METAMATERIALS FOR LIGHT AND ELECTRON WAVES: NEW PHENOMENA AND APPLICATIONS

David Emanuel Dias Fernandes

Universidade de Coimbra

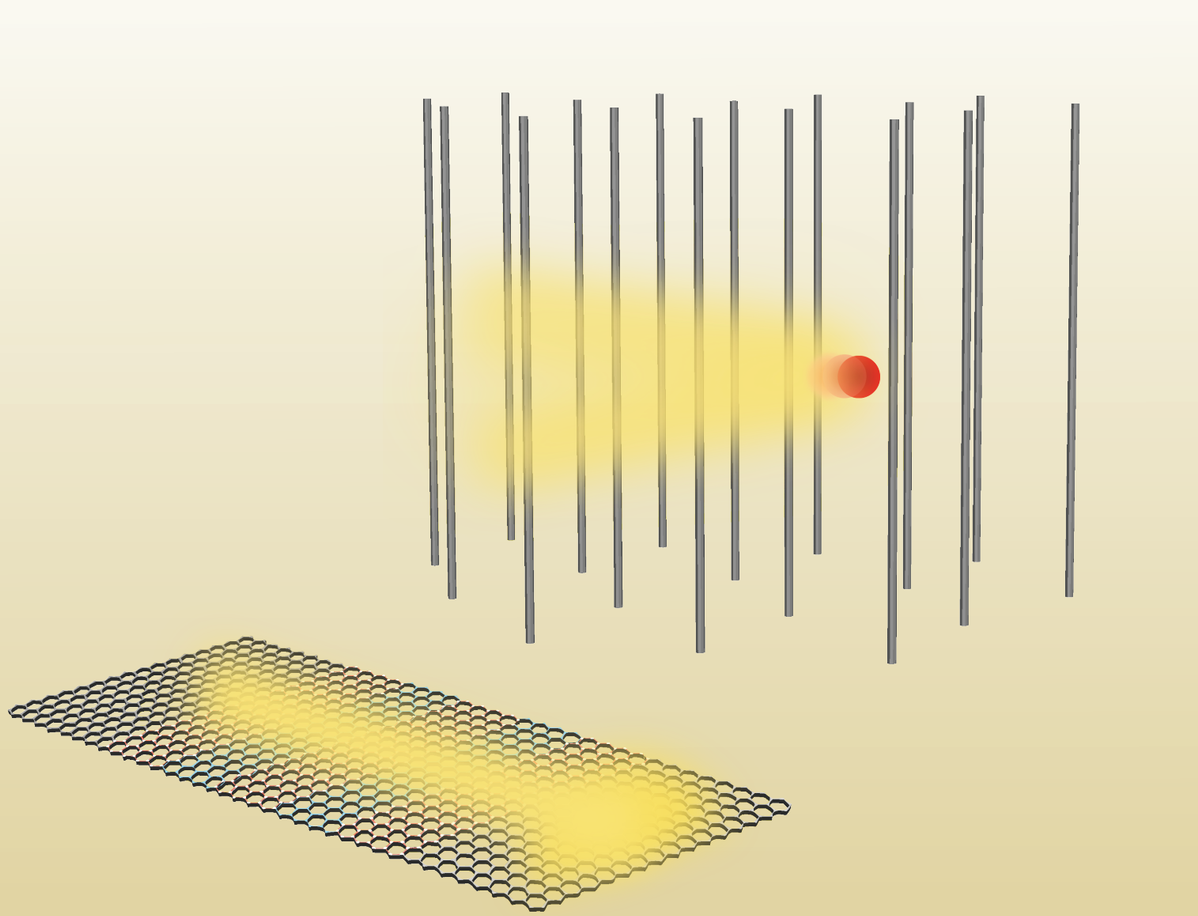

David Emanuel Dias Fernandes

METAMATERIALS FOR LIGHT AND ELECTRON WAVES: NEW PHENOMENA AND APPLICATIONS

Tese de Doutoramento em Engenharia Electrotécnica e de Computadores, ramo de especialização em Telecomunicações, orientada pelo Professor Doutor Mário Gonçalo Mestre Veríssimo Silveirinha, e apresentada ao Departamento de Engenharia Electrotécnica e de Computadores da Faculdade de Ciências e Tecnologia da Universidade de Coimbra.

Março de 2015

• U C •

UNIVERSIDADE DE COIMBRA

To my family, friends and girlfriend.

"It is paradoxical, yet true, to say, that the more we know the more ignorant we become in the absolute sense, for it is only through enlightenment that we become conscious of our limitations. Precisely one of the most gratifying results of intellectual evolution is the continuous opening up of new and greater prospects. We are progressing at an amazing pace, but the truth is that, even in fields most successfully exploited, the ground has only been broken."

(Nikola Tesla, 1856-1943)

Abstract

The electromagnetic properties of the materials directly available in Nature do not always provide enough flexibility to obtain a desired electromagnetic response. However, this limitation can be surpassed by using a new class of materials called metamaterials. Metamaterials consist of artificial structured media that may interact in a controlled and desired way with the electromagnetic radiation. In the last decades, this new class of materials has attracted the interest of the scientific community due to its applications in emerging fields such as nanophotonics and plasmonics, and a significant effort has also been made to extend the same concept to systems dealing with matter waves.

This thesis is devoted to the analytical and numerical study of novel electromagnetic phenomena in structured materials formed by arrays of parallel metallic wires, commonly known as "wire medium", and novel electronic behaviors in graphene based nanomaterials.

Regarding the study of electromagnetic phenomena in metamaterials, the main topics are the emission of Cherenkov radiation in the wire medium, the scattering engineering in nested wire media and the formation and propagation of spatial solitons in an array of nanowires embedded in a nonlinear dielectric medium.

The study of Cherenkov radiation is focused on the characterization of electromagnetic field emitted by an array of moving charges propagating inside the wire medium. We show that unlike in more conventional materials, the emission of Cherenkov radiation in the metamaterial is not limited by any charge velocity threshold. Moreover, it is demonstrated that the anomalously high density of photonic states of the nanowire array can enhance the emission of radiation by several orders of magnitude.

On the subject of the scattering engineering in a nested wire media, we derive an effective medium model for the metamaterial formed by two sets of parallel metallic wires. It is shown that the electromagnetic coupling of the two sub-arrays may result in sharp Fano-type resonances when a metamaterial slab is illuminated by a plane wave.

We also study the formation of three dimensional bright and dark spatial solitons in an array of nanowires embedded in a nonlinear dielectric medium. We derive the conditions required for the formation of each type of solitons. Parametric numerical studies reveal the influence of the metamaterials structural parameters and strength of nonlinear effects in the confinement of the solitary waves.

Finally, we investigate the possibility of extending some phenomena typically associated with electromagnetic metamaterials, such as negative refraction and propagation with no diffraction, to systems dealing with matter waves. It is shown that properly tailored graphene superlattice slabs may allow for the perfect transmission of electron waves with a specific energy, mimicking a wormhole that effectively bridges the input and output interfaces as if the region in between was nonexistent.

Keywords

Metamaterials, Wire Media, Cherenkov Radiation, Fano Resonances, Nonlinear Wire Media, Spatial Solitons, Graphene Superlattices, Negative Refraction, Diffractionless Propagation, Wormhole.

Resumo

A resposta electromagnética dos materiais directamente disponíveis na Natureza nem sempre proporciona flexibilidade suficiente para obter uma resposta electromagnética desejada. No entanto, esta limitação pode ser ultrapassada utilizando uma nova classe de materiais denominada metamateriais. Metemateriais são meios artificialmente estruturados que podem interagir de forma controlada e previamente estipulada com a radiação electromagnética. Devido às suas aplicações em áreas emergentes tais como nanofotónica e plasmónica, nas últimas décadas esta nova classe de materiais tem atraído o interesse da comunidade científica, tendo-se efectuando também um esforço significativo para estender o mesmo tipo de conceito para sistemas que utilizam ondas de matéria.

Esta tese é dedicada ao estudo analítico e numérico de novos fenómenos electromagnéticos em meios estruturados formados por agregados de fios metálicos paralelos, comummente conhecidos por *wire medium*, e novos comportamentos electrónicos em nanomateriais à base de grafeno.

Em relação ao estudo de fenómenos electromagnéticos em metamateriais, os principais temas são a emissão de radiação de Cherenkov no agregado de fios, a manipulação da dispersão num agregado de fios emparelhados e a formação e propagação de solitões espaciais num conjunto de nanofios embebido num meio dieléctrico não linear.

O estudo da radiação de Cherenkov foca-se na caracterização do campo electromagnético emitido por um conjunto de cargas que se propaga no interior do agregado de fios. Neste estudo demonstra-se que a emissão de radiação de Cherenkov no agregado de fios não tem está limitada por qualquer limiar de velocidade das cargas, contrariamente ao que se verifica nos materiais convencionais. Para além destes

resultados, demonstra-se também que a densidade de estados fotónicos anormalmente elevada do agregado de nanofios pode aumentar a emissão de radiação por várias ordens de grandeza.

Quanto ao tema da manipulação da dispersão do agregado de fios emparelhados, deduz-se um modelo de meios efectivos para o metamaterial formado por dois conjuntos de fios metálicos paralelos. Demonstra-se também que o acoplamento electromagnético entre os dois subconjuntos de fios pode originar ressonâncias de banda estreita do tipo Fano quando uma lâmina deste metamaterial é iluminada por uma onda plana.

Nesta tese também é estudada a formação solitões espaciais tridimensionais do tipo claro e escuro num agregado de nanofios embebido num meio dieléctrico não linear. Deduzem-se as condições necessárias para a formação de cada tipo de solitões e estudos paramétricos mostram a influência na escolha dos parâmetros estruturais do metamaterial e intensidade dos efeitos não lineares no confinamento dos solitões.

Por fim, investiga-se a possibilidade de estender certos fenómenos tipicamente associados a metamateriais electromagnéticos, como a propagação sem difracção e a refracção negativa, para sistemas que usem ondas de matéria. Demonstra-se também que lâminas de super-redes à base de grafeno devidamente projectadas poderão possibilitar uma transmissão perfeita de ondas electrónicas com uma energia específica, imitando um túnel espacial que liga a interface de entrada e saída como se a região entre elas não estivesse presente.

Palavras-Chave

Metamateriais, Wire Media, Radiação de Cherenkov, Ressonâncias de Fano, Wire Media não-linear, Solitões Espaciais, Super-redes de grafeno, Refracção Negativa, Propagação sem Difracção, Túnel Espacial.

Preface

This dissertation is the result of work carried out under the supervision of Prof. Mário Silveirinha, at Instituto de Telecomunicações – Coimbra and Department of Electrical and Computer Engineering of the Faculty of Sciences and Technology of the University of Coimbra between September 2010 and February 2015. The originality of this thesis is sustained in a set of journal and conference articles that have been published during my PhD research. Except where explicit reference is made to the work of others, all the research described in this dissertation is my own. For the sake of readability, not all the topics and results obtained during my PhD research will be discussed in this thesis.

Acknowledgments

The time I spent in my PhD research program was truly one of the most challenging and fulfilling periods of my life. Working towards finishing a doctoral thesis allowed me remember every progress and hiccup I ever had during that time, as well as every person that in one way or the other helped get past the bad moments and shared my joy in all successes. To all those people, my deepest and sincere gratitude.

My first words are to express my most profound gratitude to Prof. Mário Silveirinha, my PhD supervisor. Being under his guidance during these years has enriched my knowledge beyond any expectations I ever had and I consider myself very fortunate to spend this period under his tutelage. He is, without any doubt, the most brilliant person I have ever known. Finishing this thesis would not have been possible without his constant encouragement, endless support, and most of all, tremendous patience and understanding. For that, I am forever thankful.

I am also thankful to all my colleagues and friends of the Microwave Laboratory, especially João Costa and Tiago Morgado. When I first entered this laboratory I would never imagined I would find such amazing friends. If I am finishing this stage of my life, is largely because of all the help you gave me during this period. Sharing these years with you was truly amazing, and you are the best colleagues someone can hope for. Paraphrasing one of João's most famous quotes, "It will never bear any evil". Thank you so much.

To all my close friends, thank you for sharing your days with me and always being there whenever I needed. Even if we do not see each other for some time, we are always together. A special mention to Joana, Filipa, Cid, Prata and Hugo.

I want to express my deepest gratitude to my family, especially my mother, father, brother, sister-in-law and grandfather for their presence in my life, endless love, constant understanding and care. I may not be with you every day, but you are always in my heart. I would like also to dedicate all this work to the memory of my grandparents.

Last but definitely not least, a very special thanks to my girlfriend Verónica, for teaching me the invaluable lesson that we should always stay positive in life. Thank you for always being the light at the end of the tunnel that allowed me to never lose hope.

Finally, I would like to fully acknowledge the technical and financial support of *Instituto de Telecomunicações – Pólo de Coimbra* in the person of its coordinator Prof. Henrique Silva, as well as the financial support during these four years of research of the *Fundação para a Ciência e Tecnologia*, *Programa Operacional Potencial Humano/POPH*, and the cofinancing of *Fundo Social Europeu* under the fellowship SFRH/BD/70893/2010.

Contents

List of Symbols

a	Lattice period
r	Wire radius
h	Slab thickness
f_v	Volume fraction
$\mathbf{E}$	Electric field vector
$\mathbf{P}$	Polarization vector
$\mathbf{D}$	Electric Displacement vector
$\mathbf{E}$	Electric field vector
$\mathbf{B}$	Induction field vector
R	Reflection coefficient
T	Transmission coefficient
I	Microscopic current
ε_0	Permittivity of free-space
μ_0	Permeability of free-space
η_0	Impedance of free-space
ε_t	Relative permittivity along the transverse direction
ε_h	Relative permittivity of the dielectric host
v_{ph}	Phase velocity
v	Charge velocity
$\overline{\varepsilon}_{eff}$	Effective permittivity matrix
ε_m	Complex permittivity of the metal
n^2	Slow wave factor
θ_{inc}	Incidence angle
θ	Angle of emitted radiation
ω	Angular frequency
c	Speed of light in vacuum
λ	Wavelength
$\lfloor \ \rfloor$	Jump discontinuity operator
t	Time

$\mathbf{J}$	Current density
e	Electric charge
n_z	Number of charges per unit length along the *z*-direction
q	Density of charges per unit length
φ	Average potential drop
C	Capacitance per unit length
Γ	Collision frequency
k_h	Wave number in the dielectric host
k_0	Wave number in free-space
k_p	Plasma wave number
γ	Propagation constant
$\mathbf{k}$	Wave vector
(k_x, k_y, k_z)	Components of the wave vector
(x, y, z)	Position coordinates
$\mathbf{r}$	Spatial coordinate vector
$\overline{\overline{\mathbf{I}}}$	Identity matrix
τ	Relaxation time
V	Volume
$\chi^{(3)}$	Third-order electric susceptibility
Z_w	Self-impedance of the nanowires per unit length
L	Inductance of the nanowires per unit length
A_c	Area of the unit cell
N	Number of wires
ρ	Radial distance
ϕ	Azimuthal angle
W	Modal size
V_{osc}	Oscillating part of the potential
V_{av}	Average potential
$\hat{H}$	Microscopic Hamiltonian
$\hat{H}_{ef}$	Effective Hamiltonian

$\boldsymbol{\sigma}$	Pauli matrix
$\boldsymbol{\psi}$	Electron wave function
$\mathbf{v}$	Group velocity
v_F	Fermi velocity
χ	Anisotropy ratio
E_0	Energy of electrons
$\hbar$	Reduced Planck constant
$\mathbf{M}$	Transmission matrix
θ_p	Propagation angle
R_G	Gaussian beam waist
i	Imaginary unit ($\sqrt{-1}$)

I. INTRODUCTION

I.1. Overview

The advent of the semiconductor industry in the 1960's revolutionized the technological world. Since then, the continuous development of electronic devices commanded an exponential increase of the complexity and functionality of its components, contributing largely to the present era, which is punctuated by many breakthroughs and major technical developments. Bridging advances in fields that go from telecommunications and sensing systems to medical sciences and diagnosis tools, a common denominator is found in the quest for electrically small functional devices, where the precise control of the electromagnetic and electronic response of each component is of paramount importance. This scientific progress created new and challenging demands for the materials of the technological devices, and currently the complete knowledge of the electronic, optical, mechanical and even thermal properties of the materials at the atomic level is of vital significance.

Crucially, the palette of materials directly available in Nature does not always provide enough flexibility to obtain a desired electromagnetic or electronic response, ruling out many interesting applications. Motivated by the continuous development in nanotechnology and nanoscience, the answer to this limitation arrived in the form of artificial structured media, namely electromagnetic metamaterials and its electronic counterpart, the superlattices.

Metamaterials are artificial structured media formed by properly tailored metallic or dielectric inclusions, typically arranged in a periodic lattice. Remarkably, the

mesoscopic response of metamaterials depends not only on the chemical composition of the constituents, but also on its geometrical arrangement (size, shape, direction,…), introducing numerous degrees of freedom in the design of a unit cell. Microstructured composites may enable a precise manipulation of the electromagnetic field, allowing for unprecedented control over the propagation of electromagnetic waves, and thus offering a tremendous opportunity to realize response functions that were previously unattainable using solid-state materials.

An important milestone in the study of metamaterials was set in 1968, when Victor Veselago suggested in Ref. [1] that media with simultaneously negative electric permittivity and magnetic permeability (Double Negative Media – DNG media) would allow for left-handed propagation of light and an anomalous Cherenkov effect, different from what is observed in common materials [2, 3]. Still, metamaterials research was only brought into the spotlight after Sir John Pendry, in year 2000, theoretically predicted that a slab with a negative refractive index $n = -1$ would make a perfect lens, allowing for perfect imaging that is not limited by diffraction constraints [4]. The theoretical concept of DNG media was later experimentally verified by other groups in [5-7].

Motivated by this research, but also with the promise of the miniaturization of photonic and microwave devices, the continuous progress in the characterization and fabrication of metamaterials has led to important findings and significant potential applications. For instance, it was found that epsilon near zero (ENZ) metamaterials may enable the tunneling of the electromagnetic field through narrow channels, with a huge field enhancement [8, 9] and that spatially dispersive (nonlocal) metamaterials can permit broadband superlensing and anomalous dispersion of light with reduced loss [10-12]. It was also proposed that metamaterials can be used to obtain a response

characterized by an extreme optical anisotropy, allowing to manipulate the electromagnetic field in the subwavelength scale [13-20]. Enhanced nonlinear phenomena [21-25], together with "Transformation Optics" applications [26, 27], can also be counted amongst the many outstanding new possibilities that metamaterials created.

An important property of metamaterials is that provided the lattice period is much smaller than the wavelength of operation, the waves flowing through a metamaterial do to not feel the granularity of the unit cell and interact with the medium as if it were a continuous material. In these circumstances, metamaterials can be accurately described using homogenized constitutive parameters, i.e., effective permittivities and permeabilities [28-31] with precise physical meaning. In fact, this is quite similar to the electromagnetics of bulk solid-state materials wherein, in case the propagation wavelength is much larger that the atomic distance, effective parameters such as the electric permittivity and the magnetic permeability can model the electromagnetic wave propagation. Dealing with effective parameters instead of the granular details of the unit cell is useful, in the sense that it drastically simplifies the characterization of the electromagnetic response of the metamaterial.

It is well known that effective medium theories may accurately describe the electromagnetic response of many classes of metamaterials, particularly the nanowires array metamaterial [32, 33], commonly known as "wire medium". The wire medium consists of a periodic arrangement of infinitely long parallel metallic wires embedded in a dielectric medium [34]. Nanowire structures have recently attracted considerable attention, mainly due to their unusual properties, such as an anomalously high density of photonic states, as compared to natural media [35, 36], and a negative permittivity response below an engineered plasma frequency [34, 37, 38]. Moreover, because

infinitely long metallic wires are much larger than any fixed wavelength of operation, the effective response of this material is characterized by a strong spatial dispersion [32], even in the quasi-static limit [39].

Numerous intriguing electromagnetic effects have been obtained using this structure, as wire media may allow to transport and manipulate the electromagnetic radiation in the subwavelength scale [13-15, 17, 40], and permit phenomena such as superlensing [11, 41, 42] and negative refraction [43, 44]. Moreover, nonlinear responses in a metallic nanowires array can be obtained by embedding the wires in a nonlinear Kerr-type dielectric. In fact, it has been suggested that this configuration can support the propagation of stable spatial solitons [45-49]. This may enable obtaining a subwavelength confinement of light guided by the metallic nanostructures and help us to reduce the characteristic size of photonic devices. Particularly in Ref. [50], an effective medium framework has been proposed for the characterization of the electromagnetic response of this nonlinear wire media. Based on this theory, the conditions required for the formation and propagation of two-dimensional unstaggered (i.e. modes that vary slowly in the scale of the period of the unit cell) bright spatial solitons were put forward in Ref. [47].

Several modifications of the standard wire medium configuration, e.g. the periodic insertion of metallic plates in the wires, that aim to reduce the spatially dispersive effects have been proposed throughout the years [51-55]. The homogenization of double and triple perpendicular arrays of connected and non-connected wire-media has also been discussed in the literature [41, 56-59], and in particular it has been shown that double wire media may support highly confined guided modes [57, 60].

The extraordinary control over the propagation of radiation using metamaterials opened up numerous inroads into new and exciting electromagnetic phenomena [61-63].

Quite interestingly, despite the fundamental differences between light and electron waves, there are similarities between some wave phenomena in photonics and electronics. For instance, the propagation of light and matter in periodic structures [64] is described by a "band structure" [64-66]. Importantly, the concept of using artificial structured media to manipulate the way electron waves propagate in a medium was introduced by Esaki and Tsu [67] in 1970. They proposed that superlattices would allow engineering the conduction and valence bands of a semiconductor into many subbands and to control in this manner the transport properties of electrons. Superlattices are the electronic counterpart of modern electromagnetic metamaterials, and consist of a periodic arrangement of layers of distinct materials, typically semiconductor alloys. Similar to the pioneering works of Veselago [1] and Sir John Pendry [4] in the electromagnetic metamaterials field, the work of Esaki and Tsu was groundbreaking in electronics. In particular, the ability to modify the energy spectrum and, ultimately, tailoring the transport properties of the material [68-76] has attracted major interest in the study of these structures.

In the context of semiconductor physics, a material that has also been under the spotlight is graphene. This two-dimensional carbon based nanomaterial is characterized by very unusual properties such as a high crystal quality and an electronic "relativistic" spectrum, enabling to mimic some quantum relativistic phenomena in a condensed-matter system [78-83]. Particularly, it has been shown that graphene superlattices (GSLs) may be used to tailor the transport properties of electrons [84-86] and support the propagation of electron beams with virtually no diffraction [87, 88], mirroring the behavior of a metamaterial with extreme anisotropy.

The propagation of the charge carriers in pristine graphene and in graphene superlattices is governed by the massless Dirac equation. It was proven in [89] that the

"low energy physics" in graphene can be accurately characterized using an effective medium approach that describes the dynamics of the wave function envelope. Quite importantly, these homogenization techniques bridge some ideas and methods developed in the context of metamaterial systems to the characterization of systems dealing with matter waves. Interestingly, using this effective medium framework it was recently proposed in [89, 90] that it may be possible to have the electronic counterpart of the perfect lens for photons proposed by Sir John Pendry [4] based on the superlattice concept.

This thesis is devoted to the study of new emerging phenomena arising from the interaction between electromagnetic waves with metamaterials and matter waves with graphene superlattices.

The electromagnetic study is focused on unconventional applications of wire media. All the theoretical studies are conducted using effective medium models, and in most cases they are numerically validated with full-wave electromagnetic simulators.

The interaction of matter waves and graphene superlattices is analyzed using a theoretical model under a microscopic approach, where all the granular details of the superlattice are taken into account, and using an effective medium framework. Both methods will be used to unveil new and intriguing phenomena for electron wave propagation in graphene superlattices, with the intent of bridging some phenomena typically associated with photons to electron waves.

Throughout the thesis we assume a time variation of the type $e^{-i\omega t}$ in stationary states regimes.

I.2. Organization of the Thesis

The thesis is organized in 6 chapters.

Chapter II develops an effective medium model for a nested wire media, such that the unit cell of the structure has two inequivalent sets of parallel metallic wires. Using this model, we develop a formalism to calculate the scattering properties of a slab of the metamaterial. Since the electromagnetic coupling between each set of wires may strongly influence the overall response of the medium, we study the effects of changing the wires material on the scattering properties of the metamaterial. All results are compared with full-wave electromagnetic simulations.

In Chapter III we study the emission of Cherenkov radiation by an array of electric charges propagating in the wire medium. Motivated by the anomalously high density of photonic states of the wire medium, we investigate the possibility of enhancing the Cherenkov emission as compared to more conventional materials. Based on effective medium techniques, we derive an analytical model to calculate the radiation patterns of the emitted radiation and the energy loss rate of the moving charges. This model is used to study the influence of the structural parameters of the metamaterial in the directionality of the emitted light beams and in the amount of emitted radiation.

In the fourth Chapter of this thesis, we investigate the formation and propagation of bright and dark three-dimensional spatial solitons in a nanowire array embedded in a nonlinear Kerr-type dielectric. Using the effective medium model introduced in Ref. [50], we study the conditions for the formation of solitary waves in the metamaterial. In this Chapter we also develop a formalism to characterize the propagation of spatial solitons in the metamaterial. This formalism is used to calculate the profile of dark and bright solitary waves. Parametric studies are presented to show how the confinement of the solitary waves is affected by the hiperbolicity of the isofrequency contours of the

metamaterial, by the absorption in both the nonlinear dielectric and metal, and by the strength of the nonlinear effects.

Chapter V studies the electron wave propagation in graphene superlattices using an effective medium framework. The first part of the Chapter is dedicated to the numerical validation of the effective medium model. The scattering properties of a cascade of GSL slabs are calculated with the macroscopic approach and compared to the exact microscopic theory. The main objective of this Chapter is to extend some phenomena typically associated with electromagnetic metamaterials, such as negative refraction and propagation with no diffraction, to systems dealing with matter waves. Moreover, we also study the possibility of engineering a GSL slab to effectively "short-circuit" the input and output interfaces, extending the concept of light "wormholes" to electron waves in graphene.

Finally, in Chapter VI, the main conclusions of this thesis are presented, as well as some suggestions for future work.

I.3. Main Contributions

The key contributions of the present thesis are:

- Development and validation of an effective medium model for the nested wire media structure.
- Proof that the coupling between each set of sub-arrays in the nested wire media allows for the emergence of Fano resonances in the scattering response of a metamaterial slab.
- Use of effective medium techniques to characterize the emission of Cherenkov radiation in nanowire arrays.
- Demonstration that the wire medium allows for a massive Cherenkov emission with no charge velocity threshold.

- Macroscopic approach to investigate the formation and propagation of three dimensional unstaggered bright and dark spatial solitons with cylindrical symmetry in nanowire structures embedded in Kerr-type nonlinear media.
- Effective medium model for electron wave propagation in graphene superlattices.
- Demonstration of new phenomena in GSLs such as diffractionless propagation of electron waves.
- Proposal of a graphene based heterostructure that mimics a "wormhole" for matter waves.

Throughout the thesis each of the aforementioned topics is expanded, and the new contributions are compared with the open literature.

I.4. List of Author Publications

I.4.1. Articles in Journals

I.4.1.1 Articles in journals in the topics of this thesis

[J1] **D. E. Fernandes**, S. I. Maslovski, and M. G. Silveirinha, "Cherenkov emission in a nanowire material", *Phys. Rev. B.* **85**, 155107, 2012.

[J2] **D. E. Fernandes**, S. I. Maslovski, G. W. Hanson, and M. G. Silveirinha, "Fano resonances in nested wire media", *Phys. Rev. B.* **88**, 045130, 2013 **[This paper has been selected by the editors of PRB to be an Editors' Suggestion]**.

[J3] **D. E. Fernandes**, and M. G. Silveirinha, "Bright and Dark Spatial Solitons in Metallic Nanowire Arrays", *Phot. Nanostr. Fund. Appl.* **12**, 340, 2014.

[J4] **D. E. Fernandes**, N. Engheta, and M. G. Silveirinha, "Wormhole for electron waves in graphene", *Phys. Rev. B.* **90**, 041406(R), 2014.

I.4.1.2 Articles in journals in other topics

[J5] **D. E. Fernandes**, S. I. Maslovski, and M. G. Silveirinha, "Asymmetric Mushroom-Type Metamaterials", *IEEE Trans. Microwave Theory Tech.* **62**, 8, 2014.

[J6] **D. E. Fernandes**, and M. G. Silveirinha, "Optical Tractor Beam with Chiral Light", *submitted* (arXiv:1501.03192).

[J7] **D. E. Fernandes**, M. Rodrigues, G. Falcão, and M. G. Silveirinha, "Time Evolution of Electron Waves in Graphene Superlattices", *to be submitted.*

I.4.2. Articles in Conference Proceedings

[C1] **D. E. Fernandes**, S. I. Maslovski, and M. G. Silveirinha, "Boosting the Cherenkov radiation with a nanowire material", in *Proc. 8th Iberian Meeting on Computational Electromagnetics - EIEC*, Sesimbra, Portugal, November 2011.

[C2] **D. E. Fernandes**, S. I. Maslovski, and M. G. Silveirinha, "Enhancement of Cherenkov emission inside a nanowire material", in *Proc. Days on Diffraction*, St. Petersburg, Russia, May 2012.

[C3] **D. E. Fernandes**, S. I. Maslovski, and M. G. Silveirinha, "Cherenkov emission in a nanowire material", in *Proc. 6th Congress of the Portuguese Committee of URSI*, Lisbon, Portugal, May 2012.

[C4] **D. E. Fernandes**, and M. G. Silveirinha, "Electron Dynamics in Graphene Superlattices: Microscopic and Effective Medium Models", in *Proc. Conf. on Telecommunications - ConfTele*, Castelo Branco, Portugal, May 2013.

[C5] **D. E. Fernandes**, and M. G. Silveirinha, "Characterization of the dynamics of carriers in graphene superlattices using microscopic and effective medium models" in *Proc. MPNS COST Action Training School – MP1204 TERA-MIR*

Radiation: Materials, Generation, Detection and Applications, Cortona, Italy, May 2013.

[C6] **D. E. Fernandes**, and M. G. Silveirinha, "Spatial solitons in a nanowire array embedded in a self-defocusing medium", in *Proc. Metamorphose International Congress on Advanced Electromagnetic Materials in Microwaves and Optics – METAMATERIALS*, Bordeaux, France, September 2013 **[this paper was awarded with the fourth place in the student paper competition].**

[C7] **D. E. Fernandes**, N. Engheta, and M. G. Silveirinha, "Negative refraction and perfect tunneling of electron waves in graphene superlattices", in *Proc. Metamorphose International Congress on Advanced Electromagnetic Materials in Microwaves and Optics – METAMATERIALS*, Bordeaux, France, September 2013.

[C8] **D. E. Fernandes**, N. Engheta, and M. G. Silveirinha, " "Tunnel" for electron waves in graphene superlattices", in *Proc. Metamorphose International Congress on Advanced Electromagnetic Materials in Microwaves and Optics – METAMATERIALS*, Copenhagen, Denmark, August 2014.

[C9] **D. E. Fernandes**, and M. G. Silveirinha, "Optical Tractor Beam with Chiral Light", in *Proc. 8th Congress of the Portuguese Committee of URSI*, Lisbon, Portugal, November 2014.

[C10] **D. E. Fernandes**, M. Rodrigues, G. Falcão, and M. G. Silveirinha, "Time dynamics of electron waves in graphene superlattices", in *Proc. Theory, Modelling and Coputational Methods for Semiconductors – European Session*, Granada, Spain, January 2015.

[C11] **D. E. Fernandes**, and M. G. Silveirinha, "Chiral Metamaterials for Optical Pulling Forces", in *Proc. 9th European Conference on Antennas and Propagation - EUCAP 2015*, Lisbon, Portugal, April 2015.

References

[1] V. G. Veselago, "The electrodynamics of substances with simultaneously negative values of ε and μ", *Sov. Phys. Usp.* **10**, 509, 1968.

[2] P. A. Čerenkov, "Visible radiation produced by electrons moving in a medium with velocities exceeding that of light", *Phys. Rev.* **52**, 378, 1934.

[3] I. M. Frank, and I. E. Tamm, "Coherent visible radiation of fast electrons passing through matter", *Compt. Rend. (Dokl.)* **14**, 109, 1937.

[4] J. B. Pendry, "Negative Refraction Makes a Perfect Lens", *Phys. Rev. Lett.* **85**, 3966, 2000.

[5] D. R. Smith, W. J. Padilla, D. C. Vier, S. C. Nemat-Nasser, and S. Schultz, "Composite Medium with Simultaneously Negative Permeability and Permittivity", *Phys. Rev. Lett.*. **84**, 4184, 2000.

[6] R. A. Shelby, D. R. Smith, and S. Schultz, "Experimental Verification of Negative Index of Refraction", *Science* **292**, 77, 2006.

[7] J. Valentine, S. Zhang, T. Zentgraf, E. Ulin-Avila, D. A. Genov, G. Bartal, and X. Zhang, "Three-dimensional optical metamaterials with a negative refractive index", *Nature* **455**, 376, 2008.

[8] M. Silveirinha, and N. Engheta, "Tunneling of Electromagnetic Energy through Subwavelength Channels and Bends using ε-Near-Zero Materials", *Phys. Rev. Lett.* **97**, 157403, 2006.

[9] M. Silveirinha, and N. Engheta, "Transporting an Image through a Subwavelength Hole", *Phys. Rev. Lett.* **102**, 103902, 2009.

[10] M. G. Silveirinha, "Anomalous Refraction of Light Colors by a Metamaterial Prism", *Phys. Rev. Lett.* **102**, 193903, 2009.

[11] M. G. Silveirinha, C. R. Medeiros, C. A. Fernandes, and J. R. Costa, "Experimental verification of broadband superlensing using a metamaterial with an extreme index of refraction", *Phys. Rev. B* **81**, 033101, 2010.

[12] J. T. Costa, and M. G. Silveirinha, "Achromatic lens based on a nanowire material with anomalous dispersion", *Opt. Express* **20**, 13915, 2012.

[13] P. A. Belov, Y. Hao, and S. Sudhakaran*,* P. A. Belov, Y. Hao, and S. Sudhakaran, "Subwavelength microwave imaging using an array of parallel conducting wires as a lens", *Phys. Rev. B* **73**, 033108, 2006.

[14] M. G. Silveirinha, P. A. Belov, and C. Simovski, "Subwavelength Imaging at Infrared Frequencies Using an Array of Metallic Nanorods", *Phys. Rev. B* **75**, 035108 (2007).

[15] G. Shvets, S. Trendafilov, J. B. Pendry, and A. Sarychev, "Guiding, Focusing, and Sensing on the Subwavelength Scale using Metallic Wire Arrays", *Phys. Rev. Lett.* **99**, 053903, 2007.

[16] M. G. Silveirinha, P. A. Belov, and C. R. Simovski, "Ultimate limit of resolution of subwavelength imaging devices formed by metallic rods", *Opt. Lett.* **33**, 1726, 2008.

[17] P. A. Belov, Y. Zhao, S. Tse, P. Ikonen, M. G. Silveirinha, C. R. Simovski, S. Tretyakov, Y. Hao, and C. Parini, "Transmission of images with subwavelength resolution to distances of several wavelengths in the microwave range", *Phys. Rev. B* **77**, 193108, 2008.

[18] M. G. Silveirinha, C. R. Medeiros, C. A. Fernandes, and J. R. Costa, "Resolving subwavelength objects with a crossed wire mesh superlens operated in backscattering mode", *New J. Phys*. **13**, 053004, 2011.

[19] C. S. R. Kaipa, A. B. Yakovlev, S. I. Maslovski, and M. G. Silveirinha, "Indefinite dielectric response and all-angle negative refraction in a structure with deeply-subwavelength inclusions", *Phys. Rev. B* **84**, 165135, 2011.

[20] M. G. Silveirinha, and N. Engheta, "Sampling and squeezing electromagnetic waves through subwavelength ultranarrow regions or openings", *Phys. Rev. B* **85**, 085116, 2012.

[21] M. Lapine, M. Gorkunov, and K. Ringhofer, "Nonlinearity of a metamaterial arising from diode insertions into resonant conductive elements", *Phys. Rev. E* **67**, 065601, 2003.

[22] A. Zharov, I. Shadrivov, and Y. Kivshar, "Nonlinear Properties of Left-Handed Metamaterials", *Phys. Rev. Lett.* **91**, 037401, 2003.

[23] V. M. Agranovich, Y. R. Shen, R. H. Baughman, and A. A. Zakhidov, "Linear and nonlinear wave propagation in negative refraction metamaterials", *Phys. Rev. B* **69**, 165112, 2004.

[24] E. Poutrina, D. Huang, and D. R. Smith, "Analysis of nonlinear electromagnetic metamaterials", *New J. Phys.* **12**, 093010, 2010.

[25] M. Lapine, I. V. Shadrivov, and Y. S. Kivshar, "Colloquium: Nonlinear metamaterials", *Rev. Mod. Phys.* **86**, 1093, 2014.

[26] R. Liu, C. Ji, J. J. Mock, J. Y. Chin, T. J. Cui, and D. R. Smith, "Broadband ground-plane cloak", Science **323**, 66, 2009.

[27] H. Chen, C. T. Chan, and Ping Sheng, "Transformation optics and metamaterials", Nature Materials **9**, 387, 2010.

[28] M. G. Silveirinha, "Metamaterial homogenization approach with application to the characterization of microstructured composites with negative parameters", *Phys. Rev. B* **75**, 115104, 2007.

[29] C. R. Simovski, and S. A. Tretyakov, "Local constitutive parameters of metamaterials from an effective medium perspective", *Phys. Rev. B* **75**, 195111, 2007.

[30] M. G. Silveirinha, "Time Domain Homogenization of Metamaterials", *Phys. Rev. B* **83**, 165104, 2011.

[31] J. T. Costa, M. G. Silveirinha, and S. I. Maslovski, "Finite-difference frequency domain method for the extraction of effective parameters of metamaterials", *Phys. Rev. B* **80**, 235124, 2009.

[32] M. G. Silveirinha, "Nonlocal homogenization model for a periodic array of epsilon-negative rods", *Phys. Rev. E* **73**, 046612, 2006.

[33] M. G. Silveirinha, and C. A. Fernandes, "Homogenization of 3D- Connected and Non-Connected Wire Metamaterials", *IEEE Trans. on Microwave Theory and Tech.* **53**, 1418, 2005.

[34] C. R. Simovski, P. A. Belov, A. V. Atrashchenko, and Y. S. Kivshar, "Wire metamaterials: physics and applications", *Adv.Mater.* **24**, 4229, 2012.

[35] S. I. Maslovski, and M. G. Silveirinha, "Ultralong-range Casimir-Lifshitz forces mediated by nanowire materials", *Phys. Rev. A* **82**, 022511, 2010.

[36] S. I. Maslovski, and M. G. Silveirinha, "Mimicking Boyer's Casimir repulsion with a nanowire material", *Phys. Rev. A* **83**, 022508, 2011.

[37] D. R. Smith, and D. Schurig, "Electromagnetic Wave Propagation in Media with Indefinite Permittivity and Permeability Tensors", *Phys. Rev. Lett.* **90**, 077405, 2003.

[38] M. G. Silveirinha, "Broadband Negative Refraction with a Crossed Wire Mesh", *Phys. Rev. B* **79**, 153109, 2009.

[39] P. A. Belov, R. Marques, S. I. Maslovski, I. S. Nefedov, M. Silveirinha, C. R. Simovski, and S. A. Tretyakov, "Strong spatial dispersion in wire media in the very large wavelength limit", *Phys. Rev. B* **67**, 113103, 2003.

[40] P. Ikonen, C. Simovski, S. Tretyakov, P. Belov, and Y. Hao, "Magnification of subwavelength field distributions at microwave frequencies using a wire medium slab operating in the canalization regime", *Appl. Phys. Lett.* **91**, 104102, 2007.

[41] M. G. Silveirinha, "Artificial plasma formed by connected metallic wires at infrared frequencies", *Phys. Rev. B* **79**, 035118, 2009.

[42] M. G. Silveirinha, C. A. Fernandes, and J. R. Costa, "Superlens made of a metamaterial with extreme effective parameters", *Phys. Rev. B* **78**, 195121, 2008.

[43] Y. Liu, G. Bartal, and X. Zhang, "All-angle negative refraction and imaging in a bulk medium made of metallic nanowires in the visible region", *Opt. Express* **16**, 15439, 2008.

[44] J. Yao, Z. Liu, Y. Liu, Y. Wang, C. Sun, G. Bartal, A. M. Stacy, and X. Zhang, "Optical Negative Refraction in Bulk Metamaterials of Nanowires", *Science* **321**, 930, 2008.

[45] Y. Liu, G. Bartal, D. A. Genov, and X. Zhang, "Subwavelength Discrete Solitons in Nonlinear Metamaterials", *Phys. Rev. Lett.* **99**, 153901, 2007.

[46] F. Ye, D. Mihalache, B. Hu, and N. C. Panoiu, "Subwavelength Plasmonic Lattice Solitons in Arrays of Metallic Nanowires", *Phys. Rev. Lett.* **104**, 106802, 2010.

[47] M. G. Silveirinha, "Theory of Spatial Optical Solitons in Metallic Nanowire Materials", *Phys. Rev. B* **87**, 235115, 2013.

[48] F. Ye, D. Mihalache, B. Hu, and N. C. Panoiu, "Subwavelength vortical plasmonic lattice solitons", *Opt. Lett.* **36**, 1179, 2011.

[49] Y. Kou, F. Ye, and X. Chen, "Multipole plasmonic lattice solitons", *Phys. Rev. A* **84**, 033855, 2011.

[50] M. G. Silveirinha, "Effective Medium Response of Metallic Nanowire Arrays with a Kerr-type Dielectric Host", *Phys. Rev. B* **87**, 165127, 2013.

[51] A. Demetriadou, and J.B. Pendry, "Taming spatial dispersion in wire metamaterial", *Phys. Condens. Matter* **20**, 295222, 2008.

[52] O. Luukkonen, M. G. Silveirinha, A. B. Yakovlev, C. R. Simovski, I. S. Nefedov, and S. A. Tretyakov, "Effects of Spatial Dispersion on Reflection from Mushroom-type Artificial Impedance Surfaces", *IEEE Trans. Microwave Theory Tech.* **57**, 2692, 2009.

[53] A. B. Yakovlev, M. G. Silveirinha, O. Luukkonen, C. R. Simovski, I. S. Nefedov, and S. A. Tretyakov, "Characterization of Surface-Wave and Leaky-Wave Propagation on Wire-Medium Slabs and Mushroom Structures Based on Local and Non-Local Homogenization Models", *IEEE Trans. Microwave Theory Tech.* **57**, 2700, 2009.

[54] S. I. Maslovski, and M. G. Silveirinha, "Nonlocal permittivity from a quasistatic model for a class of wire media", *Phys. Rev. B* **80**, 245101, 2009.

[55] S. I. Maslovski, T. A. Morgado, M. G. Silveirinha, C. S. R. Kaipa, and A. B. Yakovlev, "Generalized additional boundary conditions for wire media", *New J. Phys.* **12**, 113047, 2010.

[56] J. Shin, J.-T. Shen, and S. Fan, "Three-dimensional electromagnetic metamaterials that homogenize to uniform non-Maxwellian media", *Phys. Rev B* **76**, 113101, 2007.

[57] M. G. Silveirinha, and C. A. Fernandes, "Nonresonant structured material with extreme effective parameters", *Phys. Rev. B* **78**, 033108, 2008.

[58] M. G. Silveirinha, "Additional Boundary Conditions for Nonconnected Wire Media", *New J. Phys.* **11**, 113016, 2009.

[59] G. W. Hanson, E. Forati, and M. G. Silveirinha, "Modeling of spatially-dispersive wire media: transport representation, comparison with natural materials, and additional boundary conditions", *IEEE Trans. on Antennas and Propagat.* **60**, 4219, 2012.

[60] T. A. Morgado, J. S. Marcos, M. G. Silveirinha, and S. I. Maslovski, "Ultraconfined Interlaced Plasmons", *Phys. Rev. Lett.* **107**, 063903, 2011.

[61] A. Shivola, "Metamaterials in electromagnetics", *Metamaterials* **1**, 2, 2007.

[62] G. Shvets, "Metamaterials add an extra dimension", *Nature Materials* **7**, 7, 2008.

[63] Y. Liua, and X. Zhang, "Metamaterials: a new frontier of science and technology", *Chem. Soc. Rev.* **40**, 2494, 2011.

[64] J. D. Joannopoulos, S. G. Johnson, J. N. Winn, and R. D. Meade, *Photonic Crystals: Molding the Flow of Light,* Princeton University Press, Princeton, 2008.

[65] E. Yablonovitch, "Inhibited Spontaneous Emission in Solid-State Physics and Electronics", *Phys. Rev. Lett.* **58**, 2059, 1987.

[66] S. John, "Strong localization of photons in certain disordered dielectric superlattices", *Phys. Rev. Lett.* **58**, 2486, 1987.

[67] L. Esaki, and R. Tsu, "Superlattice and Negative Differential Conductivity in Semiconductors", *IBM J. Res. Dev.* **14**, 61, 1970.

[68] D. Weiss, K. V Klitzing, K. Ploog, and G. Weimann, "Magnetoresistance Oscillations in a Two-Dimensional Electron Gas Induced by a Submicrometer Periodic Potential", *Europhys. Lett.* **8**, 179, 1989.

[69] D. Weiss, M. L. Roukes, A. Menschig, P. Grambow, K. von Klitzing, and G. Weimann, "Electron pinball and commensurate orbits in a periodic array of scatterers", *Phys. Rev. Lett.* **66**, 2790, 1991.

[70] D. Pfannkuche, and R. R. Gerhardts, "Theory of magnetotransport in two-dimensional electron systems subjected to weak two-dimensional superlattice potentials", *Phys. Rev. B* **46**, 12606, 1992.

[71] D. K. Ferry, "Quantum magnetotransport in lateral surface superlattices", *Prog. Quant. Electr.* **16**, 251, 1992.

[72] C. Albrecht, J. H. Smet, D. Weiss, K. von Klitzing, R. Hennig, M. Langenbuch, M. Suhrke, U. Rössler, V. Umansky, and H. Schweizer, "Fermiology of two-dimensional lateral superlattices", *Phys. Rev. Lett.* **83**, 2234, 1999.

[73] T. Schlösser, K. Ensslin, J. P. Kotthaus, and M. Holland, "Internal structure of a Landau band induced by a lateral superlattice: a glimpse of Hofstadter's butterfly", *Europhys. Lett.* **33**, 683, 1996.

[74] C. Albrecht, J. H. Smet, K. von Klitzing, D. Weiss, V. Umansky, and H. Schweizer, "Evidence of Hofstadter's fractal energy spectrum in the quantized Hall conductance", *Phys. Rev. Lett.* **86**, 147, 2001.

[75] M. C. Geisler, J. H. Smet, V. Umansky, K. von Klitzing, B. Naundorf, R. Ketzmerick, and H. Schweizer, "Detection of a Landau band-coupling-induced rearrangement of the Hofstadter butterfly", *Phys. Rev. Lett.* **92**, 256801, 2004.

[76] L. A. Ponomarenko, R. V. Gorbachev, G. L. Yu, D. C. Elias, R. Jalil, A. A. Patel, A. Mishchenko, A. S. Mayorov, C. R. Woods, J. R. Wallbank, M. Mucha-Kruczynski, B. A. Piot, M. Potemski, I. V. Grigorieva, K. S. Novoselov, F. Guinea, V. I. Fal'ko, and

A. K. Geim, “Cloning of Dirac fermions in graphene superlattices”, *Nature* **497**, 594, 2013.

[77] K. S. Novoselov, A. K. Geim, S. V. Morozov, D. Jiang, M. I. Katsnelson, I. V. Grigorieva, S. V. Dubonos, and A. A. Firsov, “Two-dimensional gas of massless Dirac fermions in graphene”, *Nature* **438**, 197, 2005.

[78] A. K. Geim, and K. S. Novoselov, “The rise of graphene”, *Nature Mater.* **6**, 183, 2007.

[79] A. H. Castro Neto, F. Guinea, N. M. R. Peres, K. S. Novoselov, and A. K. Geim, “The electronic properties of graphene”, *Rev. Mod. Phys.* **81**, 109, 2009.

[80] M. I. Katsnelson, “The electronic properties of graphene”, *Mater. Today* **10**, 20, 2007.

[81] M. I. Katsnelson, K. S. Novoselov, and A. K. Geim, “Chiral tunnelling and the Klein paradox in graphene”, *Nat. Phys.* **2**, 620, 2006.

[82] A. V. Rozhkov, G. Giavaras, Y. P. Bliokh, V. Freilikher, and F. Nori, “Electronic properties of mesoscopic graphene structures: Charge confinement and control of spin and charge transport”, *Phys. Rep.* **77**, 503, 2011.

[83] A. Vakil, and N. Engheta, “Transformation Optics Using Graphene”, *Science* **332**, 1291, 2011.

[84] Y. P. Bliokh, V. Freilikher, S.Savel’ev, and F. Nori, “Transport and localization in periodic and disordered graphene superlattices”, *Phys. Rev. B* **79**, 075123, 2009.

[85] P. Burset, A. L. Yeyati, L. Brey, and H. A. Fertig, “Transport in superlattices on single-layer graphenes”, *Phys. Rev. B* **83**, 195434, 2011.

[86] L.-G. Wang, and S.-Y. Zhu, “Electronic band gaps and transport properties in graphene superlattices with one-dimensional periodic potentials of square barriers”, *Phys. Rev. B* **81**, 205444, 2010.

[87] C. H. Park, L. Yang, Y. W. Son, M. L. Cohen, and S. G. Louie, “New Generation of Massless Dirac Fermions in Graphene under External Periodic Potentials”, *Phys. Rev. Lett.* **101**, 126804, 2008.

[88] C.-H. Park, L. Yang, Y.-W. Son, M. L. Cohen, and S. G. Louie, “Anisotropic behaviours of massless Dirac fermions in graphene under periodic potentials”, *Nat. Phys.* **4**, 213, 2008.

[89] M. G. Silveirinha, and N. Engheta, “Effective medium approach to electron waves: Graphene superlattices”, *Phys. Rev. B* **85**, 195413, 2012.

[90] M. G. Silveirinha, and N. Engheta,” Spatial Delocalization and Perfect Tunneling of Matter Waves: Electron Perfect Lens”, *Phys. Rev. Lett.* **110**, 213902, 2013.

II. SCATTERING ENGINEERING WITH WIRE MEDIA

II.1. Introduction

In the context of metamaterials research one of the most relevant structures is the uniaxial wire medium. The wire medium consists of a set of infinitely long wires oriented along the same axis and embedded in a dielectric medium [1-2]. As discussed in Chapter I, nanowire materials have been recently on focus due to their unusual electromagnetic properties, some of which are the anomalously high density of photonic states, as compared to more natural media [3-5], and a negative permittivity response below an engineered plasma frequency [6-8]. Because of these properties this artificial media gained an increasing importance, and it was proven that wire media may be useful in many applications in the microwave through mid-THz frequency band [9-15].

The use of effective medium techniques to describe the behavior of this material, e.g. [16, 17], soon became of invaluable importance. As discussed in Sec. I.1, it was found that the effective medium response of this material is characterized by a strong non-local (spatially dispersive) response [16, 17]. It has been shown that the nonlocal response may be tamed by periodically inserting metallic plates in the metallic wires [18-22]. Other wire medium topologies, such as double and triple perpendicular arrays of connected and non-connected wire-media, have also been discussed in the literature [23-27]. In fact, a significant effort has been dedicated to the homogenization of such complex media, as it may enable new exciting electromagnetic phenomena [14, 24].

Nevertheless, the homogenization of a metamaterial formed by two nonconnected perpendicular wire arrays [24] in the scenario wherein the two wire arrays are parallel, so that each unit cell of the material contains two parallel wires, remains an open problem. From here on, the metamaterial formed by two inequivalent parallel metallic wire arrays will be designated by "nested wire medium". The effective response of the nested wire media is quite peculiar. The key feature is the hybridization of the modes supported by the individual arrays, which is a consequence of the interactions between the nested wire arrays. In particular the number of natural modes (plane waves) supported by the metamaterial (within an effective medium description) is greater than in conventional wire media, making it challenging to describe the wave propagation with effective medium techniques.

In this chapter, we develop an effective medium model for the nested wire media. The effective dielectric constant of the bulk metamaterial medium is derived and the photonic modes supported by the bulk medium are characterized.

Using this effective medium model, we propose a formalism to solve scattering problems. Namely, we introduce a set of boundary conditions necessary to characterize the scattering by a metamaterial slab. The purpose of this study is to show that the transmission and reflection properties of the nested wire media may be drastically modified if there is some structural asymmetry in the system, for instance if each sub-array is made of a different metal. In fact, it will be shown that the electromagnetic coupling of the two sub-arrays may enable one to engineer the scattering response in such a way that sharp Fano-type resonances [28, 29] appear in the transmission and reflection coefficients of the nested wire media.

The Fano resonances are characterized by a sharp asymmetric line shape and were named after the renowned Italian physicist Ugo Fano. In 1935 Ugo Fano successfully

derived a theoretical formalism [30] to explain the asymmetric peaks seen in the spectra of radiation absorbed by atoms observed by Hans Beutler in 1935 [31]. A few decades later, in 1961, U. Fano developed his first work to predict the shape of spectral lines [28]. This new model became very important in a variety of subjects such as nuclear, atomic, molecular and condensed-matter physics. The reason for this lies on the fundamental fact that these resonances originate from the interference of two or more oscillators, hence they can be observed in quite distinct physical systems. In particular, Fano resonances have been recently demonstrated in plasmonic structures and metamaterials [29-34]. Because of its narrow lineshape, Fano resonances have promising applications in sensing, e.g. in the development of novel chemical or biosensors.

II.2. Effective Medium Model of the Nested Wire Media

II.2.1. Effective Permittivity

In this section, we characterize the effective medium response of the nested wire media. The wires are oriented along the *z*-direction, such that the unit cell of the bulk material contains two inequivalent metallic wires, denoted by *A* and *B* in Fig. 2.1.

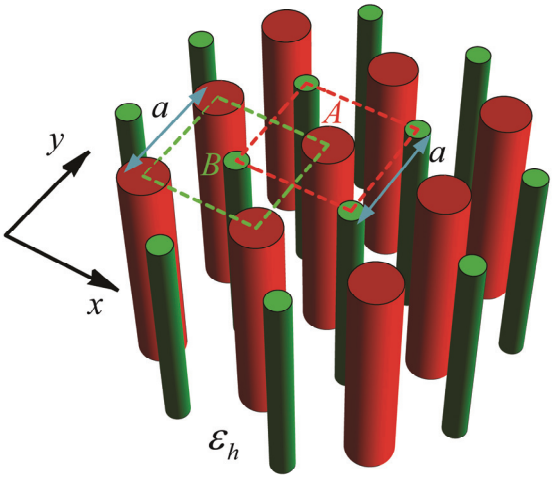

Fig. 2.1. Geometry of the two nested wire media denoted by *A* and *B*. The two arrays are arranged in a periodic square lattice with period a and the wires are embedded in a dielectric host material with permittivity ε_h.

This structure is manifestly different from the standard wire medium structure, which is formed by a single set of infinitely long metallic wires arranged in a periodic square lattice. Assuming that the wires are oriented along the *z*-direction, it has been shown [16, 17] that the wire medium is characterized an effective permittivity tensor that reads:

$$\bar{\bar{\varepsilon}}_{eff}\left(\omega,k_z\right)=\varepsilon_h\left\{\varepsilon_t\left(\hat{\mathbf{x}}\hat{\mathbf{x}}+\hat{\mathbf{y}}\hat{\mathbf{y}}\right)+\varepsilon_{zz}\hat{\mathbf{z}}\hat{\mathbf{z}}\right\} \tag{2.1}$$

where ε_h is the permittivity of the dielectric, $\varepsilon_{zz}=1+\left[\frac{\varepsilon_h}{\left(\varepsilon_m-\varepsilon_h\right)f_V}-\frac{k_h^2-k_z^2}{k_p^2}\right]^{-1}$, $k_h=\omega\sqrt{\varepsilon_h\mu_0}$ is the wave number in the dielectric host medium, $f_V=\pi\left(r/a\right)^2$ is the volume fraction of the metal, ε_m is the complex permittivity of the metallic wires and k_p is a structural parameter with the physical meaning of a plasma wave number. Within a thin wire approximation it can be checked that $\left(k_p a\right)^2\approx 2\pi\left[0.5275+\ln\left(\frac{a}{2\pi r}\right)\right]^{-1}$ and the transverse permittivity satisfies $\varepsilon_t\approx 1$ [16,

17]. The explicit dependence of the dielectric function on the wave vector $k_z \leftrightarrow -i\frac{d}{dz}$ implies a strong non-local behavior [16, 17].

In order to derive an expression for the effective permittivity of the nested wire media, it is important to realize that provided the two sub-arrays are not very strongly coupled in the near-field, so that the influence of one array on the other can be regarded as a macroscopic excitation, the contribution of each array to the electric polarization is related to the macroscopic electric field as [27]:

$$\mathbf{P}_l = \left[\overline{\overline{\varepsilon}}_{eff,l}\left(\omega, -i\frac{d}{dz}\right) - \varepsilon_h \overline{\overline{\mathbf{I}}} \right] \cdot \mathbf{E}, \qquad l=A,B. \tag{2.2}$$

where $\overline{\overline{\varepsilon}}_{eff,A}$ and $\overline{\overline{\varepsilon}}_{eff,B}$ are the effective permittivities of each set of the nested wires, defined as in Eq. (2.1), with pertinent structural parameters dependent on the considered sub-array, and $\overline{\overline{\mathbf{I}}}$ is the identity matrix. The requirement that the two sub-arrays interact with one another as macroscopic sources is better satisfied when the two wires in the unit cell are as far apart as possible, which is the case represented in Fig. 2.1.

The effective permittivity of the nested wire arrays describes the response of the total polarization vector $\mathbf{P}_A + \mathbf{P}_B$ to the macroscopic electric field. Therefore, it must satisfy

$$\overline{\overline{\varepsilon}}_{eff,A+B}\left(\omega, k_z\right) = \overline{\overline{\varepsilon}}_{eff,A}\left(\omega, k_z\right) + \overline{\overline{\varepsilon}}_{eff,B}\left(\omega, k_z\right) - \varepsilon_h \overline{\overline{\mathbf{I}}}. \tag{2.3}$$

The permittivity tensor $\overline{\overline{\varepsilon}}_{eff,A+B}\left(\omega, k_z\right)$ is also of the form of Eq. (2.1), but now the *zz* component is given by:

$$\varepsilon_{zz} = 1 + \left[\frac{\varepsilon_h}{\left(\varepsilon_{m,A} - \varepsilon_h\right) f_{V,A}} - \frac{k_h^2 - k_z^2}{k_{p,A}^2} \right]^{-1} + \left[\frac{\varepsilon_h}{\left(\varepsilon_{m,B} - \varepsilon_h\right) f_{V,B}} - \frac{k_h^2 - k_z^2}{k_{p,B}^2} \right]^{-1}. \tag{2.4}$$

In what follows, the metal is assumed to be described by a lossless Drude dispersion model such that $\varepsilon_m\left(\omega\right) = \varepsilon_0\left(1 - \omega_m^2 / \omega^2\right)$, being ω_m the angular plasma frequency of the

electron gas within the metal. In such a case, the term $\frac{\varepsilon_h}{(\varepsilon_m-\varepsilon_h)f_V}$ can be simplified into $\frac{\varepsilon_h}{(\varepsilon_m-\varepsilon_h)f_V}\approx-\frac{\varepsilon_h}{\varepsilon_0 f_V}\frac{\omega^2}{\omega_m^2}=-\frac{k_h^2}{f_V k_m^2}$, with $k_m=\omega_m\sqrt{\mu_0\varepsilon_0}$. Hence, after simple mathematical manipulations, it is found that

$$\varepsilon_{zz}(\omega,k_z)=1-\frac{k_{ef,A}^2}{k_h^2-k_z^2/n_A^2}-\frac{k_{ef,A}^2}{k_h^2-k_z^2/n_A^2}. \tag{2.5}$$

where $n_l^2=1+\frac{k_{p,l}^2}{f_{V,l}k_{m,l}^2}$ with $l=A,B$ is the so-called slow-wave factor [21] that characterizes the plasmonic behavior of each set of wires, and $k_{ef,l}^2=k_{p,l}^2/n_l^2$ is the effective plasma wave number of each array, that takes into account both the geometry of the unit cell and the plasmonic response of the metallic wires. In case the wires are made of a perfect electrical conducting (PEC) material, the slow-wave factor is equal to unity, so that $n_l^2=1$ and therefore $k_{ef,l}^2=k_{p,l}^2$.

Next, we derive the photonic modes allowed in the bulk nested wire media. The characteristic equation for the photonic modes can be found substituting the permittivity tensor given by Eq. (2.4) into the Maxwell equations and calculating the plane-wave solutions (eigenmodes) with a spatial variation of the form $e^{i\mathbf{k}\cdot\mathbf{r}}$, being $\mathbf{k}=\mathbf{k}_t+k_z\hat{\mathbf{z}}$ and $\mathbf{k}_t=k_x\hat{\mathbf{x}}+k_y\hat{\mathbf{y}}$ the transverse part of the wave vector. This yields the following dispersion relation for TM (Transverse Magnetic)-polarized eigenwaves

$$k_z^2=k_h^2-\frac{k_x^2+k_y^2}{1-\frac{k_{ef,A}^2}{k_h^2-k_z^2/n_A^2}-\frac{k_{ef,B}^2}{k_h^2-k_z^2/n_B^2}} \tag{2.6}$$

and $k_z^2=k_h^2-k_x^2-k_y^2$ for the TE (Transverse Electric)-polarized waves. For a given value of the transverse part of the wave vector, the dispersion equation for TM-polarized waves given by Eq. (2.6) corresponds to a cubic equation, and therefore yields

three different solutions. Thus there are three distinct propagating eigenmodes: two quasi-Transverse Electromagnetic (q-TEM) modes and a TM mode. From here on these modes will be designated by qT1, qT2 and TM modes. Remarkably, this property contrasts with the standard wire medium which only supports two distinct extraordinary waves, the q-TEM mode and the TM mode [17, 21].

Clearly, each q-TEM mode is associated with a different array of wires [17, 21, 27]. This result can be generalized, so that for a metamaterial formed by *N* distinct wires arrays, there will be *N* different propagating q-TEM waves, provided the influence of each array on the others can be regarded as a macroscopic excitation.

II.2.2. Additional Boundary Conditions

In what follows, the theory developed in the previous section is applied to derive a formalism that allows one to characterize the scattering of electromagnetic waves by a slab of the nested wire media metamaterial with thickness *h*. A representative geometry of the system is sketched in Fig. 2.2. The slab is excited by a TM-polarized plane wave (magnetic field is along the *y*-direction) so that the plane of incidence is the *xoz* plane. The angle of incidence is θ_{inc} and the relevant field components are H_y, E_x and E_z. This monochromatic incoming wave can excite plane waves in the wire medium with transverse wave vector $\mathbf{k}_t = k_x\hat{\mathbf{x}} + k_y\hat{\mathbf{y}}$ such that $k_x = k_0 \sin\theta_{inc}$ and $k_y = 0$, with $k_0 = \omega/c$ and *c* the light speed in vacuum.

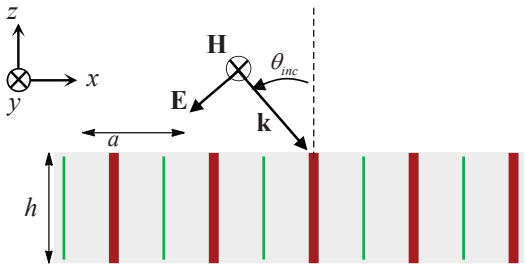

Fig. 2.2. Side view of the wire media slab formed by two nested sets of parallel wire arrays. The cells are arranged in a periodic square lattice with period a and both sets of wires are severed at the interfaces, forming a slab of thickness h. The structure is illuminated by a TM-polarized plane wave with incidence angle θ_{inc}.

The electromagnetic field inside the nested wire media may be written as a superposition of six plane waves: two counter-propagating waves (propagating along +z and –z directions, respectively) for each of the qT1, qT2 and TM modes. Thus, the magnetic field distribution in the whole space can be expressed as:

$$H_y(z,\omega) = e^{ik_x x}\frac{E^{inc}}{\eta_0}\begin{cases} \left(e^{\gamma_0 z} - Re^{-\gamma_0 z}\right) & z > 0 \\ C_1 e^{\gamma_{TM}(z+h)} + C_2 e^{-\gamma_{TM}(z+h)} + B_1 e^{\gamma_{qT2}(z+h)} + B_2 e^{-\gamma_{qT2}(z+h)} & \\ \qquad + A_1 e^{\gamma_{qT1}(z+h)} + A_2 e^{-\gamma_{qT1}(z+h)} & -h < z < 0 \\ Te^{\gamma_0(z+h)} & z < -h \end{cases} \quad (2.7)$$

where $A_{1,2}$ and $B_{1,2}$ stand for the amplitudes of the q-TEM modes, $C_{1,2}$ for the amplitude of the TM modes, E^{inc} is the complex amplitude of the incident field and $\eta_0 = \sqrt{\mu_0/\varepsilon_0}$. The reflection and transmission coefficients are R and T, and $\gamma_0 = \sqrt{k_t^2 - \omega^2\mu_0\varepsilon_0}$ is the free space propagation constant along the z-direction. The propagation constants along the z-direction in the metamaterial ($\gamma^2 = -k_z^2$ with $\gamma = \gamma_{qT1}, \gamma_{qT2}, \gamma_{qTM}$) are obtained from the solution of the dispersion characteristic equation (2.6) with $\mathbf{k} = \mathbf{k}_t + k_z\hat{\mathbf{z}}$ and $\mathbf{k}_t = k_x\hat{\mathbf{x}}$.

To determine the unknowns $A_{1,2}$, $B_{1,2}$, $C_{1,2}$, R, and T a set of suitable boundary conditions need to be imposed at the interfaces between the metamaterial slab and the air regions. The boundary conditions depend on the manner in which the metallic wires are terminated at the interfaces. In this thesis, it will be assumed that the wires are cut at the interfaces.

The classical Maxwellian boundary conditions establish a relation between the tangential components of the electric and magnetic fields at the interfaces. In the considered configuration, the tangential electric field is continuous at the interface because there is no effective surface magnetization (or higher-order surface multipole densities) at the interface. Moreover, the tangential magnetic field is also continuous since no electric surface currents are present.

It is well known that due to the strong nonlocal behavior of wire media, additional boundary conditions must be specified at the interfaces of a material slab [22, 35-38]. However, since in a unit cell of the nested wire media there are two independent sets of wires, two additional boundary conditions are required at each interface. The formulation of these boundary conditions will be based on the ideas of Ref. [27]. Because we assume that the wires are severed at the interfaces, the microscopic current flowing on each of the metallic wires I_l, with $l = A, B$ representing each set of wires, must vanish at the interface, i.e. at an interface $z = z_0$ one should have $I_l = 0$. Since the contribution $\mathbf{P}_l$ of the sub-array l to the total polarization vector may be written as a function of the current flowing on each of the metallic wires so that $\mathbf{P}_l = \frac{1}{-i\omega}\frac{I_l}{a^2}\hat{\mathbf{z}}$, it follows that the boundary condition $I_l = 0$ at $z = z_0$ is equivalent to $\mathbf{P}_l \cdot \hat{\mathbf{z}}\big|_{z=z_0} = 0$.

Importantly, from Eq. 2.2, the previous boundary condition may also be rewritten as

$$\left[\varepsilon_{zz,l}\left(\omega,-i\frac{d}{dz}\right)-1\right]E_z\Big|_{z=z_0}=0.$$

In summary, the boundary conditions at the interfaces between the metamaterial slab and the air regions are:

$$\lfloor E_x \rfloor_{z=0,-h}=0, \tag{2.8a}$$

$$\lfloor H_y \rfloor_{z=0,-h}=0, \tag{2.8b}$$

$$\left[\varepsilon_{zz,l}\left(\omega,-i\frac{d}{dz}\right)-1\right]E_z\Big|_{z=0,-h}=0,\ l=A,B. \tag{2.8c}$$

Here $\lfloor F \rfloor_{z=z_0}=F_{z=z_0^+}-F_{z=z_0^-}$ stands for the field discontinuity of the generic function F at the pertinent interface. The electric field distribution may be obtained using $\mathbf{E}=\frac{1}{-i\omega}\left[\overline{\overline{\varepsilon}}\left(\omega,-i\frac{d}{dz}\right)\right]^{-1}\cdot\nabla\times\mathbf{H}$, and it satisfies:

$$E_x(z,\omega)=e^{ik_x x}\frac{E^{inc}}{\eta_0}\frac{1}{i\omega\varepsilon_0}\begin{cases}\gamma_0\left(e^{\gamma_0 z}+Re^{-\gamma_0 z}\right) & z>0,\\ \frac{\varepsilon_0}{\varepsilon_h}\gamma_{TM}\left(C_1e^{\gamma_{TM}(z+h)}-C_2e^{-\gamma_{TM}(z+h)}\right)+\frac{\varepsilon_0}{\varepsilon_h}\gamma_{qT2}\left(B_1e^{\gamma_{qT2}(z+h)}-B_2e^{-\gamma_{qT2}(z+h)}\right) & \\ +\frac{\varepsilon_0}{\varepsilon_h}\gamma_{qT1}\left(A_1e^{\gamma_{qT1}(z+h)}-A_2e^{-\gamma_{qT1}(z+h)}\right) & -h<z<0,\\ \gamma_0Te^{\gamma_0(z+h)} & z<-h\end{cases} \tag{2.9}$$

$$E_z(z,\omega)=-e^{ik_x x}\frac{E^{inc}}{\eta_0}\frac{k_x}{\omega\varepsilon_0}\begin{cases}e^{\gamma_0 z}-Re^{-\gamma_0 z} & z>0\\ \frac{\varepsilon_0}{\varepsilon_{zz}^{TM}}\left(C_1e^{\gamma_{TM}(z+h)}+C_2e^{-\gamma_{TM}(z+h)}\right)+\frac{\varepsilon_0}{\varepsilon_{zz}^{qT2}}\left(B_1e^{\gamma_{qT2}(z+h)}+B_2e^{-\gamma_{qT2}(z+h)}\right) & \\ +\frac{\varepsilon_0}{\varepsilon_{zz}^{qT1}}\left(A_1e^{\gamma_{qT1}(z+h)}+A_2e^{-\gamma_{qT1}(z+h)}\right) & -h<z<0\\ Te^{\gamma_0(z+h)} & z<-h\end{cases}. \tag{2.10}$$

In the above $\varepsilon_{zz}^{TM}=\varepsilon_h\varepsilon_{zz}\left(\omega,i\gamma_{TM}\right)$, $\varepsilon_{zz}^{qT1}=\varepsilon_h\varepsilon_{zz}\left(\omega,i\gamma_{qT1}\right)$, and $\varepsilon_{zz}^{qT2}=\varepsilon_h\varepsilon_{zz}\left(\omega,i\gamma_{qT2}\right)$ where $\varepsilon_{zz}\left(\omega,k_z\right)$ is given by Eq. (2.5).

Imposing the boundary conditions (2.8a), (2.8b) and (2.8c) on the each of the sub-arrays ($l = A, B$) at the top and bottom interfaces, allows us to obtain a set of eight linear equations that can be numerically solved to obtain the value of all unknowns and therefore solve the scattering problem.

It is important to stress that in agreement with the findings reported in Ref. [25], for lossless structures these boundary conditions are consistent with the conservation of energy and with continuity of the real part of the Poynting vector component normal to the interfaces (please see Appendix B of the article [J2]). Moreover, it is worth mentioning that in the article [J2] we also derived boundary conditions for the configuration where the wires are connected to square metallic patches, so that all the wires in the same sub-array are terminated in the same manner at both interfaces, but wires in different arrays can be terminated differently.

II.3. Fano Resonances

In order to demonstrate the validity of the proposed effective medium model and prove that the coupling of the wire arrays results in the emergence of Fano resonances, next the transmission and reflection properties of nested wire media are calculated for different examples. The wires are embedded in a dielectric medium with thickness h and permittivity ε_h, and the set wires of sub-array *A* have radius R_A, whereas the wires of sub-array *B* have radius R_B. The geometry is shown in Fig. 2.3.

We suppose that the slab has thickness $h = 3a$ and that the wires stand in air so that $\varepsilon_h = \varepsilon_0$. The wire radii are $R_A = 0.05a$ and $R_B = 0.025a$, for each of the sub-arrays. The slab is illuminated by a TM-polarized plane wave with incidence angle $\theta_{inc} = 60^\circ$.

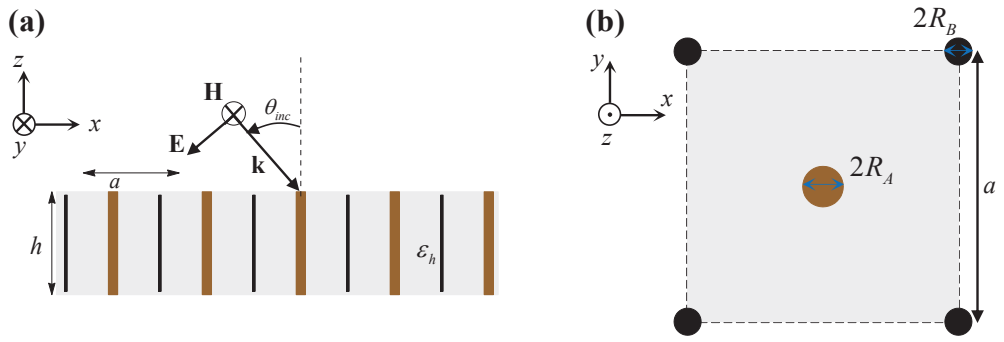

Fig. 2.3. Geometry of the wire media slab formed by two nested sets of parallel wire arrays **(a)** Side view: the cells are arranged in a periodic square lattice with period a. Both sets of wires are severed at the interfaces. The wires are embedded in a dielectric with permittivity ε_h and thickness h. The structure is illuminated by a TM-polarized plane wave with incidence angle θ_{inc}. **(b)** Top view of the unit cell of a 2D lattice of wire medium slab with one wire with radius R_A in the middle and another wire with radius R_B placed in the corners of the cell.

II.3.1. Nested Wire Wedia with Perfect Electric Conducting Wires

To begin with, it is supposed that the wires of both sub-arrays are made of an ideal PEC material. In this case the propagation constants associated with the two q-TEM modes become identical such that $\gamma_{qT1} = \gamma_{qT2} = -ik_h$. As a consequence, it is clear that $\varepsilon_{zz}^{qT1} = \varepsilon_{zz}^{qT2} = \infty$, and hence the system of equations obtained by imposing the boundary conditions (2.8a), (2.8b) and (2.8c) on the each of the sub-arrays at the top and bottom interfaces of the slab is ill-defined. This difficulty can be circumvented simply by slightly numerically perturbing the complex permittivity of the materials. The numerical perturbation was modeled in such a way that the slow wave factor of the sub-arrays was $n_{A,B}^2 = 1 + \delta_{A,B}$, with $\delta_{A,B} << 1$. It was checked, both numerically and analytically, that independent of the considered perturbation, the reflection and transmission coefficients converge to the same result independent of the form of the perturbation when $\delta_{A,B} \to 0$. In general, one may need to adopt this perturbative approach when the propagation constants of the two q-TEM modes are identical, even if each set of wires is terminated asymmetrically.

Figure 2.4 depicts the amplitude and phase of both the transmission (panel **(a)**) and reflection (panel **(b)**) coefficients of the nested wire media slab as a function of the normalized frequency $h\omega/c$, calculated using the developed homogenization model and using the commercial full-wave electromagnetic simulator CST Microwave Studio [39].

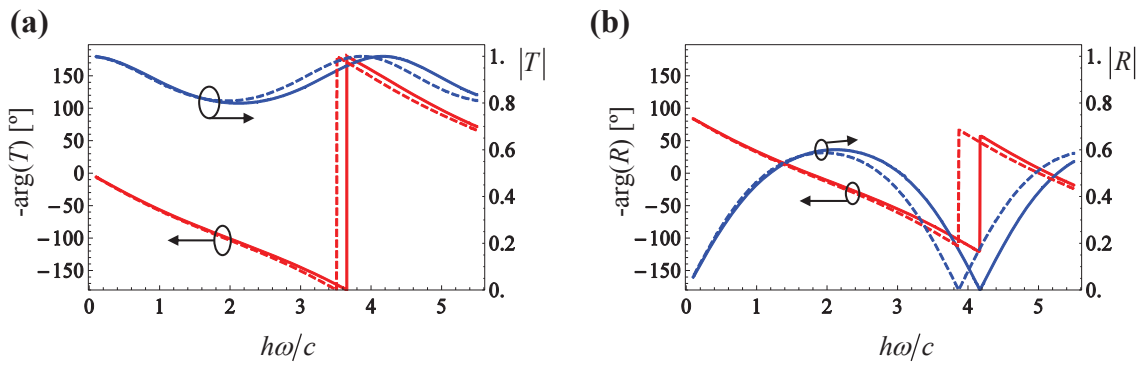

Fig. 2.4. Amplitude (blue curves) and phase (red curves) of the **(a)** transmission and **(b)** reflection coefficients for PEC wires and an incident TM polarized wave with $\theta_{inc} = 60^{o}$ as a function of the normalized frequency $h\omega/c$. The solid lines represent the results calculated using the homogenization model and the dashed lines represent the full wave results obtained with CST Microwave Studio.

The results show that there is a good agreement between the results obtained using the homogenization model and the full-wave simulations, indicating that the proposed effective medium theory accurately describes the electromagnetic response of the nested wire media when the wires are made of a PEC material.

Importantly, even though there is some asymmetry in the system, since both sub-arrays have different radii ($R_A = 0.05a$ and $R_B = 0.025a$), this is not sufficient to observe Fano resonances in the scattering properties of the nested wire media. For reasons that will be discussed ahead, to observe such a phenomenon, it is necessary to increase the asymmetry between both sub-arrays, for instance connecting metallic plates to one set of wires at the interface [J2].

II.3.2. Nested Wire Media with Dispersive Metallic Wires

In the next example, we suppose that the permittivity of the metals $\varepsilon_m(\omega)$ is described by the lossless Drude dispersion model such that $\varepsilon_m(\omega)=\varepsilon_0\left(1-\omega_m^2/\omega^2\right)$. It is assumed that the wires of array A have a plasma frequency that satisfies $k_{m,A}a=\left(\omega_{m,A}/c\right)a=19.5$, which for a lattice period of $a=273\,\mu\text{m}$ corresponds to the plasma frequency of indium antimonide at 225 K [40]. Moreover, it is considered that the wires of array B are made of a material such that $k_{m,B}a=\left(\omega_{m,B}/c\right)a=10.0$, consistent with the plasma frequency of $0.92\,\Omega\,cm$ p-type doped silicon [41]. As in the previous example, the remaining structural parameters are $h=3a$, $R_A=0.05a$ and $R_B=0.025a$, while the slab is illuminated by a TM-polarized plane wave with incidence angle $\theta_{inc}=60^\text{o}$.

A comparison between the results obtained with the homogenization model and full wave simulation is shown in panels **(a)** and **(b)** of Fig. 2.5.

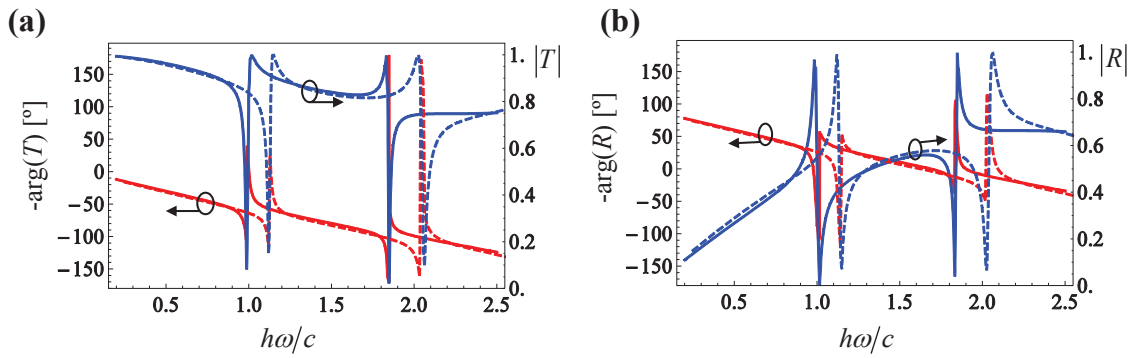

Fig. 2.5. Amplitude (blue curves) and phase (red curves) of the **(a)** transmission and **(b)** reflection coefficients as a function of the normalized frequency $h\omega/c$, for a nested wire media slab where the wires of sub-arrays A and B are made of metals such that for a lattice period of $a=273\,\mu m$ the normalized plasma frequencies satisfy $k_{m,A}a=19.5$ and $k_{m,B}a=10.0$ under the excitation of an incident TM polarized wave with $\theta_{inc}=60^\text{o}$. The solid lines represent the results calculated using the homogenization model and the dashed lines represent the full wave results obtained with CST Microwave Studio.

Apart from a frequency shift, the results show a reasonable agreement, further validating our theory when the metallic wires are made of distinct materials. An eye catching feature in the plots is the presence of a sharp resonance in the transmission and reflection coefficients near the normalized frequency $h\omega/c \approx 1.0$, whose asymmetric shape is consistent with a Fano-type resonance and is markedly different from the more common Lorentzian resonance [28, 29]. The emergence of this resonance is related to the interference between a narrow quadrupole-type resonance and a broad dipole-type resonance [34]. In fact, it can be checked that to a first approximation electrically short (subwavelength) wires behave as electric dipoles, such that their scattering strength typically increases with the frequency. Therefore, the scattering of the wire arrays is dominated by the strongly radiative collective dipolar mode originated from the in-phase interference of the fields that are scattered by the two wire sub-arrays, and in particular, for long wavelengths, the transmission of the structure tends to decrease with an increasing frequency, as shown in both Fig. 2.4**(a)** and Fig. 2.5**(a)**. However, in the nested wire medium, where there are two distinct wires in the unit cell, the currents in the wires may have opposite signs over a narrow frequency range, resulting in a narrow anti-bonding mode. The Fano resonance emerges precisely at the frequency wherein the dipole moments of each array oscillate out of phase. At this frequency the net dipole moment is null, which results in a sub-radiant mode and in nearly 100% transmission of the incoming wave.

These ideas are illustrated in Fig. 2.6, where it is shown the phase and normalized amplitude of the *z*-component of the polarization vector P_z of each sub-array of wires, calculated at the midpoint of the wire media slab using Eq. 2.2, as a function of the normalized frequency.

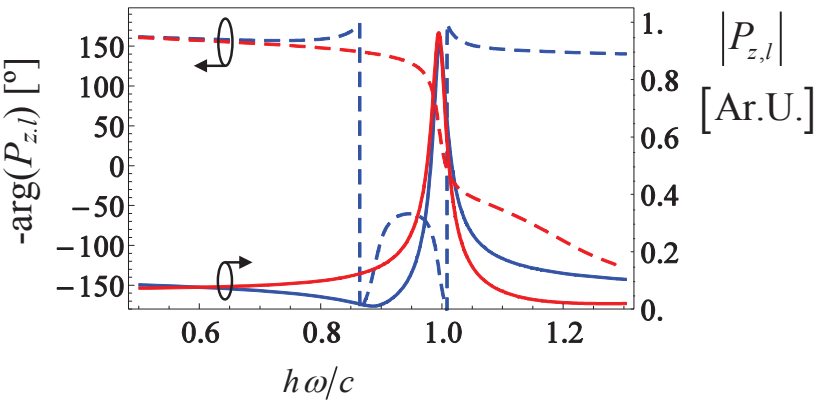

Fig. 2.6. Normalized amplitude (solid curves) and phase (dashed curves) and of the *z*-component of the macroscopic polarization vector of each sub-array of wires at the middle of the slab as a function of the normalized frequency: polarization vector of sub-mesh *A* (blue curves) and polarization vector of sub-mesh *B* (red curves). The amplitude of the incident wave is constant.

It is seen that at the peak of transmission corresponding to the Fano resonance, occurring at the normalized frequency $h\omega/c \approx 1.0$, not only the polarization vectors are out of phase, but also that they have nearly the same amplitude, confirming that the net polarization vector vanishes at the Fano resonance. For slightly different frequencies, the amplitudes of the polarization vectors are not the same, causing the dips in the amplitude transmission coefficient.

Interestingly, the results show that for frequencies slightly above $h\omega/c \approx 1.0$ the amplitude of the polarization vector is higher in the sub-array of wires with larger radius, whereas at frequencies smaller than $h\omega/c \approx 1.0$ the amplitude of the polarization vector is typically larger in the sub-array of wires with smaller radius. In fact, for slightly smaller operating frequencies the sub-arrays are characterized by a very strong dipolar response, and the currents flowing through the wires do not oscillate in opposition of phase, forcing the dip in the amplitude of the transmission coefficient.

These ideas are substantiated in Fig. 2.7, where we show the phase and normalized amplitude of the *z*-component of the polarization vector P_z of each sub-array of wires, calculated inside the wire media slab at fixed frequencies $h\omega/c \approx 1.0$ (solid blue curves

for sub-mesh *A* and long dashed red curves for sub-mesh *B*) and at $h\omega/c \approx 0.987$ (green dotted curves for sub-mesh *A* and dot-dashed brown curves for sub-mesh *B*).

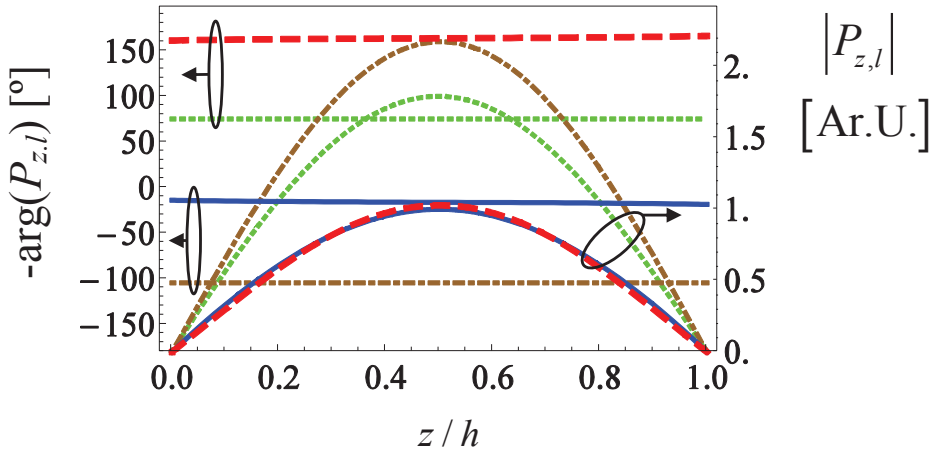

Fig. 2.7. Phase and normalized amplitude of the *z*-component of the macroscopic polarization vector of each sub-array of wires inside the wire media slab at $h\omega/c \approx 1.0$ (solid blue curves for sub-mesh *A* and long dashed red curves for sub-mesh *B*) and at $h\omega/c \approx 0.987$ (green dotted curves for sub-mesh *A* and dot-dashed brown curves for sub-mesh *B*).

In fact, while at the normalized frequency $h\omega/c \approx 1.0$ the *z*-component of the polarization vector of each sub-array of wires has nearly the same amplitude but opposite signs across the slab, at a slightly smaller frequency $h\omega/c \approx 0.987$ this does not happen and the amplitude of the *z*-component of the polarization vector of the sub-mesh *B* is always larger than in the sub-mesh *A*, i.e. $|P_{z,B}|$ is always larger than $|P_{z,A}|$.

To further demonstrate that the nature of the Fano resonance lies in the asymmetry of the structure, we depict, in Fig. 2.8 normalized microscopic current density flowing through the wires in the unit cell at the normalized frequencies $h\omega/c = 1.15$ and at $h\omega/c = 2.06$. These normalized frequencies correspond to peaks of transmission calculated with Microwave Studio [39] that are depicted in Fig. 2.5.

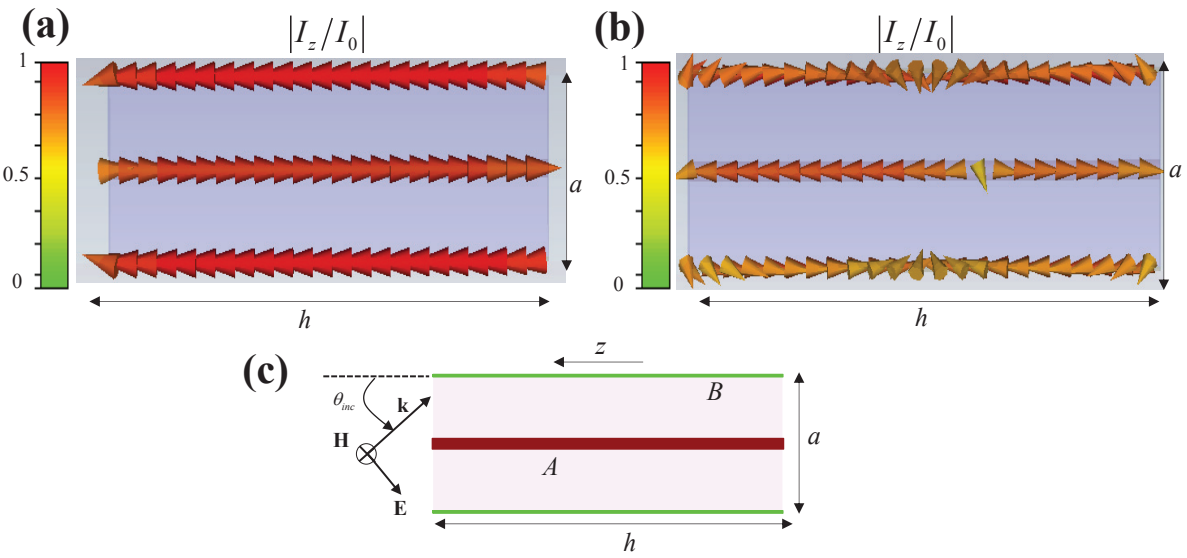

Fig. 2.8. Normalized microscopic current density distribution in a unit cell of the nested wire medium structure for the normalized frequencies: **(a)** $h\omega/c = 1.15$ and **(b)** $h\omega/c = 2.06$. Panel **(c)** shows the geometry of the unit cell.

Figure 2.8**(a)** reveals that the currents in the two wire arrays have nearly the same amplitude and are out of phase, demonstrating in this manner that the narrow-band Fano resonance is rooted in the counter-flow of microscopic currents in each set of wires. These results also allow concluding that the narrow anti-bonding mode is related to quadrupole/magnetic resonances, and that nested wires slab may mimic an array of magnetic dipoles that oscillate along the *y*-direction. In fact, since the Fano resonance is originated from the interaction of an electric-type resonance and magnetic-type resonance (more rigorously a mix of magnetic and quadrupolar resonances), the nested wire medium may be roughly pictured as a material with an effective permittivity and an effective permeability that resonate at nearby frequencies.

In this system the Fano resonance emerges from the interaction of two different resonators (two different wire arrays), but it has also been proposed that Fano resonances may appear due to the interaction of different modes of the same resonator [34, 42].

On the other hand, at the second resonance, corresponding to the normalized frequency $h\omega/c = 2.06$, the currents do not flow along a single direction in each wire, so that the wires cannot be regarded as a short dipoles.

II.4. Summary

In this chapter, we investigated the effective medium response of two nested arrays of parallel metallic wires. Under the assumption that the two sub-arrays are not very strongly coupled in the near-field, we derived an explicit formula for the effective dielectric constant of the bulk metamaterial which depends on both the geometry of the cell and the plasmonic behavior of the permittivity of the metallic wires. It was also shown that the dispersion relation for TM-polarized waves in the nested wire media yields three different solutions, corresponding to two q-TEM modes and a TM mode, which contrasts with the standard wire medium that only supports two distinct extraordinary waves, the q-TEM mode and the TM mode [17, 21].

One of the main contributions of this Chapter is the development of a formalism to solve scattering problems in a slab of nested wire media when the wires are severed at the interfaces. This formalism was successfully applied to the study of the scattering of electromagnetic plane waves by a slab of the metamaterial. It was shown that the two arrays can be strongly coupled and that the currents in the two sets of wires may flow in opposite directions. The aforementioned phenomenon enables the interference of a narrow quadrupole-type resonance and a broad dipole-type resonance, resulting in a Fano-type resonance in the transmission and reflection coefficients of the slab. Remarkably it was shown that it is necessary to have some degree of asymmetry in the structure for this resonance to appear, and that a possibility is to consider wires made of distinct materials.

It is important to stress that this work was further developed in [J2] for a configuration wherein the wires are connected to square metallic patches, so that all the wires in the same sub-array are terminated in the same manner at both interfaces but wires in different arrays can be terminated differently.

References

[1] J. B. Pendry, A. J. Holden, W. J. Stewart, and I. Youngs, "Extremely Low Frequency Plasmons in Metallic Mesostructures", *Phys. Rev. Lett.* **76**, 4773, 1996.

[2] S. I. Maslovski, S. A. Tretyakov, P. A. Belov, "Wire media with negative effective permittivity: A quasi-static model", *Microwave Opt. Tech. Lett.* **35**, 47, 2002.

[3] S. I. Maslovski, and M. G. Silveirinha, "Ultralong-range Casimir-Lifshitz forces mediated by nanowire materials", *Phys. Rev. A* **82**, 022511, 2010.

[4] S. I. Maslovski, and M. G. Silveirinha, "Mimicking Boyer's Casimir repulsion with a nanowire material", *Phys. Rev. A* **83**, 022508, 2011.

[5] T. A. Morgado, S. I. Maslovski, M. G. Silveirinha, "Ultrahigh Casimir Interaction Torque in Nanowire Systems", *Opt. Express* **21**, 14943, 2013.

[6] C. R. Simovski, P. A. Belov, A. V. Atrashchenko, and Y. S. Kivshar, "Wire metamaterials: physics and applications.", *Adv.Mater.* **24**, 4229, 2012.

[7] D. R. Smith, and D. Schurig, "Electromagnetic Wave Propagation in Media with Indefinite Permittivity and Permeability Tensors", *Phys. Rev. Lett.* **90**, 077405, 2003.

[8] M. G. Silveirinha, "Broadband negative refraction with a crossed wire mesh", *Phys. Rev. B* **79**, 153109, 2009.

[9] S. A. Tretyakov, and S. I. Maslovski, "Thin absorbing structure for all incidence angles based on the use of a high-impedance surface", *Microwave Opt. Tech. Lett.* **38**, 175, 2003.

[10] M. G. Silveirinha, "Anomalous Refraction of Light Colors by a Metamaterial Prism", *Phys. Rev. Lett.* **102**, 193903, 2009.

[11] P. A. Belov, G. K. Palikaras, Y. Zhao, A. Rahman, C. R. Simovski, Y. Hao, and C. Parini, "Experimental demonstration of multiwire endoscopes capable of manipulating near-fields with subwavelength resolution", *Appl. Phys. Lett.* **97**, 191905, 2010.

[12] T. A. Morgado, J. S. Marcos, M. G. Silveirinha, and S. I. Maslovski, "Experimental Verification of Full Reconstruction of the Near-Field with a Metamaterial Lens", *Appl. Phys. Lett.* **97**, 144102, 2010.

[13] S. Paulotto, P. Baccarelli, P. Burghignoli, G. Lovat, G.W. Hanson, and A.B. Yakovlev, "Homogenized Green's functions for an aperiodic line source over planar densely periodic artificial impedance surfaces", *IEEE Trans. Microwave Theory Tech.* **58**, 1807, 2010.

[14] T. A. Morgado, J. S. Marcos, M. G. Silveirinha, and S. I. Maslovski, "Ultraconfined Interlaced Plasmons", *Phys. Rev. Lett.* **107**, 063903, 2011.

[15] J. T. Costa, and M. G. Silveirinha, "Achromatic Lens Based on a Nanowire Material with Anomalous Dispersion", *Optics Express* **20**, 13915, 2012.

[16] P. A. Belov, R. Marques, S. I. Maslovski, I. S. Nefedov, M. Silveirinha, C. R. Simovski, and S. A. Tretyakov, "Strong spatial dispersion in wire media in the very large wavelength limit", *Phys. Rev. B* **67**, 113103, 2003.

[17] M. G. Silveirinha, "Nonlocal homogenization model for a periodic array of ε-negative rod", *Phys. Rev. E* **73**, 046612, 2006.

[18] A. Demetriadou, and J.B. Pendry, "Taming spatial dispersion in wire metamaterial", *Phys. Condens. Matter* **20**, 295222, 2008.

[19] O. Luukkonen, M. G. Silveirinha, A. B. Yakovlev, C. R. Simovski, I. S. Nefedov, and S. A. Tretyakov, "Effects of Spatial Dispersion on Reflection from Mushroom-type Artificial Impedance Surfaces", *IEEE Trans. Microwave Theory Tech.* **57**, 2692, 2009.

[20] A. B. Yakovlev, M. G. Silveirinha, O. Luukkonen, C. R. Simovski, I. S. Nefedov, and S. A. Tretyakov, "Characterization of Surface-Wave and Leaky-Wave Propagation on Wire-Medium Slabs and Mushroom Structures Based on Local and Non-Local Homogenization Models", *IEEE Trans. Microwave Theory Tech.* **57**, 2700, 2009.

[21] S. I. Maslovski, and M. G. Silveirinha, "Nonlocal permittivity from a quasistatic model for a class of wire media", *Phys. Rev. B* **80**, 245101, 2009.

[22] S. I. Maslovski, T. A. Morgado, M. G. Silveirinha, C. S. R. Kaipa, and A. B. Yakovlev, "Generalized additional boundary conditions for wire media", *New J. Phys.* **12**, 113047, 2010.

[23] J. Shin, J.-T. Shen, and S. Fan, "Three-dimensional electromagnetic metamaterials that homogenize to uniform non-Maxwellian media", *Phys. Rev B* **76**, 113101, 2007.

[24] M. G. Silveirinha, and C. A. Fernandes, "Nonresonant structured material with extreme effective parameters", *Phys. Rev. B* **78**, 033108, 2008.

[25] M. G. Silveirinha, "Additional Boundary Conditions for Nonconnected Wire Media", *New J. Phys.* **11**, 113016, 2009.

[26] M. G. Silveirinha, "Artificial plasma formed by connected metallic wires at infrared frequencies", *Phys. Rev. B* **79**, 035118, 2009.

[27] G. W. Hanson, E. Forati, and M. G. Silveirinha, "Modeling of spatially-dispersive wire media: transport representation, comparison with natural materials, and additional boundary conditions", *IEEE Trans. on Antennas and Propagat.* **60**, 4219, 2012.

[28] U. Fano, "Effects of configuration interaction on intensities and phase shifts", *Phys. Rev.* **124**, 1866, 1961.

[29] A. E. Miroshnickenko, S. Flach, and Y. S. Kivshar, "Fano resonances in nanoscale structures", *Rev. Mod. Phys.* **82**, 2257, 2010.

[30] U. Fano, "Sullo spettro di assorbimento dei gas nobili presso il limite dello spettro d'arco", *Nuovo Cimento* **12**, 154, 1935.

[31] H. Beutler, "Über absorptionsserien von argon, kryptonund xenon zu termen zwischen den beiden ionisierungsgrenzen $^2P_3^{2/0}$ und $^2P_1^{2/0}$", *Z. Phys. A* **93**, 177, 1935.

[32] V. A. Fedotov, M. Rose, S. L. Prosvirnin, N. Papasimakis, and N. I. Zheludev, "Sharp Trapped-Mode Resonances in Planar Metamaterials with a Broken Structural Symmetry", *Phys. Rev. Lett.* **99**, 147401, 2007.

[33] N. A. Mirin, K. Bao, and P. Nordlander, "Fano Resonances in Plasmonic Nanoparticle Aggregates", *J. Phys. Chem. A* **113**, 4028, 2009.

[34] B. Luk'yanchuk, N. I. Zheludev, S. A. Maier, N. J. Halas, P. Nordlander, H. Giessen, and C. T. Chong, "The Fano resonance in plasmonic nanostructures and metamaterials", *Nat. Mater*. **9**, 707, 2010.

[35] M. G. Silveirinha, "Additional Boundary Condition for the Wire Medium", *IEEE Trans. on Antennas and Propag.* **54**, 1766, 2006.

[36] M. G. Silveirinha, C. A. Fernandes, and J. R. Costa, "Additional Boundary Condition for a Wire Medium Connected to a Metallic Surface", *New J. Phys.* **10**, 053011, 2008.

[37] C. S. R. Kaipa, A. B. Yakovlev , S. I. Maslovski, and M. G. Silveirinha, "Indefinite dielectric response and all-angle negative refraction in a structure with deeply-subwavelength inclusions", *Phys. Rev. B* **84**, 165135, 2011.

[38] C. S. R. Kaipa, A. B. Yakovlev , S. I. Maslovski, and M. G. Silveirinha, "Mushroom-type High-Impedance Surface with Loaded Vias: Homogenization Model and Ultra-Thin Design", *IEEE Antennas and Wireless Propag. Lett.* **10**, 1503, 2011.

[39] CST GmbH 2014 CST Microwave Studio http://www.cst.com.

[40] J. G. Rivas, C. Janke, P. Bolivar, and H. Kurz, "Transmission of THz radiation through InSb gratings of subwavelength apertures", *Opt. Express* **13**, 847, 2005.

[41] M. van Exter, and D. Grischkowsky, "Optical and electronic properties of doped silicon from 0.1 to 2 THz", *Appl. Phys. Lett.* **56**, 1694, 1990.

[42] M. Sarrazin, J.-P. Vigneron, and J.-M. Vigoureux, "Role of Wood anomalies in optical properties of thin metallic films with a bidimensional array of subwavelength holes", *Phys.Rev. B* **67**, 085415, 2003.

III. CHERENKOV EMISSION IN WIRE MEDIA

III.1. Introduction

Cherenkov radiation [1] is emitted whenever a charged particle moves inside a transparent medium with a velocity v larger than the phase velocity $v_{\mathrm{ph}} = c/n$ of the electromagnetic waves inside the medium, where n is the refractive index of the medium. If the velocity threshold is surpassed, the emitted radiation forms a cone of rays inclined at an angle θ with respect to the direction of motion such that $\theta = \arccos\left(v_{\mathrm{ph}} / v\right)$. Hence, the particle velocity can be determined based upon the angle of the emitted radiation. This phenomenon was discovered by P. A. Čerenkov in 1934 while studying the effects of radioactive substances on liquids, as he noticed that the water surrounding certain radioactive substances emitted a faint blue glow. Soon after this discovery, in 1937, I. M. Frank and I. E. Tamm put forward a theoretical interpretation of Čerenkov's observations [2]. Since then, Cherenkov radiation has been extensively studied due to its many applications, particularly in particle detection in high-energy physics [3].

Quite interestingly, this phenomenon is intimately linked to the beginning of metamaterials research. The history of modern metamaterials can be traced back to 1968, when Victor Veselago published a pioneering study [4] proposing that DNG media would allow for left-handed propagation of light and an anomalous Cherenkov effect, where the cone of the radiation would be directed backward relative to the motion of the particle, different from what is observed in usual materials [1, 2, 5].

It took nearly forty years for the anomalous Cherenkov effect to be experimentally verified [7], even if in an indirect manner. Recently the study of Cherenkov emission gained a new breath with the emergence of novel functional materials with tailored electromagnetic response [7-17]. For instance, it has been suggested that metamaterials enable the emission of Cherenkov radiation with no velocity threshold [8, 9, 12, 13].

In Chapter II it was shown that a nanowire metamaterial may support Fano resonances and this can have exciting applications in sensing. Here we explore the potentials of nanowire arrays in context of Cherenkov emission. The main motivation to study this problem is related to the recent finding [18-20] that an array of nanowires in the long wavelength limit $\lambda >> a$ (a is the period of the structure) [21] is characterized by an extremely large density of photonic states, allowing to boost the Casimir interaction between two bodies embedded in a nanowire environment. It is important to mention that singularities in the density of photonic states have also been associated to a significant increase in the Purcell emission rate [22-26] of indefinite media (such that the permittivity tensor is indefinite). Therefore, it is natural to wonder how would the large density of photonic states affect the Cherenkov emission.

Here, based on an effective medium framework, an analytical model is developed to calculate the Cherenkov radiation emitted by a linear array of charges moving with constant velocity inside an infinite nanowire structure. The model is used to prove that the Cherenkov emission in nanowire materials has maximal intensity along a very specific direction, and that unlike natural materials it has no velocity threshold.

The enhancement of the Cherenkov emission is discussed in detail. Explicit analytical formulas are derived to compare the radiation losses associated with the emission of Cherenkov radiation in an unbounded nanowire structure and in a natural material. It is shown that the wire media may greatly enhance the emission of radiation

as compared to water, a dielectric widely used in the context of Cherenkov radiation detectors [27-28].

III.2. Pencil of Charges Moving Inside the Nanowire Structure

III.2.1. Analytical Model

In what follows, an analytical model is developed to calculate the field distribution of the Cherenkov radiation emitted by a linear array of charges, or "pencil" of charges, moving inside an unbounded wire medium, and whose movement is confined to the $y = 0$ plane, as shown in Fig. 3.1. In the proposed configuration the pencil of charges is oriented along the *z*-direction, so that at a fixed instant of time, all charges have the same y coordinate and move along the x-direction with a constant velocity *v*. The nanowire structure consists of a set of infinitely long wires arranged in a periodic square lattice with period *a*, and oriented along the *y*-direction. The metallic wires have radius r and are embedded in a dielectric medium with relative dielectric permittivity ε_h, as depicted in Fig. 3.1. The relative complex permittivity of the metallic wires is ε_m.

From the discussion in Sec. II.2, the effective permittivity tensor of the wire medium may be written as:

$$\varepsilon_{eff} = \varepsilon_h \begin{pmatrix} \varepsilon_t & 0 & 0 \\ 0 & \varepsilon_{yy} & 0 \\ 0 & 0 & \varepsilon_t \end{pmatrix} \tag{2.1}$$

where $\varepsilon_{yy} = 1 + \left[\dfrac{\varepsilon_h}{(\varepsilon_m - \varepsilon_h) f_V} - \dfrac{k_h^2 - k_y^2}{k_p^2} \right]^{-1}$ and $\varepsilon_t \approx 1$ [29, 30].

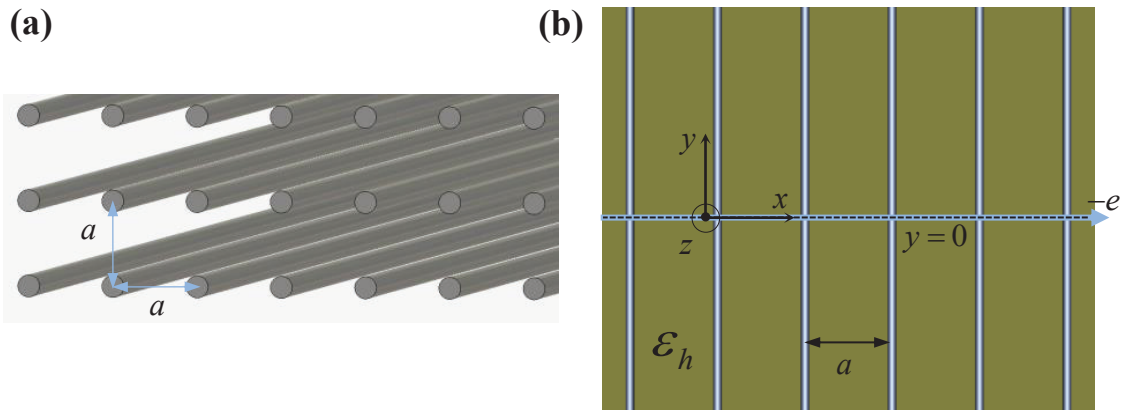

Fig. 3.1. (a) Geometry of the infinite wire medium with period a, embedded in a dielectric host material with permittivity ε_h. **(b)** A linear array of charges moves inside an unbounded wire medium with a constant velocity v.

The spatial distribution of the electromagnetic field in the wire medium can be obtained from the solution of the Maxwell equations:

$$\partial \mathbf{B}/\partial t + \nabla \times \mathbf{E} = 0\,, \tag{2.2}$$

$$\nabla \times \mathbf{H} - \varepsilon_0 \frac{\partial \mathbf{E}}{\partial t} = \mathbf{J}_t\,, \tag{2.3}$$

and allows for the complete characterization of the Cherenkov radiation in the structure. The source term $\mathbf{J}_t = \mathbf{J}_{ext} + \mathbf{J}_{wm}$ represents the total current density in the system, taking into account the contributions from the moving charges $\mathbf{J}_{ext}$ and the current that is induced in the structured material $\mathbf{J}_{wm}$. In this problem, the current density of the moving charges is given by:

$$\mathbf{J}_{ext}(x,y,t) = -en_z\delta(y)\delta\left(\frac{x}{v} - t\right)\hat{\mathbf{x}} \tag{2.4}$$

where n_z is the number of charges per unit of length along the z-direction and $-e$ is the electron charge. The volumetric charge density is determined by the divergence of this current. Since the electromagnetic fields can be found most easily in the frequency domain, it is useful to calculate the Fourier transform of $\mathbf{J}_{ext}(x,y,t)$:

$$\mathbf{J}_{ext}(x,y,\omega)=\int_{-\infty}^{+\infty}\mathbf{J}_{ext}\left(x,y,t\right)e^{i\omega t}dt=-en_z\delta\left(y\right)e^{ik_x x}\hat{\mathbf{x}} \tag{2.5}$$

where $k_x=\omega/v$. The current density $\mathbf{J}_{wm}$ is the average current induced in the nanowire metamaterial, and hence is defined as $J_{y,wm}=I_y/a^2$, where I_y is the microscopic current in a nanowire [31]. As proven in Ref. [31, 32], it is possible to write I_y directly in terms of the macroscopic fields as:

$$I_y=a^2\frac{i\mathbf{k}_t}{k_t^2}\cdot\left[-i\omega\varepsilon_0\varepsilon_h\frac{\partial\mathbf{E}_t}{\partial y}+\left(\frac{\omega^2}{c^2}\varepsilon_h-k_t^2\right)\left(\hat{\mathbf{y}}\times\mathbf{H}_t\right)\right] \tag{2.6}$$

where $\mathbf{k}_t$, $\mathbf{H}_t$ and $\mathbf{E}_t$ stand for the transverse components of the wave vector, magnetic and electric fields, respectively. Due to the geometry of the problem (see Fig. 3.1), the magnetic field has a single component, oriented along the *z*-direction, hence it is evident that $\mathbf{H}_t=\mathbf{H}=H_z\hat{\mathbf{z}}$, while $\mathbf{k}_t=k_x\hat{\mathbf{x}}$ and $\mathbf{E}_t=E_x\hat{\mathbf{x}}$. In the frequency domain the magnetic field satisfies the following second order differential equation in the $y\neq 0$ region:

$$\nabla^2 H_z+\omega^2\mu_0\varepsilon_0\varepsilon_h H_z=-\frac{\partial J_{y,wm}}{\partial x}+\frac{\partial J_{x,ext}}{\partial y}. \tag{2.7}$$

Since in the region $y\neq 0$ the external current vanishes, the magnetic field in the wire medium region must be a superposition of the so-called q-TEM and TM waves [30]. Therefore it is possible to write the electromagnetic field distribution as:

$$H_z\left(x,y,\omega\right)=\begin{cases}\left(T_1^{+}e^{-\gamma_{TEM}y}+T_2^{+}e^{-\gamma_{TM}y}\right)e^{ik_x x} & y>0\\ \left(T_1^{-}e^{\gamma_{TEM}y}+T_2^{-}e^{\gamma_{TM}y}\right)e^{ik_x x} & y<0\end{cases} \tag{2.8}$$

where $T_1^{\pm}$ and $T_2^{\pm}$ stand for the amplitudes of the q-TEM and TM modes under a plane wave excitation scenario with the incident wave characterized by the transverse wave

number k_x. The propagation constants of the TM (γ_{TM}) and q-TEM (γ_{TEM}) modes are given by [21, 30, 33, 34]:

$$\gamma_{\pm} = -i\left[k_h^2 - \frac{1}{2}\left(k_p^2 + k_x^2 - k_c^2 \pm \sqrt{\left(k_p^2 + k_x^2 - k_c^2\right)^2 + 4k_x^2 k_c^2}\right)\right]^{\frac{1}{2}} \tag{2.9}$$

where $\gamma_{TM} = \gamma_+$, $\gamma_{TEM} = \gamma_-$ and $k_c^2 = -\dfrac{k_p^2}{f_V}\dfrac{1}{\left(\varepsilon_m/\varepsilon_h\right)-1}$.

To determine the unknowns $T_1^{\pm}$ and $T_2^{\pm}$, a set of boundary conditions needs to be enforced on the general solution at $y = 0$. Due to the flow of charged particles, the magnetic field is discontinuous at the plane $y = 0$, where the charges are confined to. However, the tangential component of the electric field E_x remains continuous at this plane. Moreover, given the geometry of the system, since the flow of charges along the wires is perpendicular to the flow of external charges, it seems reasonable to assume that I_y, given by Eq. (2.6), is continuous at $y = 0$. The remaining boundary condition is obtained from the behavior of the electric charge in the nanowires in the vicinity of $y = 0$. It was shown in Ref. [31] that the density of charge in the nanowires per unit of length (p.u.l.) q may be written in terms of an average electrostatic potential drop measured from the nanowire to the boundary of the associated unit cell φ [31], such that $q = C\varphi$, where C is a capacitance (p.u.l.) that depends on the geometry of the wire medium. Similarly to the current in the nanowires, this additional potential φ may also be written directly in terms of the macroscopic fields [31, 32]. It can be shown that it satisfies:

$$\varphi = \frac{a^2}{i\omega C}\frac{\omega\varepsilon_0\varepsilon_h\mathbf{k}_t}{k_t^2}\cdot\left[\frac{\partial^2\mathbf{E}_t}{\partial y^2} + \left(\frac{\omega^2}{c^2}\varepsilon_h - k_t^2\right)\mathbf{E}_t\right]. \tag{2.10}$$

Since the tangential component of the electric field is expected to be continuous at $y=0$, it follows that the additional potential φ, and consequently q, must also have the same property. In summary, the set of boundary conditions necessary to find the unknowns $T_1^{\pm}$ and $T_2^{\pm}$ is the following:

$$\left\lfloor H_z \right\rfloor_{y=0} = -en_z e^{ik_x x}, \tag{2.11a}$$

$$\left\lfloor E_x \right\rfloor_{y=0} = 0, \tag{2.11b}$$

$$\left\lfloor I_y \right\rfloor_{y=0} = 0, \tag{2.11c}$$

$$\left\lfloor \varphi \right\rfloor_{y=0} = 0. \tag{2.11d}$$

Here, the operator $\left\lfloor \ \right\rfloor_{y=0}$ has the same definition as in Chapter II. Using the boundary conditions (2.11a)-(2.11d), together with Eqs. (2.6), (2.8), (2.10) and $E_x = -\dfrac{1}{i\omega\varepsilon_0\varepsilon_h}\dfrac{\partial H_z}{\partial y}$, allows us to write a system of equations that can be solved to find the unknowns. Interestingly $T_1^{\pm}$ and $T_2^{\pm}$ have an exact analytical solution [J1] that permits writing the spatial distribution of the magnetic field as:

$$H_z(x,y,\omega) = \frac{e\,n_z e^{ik_x x}}{2}\mathrm{sgn}(y)\left(\frac{\varepsilon_h\omega^2/c^2+\gamma_{TM}^2-k_x^2}{\gamma_{TEM}^2-\gamma_{TM}^2}e^{-\gamma_{TEM}|y|}-\frac{\varepsilon_h\omega^2/c^2+\gamma_{TEM}^2-k_x^2}{\gamma_{TEM}^2-\gamma_{TM}^2}e^{-\gamma_{TM}|y|}\right). \tag{2.12}$$

To characterize the radiation pattern of the moving charges, it is necessary to calculate the magnetic field in the time domain. The time-domain evolution is determined by calculating the inverse Fourier transform $H_z(x,y,t) = \dfrac{1}{2\pi}\int_{-\infty}^{+\infty} H_z(x,y,\omega)e^{-i\omega t}d\omega$. Provided the charges are moving for a long time (for instance since $t=-\infty$) and the source of charges is at a very distant point from a certain region of interest, it is expected that the time evolution of H_z is simply described by the translation $x_0 \to x_0 + vt_0$ along the x direction of the signal calculated

at $t=0$, being t_0 a generic instant of time. Hence, a snapshot of the magnetic field at $t=0$ is sufficient to characterize the Cherenkov emission at an arbitrary time instant.

III.2.2. Examples and Discussion

Next, the Cherenkov emission is numerically studied.

III.2.2.1 Radiation Patterns

In the first example, we consider an unbounded nanowire structure with PEC wires ($\varepsilon_m=-\infty$) standing in vacuum ($\varepsilon_h=1$). The wires have a radius $r=0.05a$, with $a=100\,\text{nm}$ being the lattice spacing, which is fixed hereafter in all examples of this subsection. Figure 3.2**(a)-(b)** shows the spatial distribution of the magnetic field intensity at $t=0$, so that the pencil of moving charges is at $x=0$, for two values of velocity, $v=0.2c$ and $v=0.5c$.

Quite interestingly, in both plots the magnetic field is non-zero for $x>0$. This is consistent with the fact that the electromagnetic radiation propagates faster in the vacuum host region (with velocity equal to *c*) than the charged particles do. Moreover, it can be checked that there is a nodal line wherein the magnetic field vanishes at the plane $y=0$. The snapshots of the magnetic field intensity also reveal another eye catching property, namely that the field inside the wire medium has maximal intensity along a specific direction θ, measured with respect to the *x*-negative axis as illustrated in Fig. 3.2**(c)**.

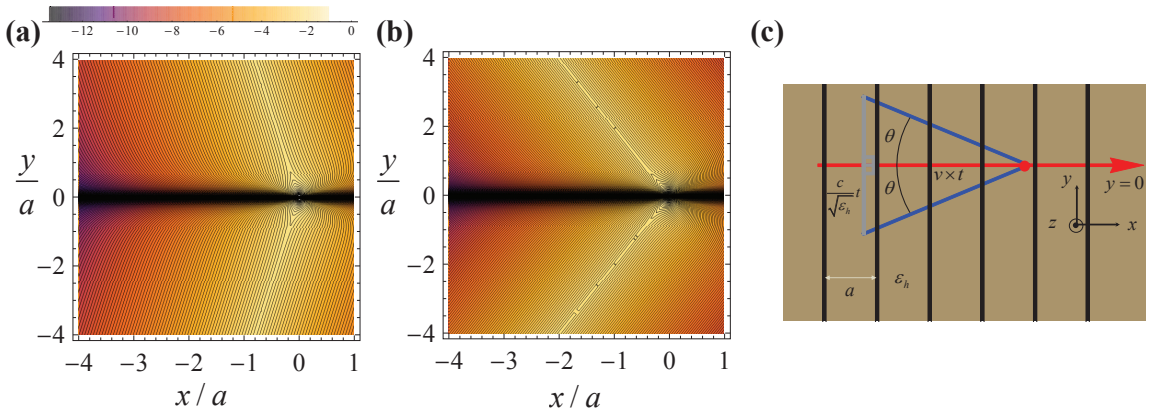

Fig. 3.2. Snapshot (at $t = 0$) of the magnetic field intensity (in arbitrary logarithmic units) radiated by a linear array of charges moving inside an unbounded wire medium with vacuum as the host and PEC nanowires with radius $r = 0.05a$. The velocity of the charges is: **(a)** $v = 0.2c$ **(b)** $v = 0.5c$. **(c)** Representation of the radiation emitted when a beam of moving charges propagates inside a wire medium along the *x*-direction. Because the main radiation channel is associated with the q-TEM mode of the wire medium, most of the emitted radiation is launched along the direction θ measured with respect to the direction –*x*.

As shown in Fig. 3.2**(a)-(b)**, for PEC wires the value of θ decreases with increasing velocity, and it can be verified with an excellent accuracy that $\theta = \pm\arctan\left(c/\left(v\sqrt{\varepsilon_h}\right)\right)$. This can be understood by noting that as the moving charges pass above a certain row of wires, they will induce currents in these wires, which will mainly excite the q-TEM mode in the wire medium. In the PEC limit, this mode propagates with velocity $c/\sqrt{\varepsilon_h}$ along the direction of the wires [29, 30]. As the radiated field propagates in the wire medium with a velocity $c/\sqrt{\varepsilon_h}$ along the $\pm y$ direction, and the charges move with velocity v in the *x*-direction, it follows that the maximal intensity of the field is along a specific direction $\theta = \pm\arctan\left(c/\left(v\sqrt{\varepsilon_h}\right)\right)$, as shown in Fig. 3.2**(c)**. This property is also easily explained within the proposed analytical model. Since the PEC nanowires are embedded in a non-dispersive dielectric host, the inverse Fourier transform of the TEM mode contribution to the total radiated field (first addend in Eq. (2.12)) can be analytically calculated, and it is given by:

$$H_z^{TEM}(x,y,t) = -k_p v \frac{e\, n_z}{4} \operatorname{sgn}(y) e^{-k_p v \left| t - \frac{x}{v} - \sqrt{\varepsilon_h}\frac{|y|}{c} \right|}. \tag{2.13}$$

Clearly, the intensity of the TEM contribution to the magnetic field is maximal along the lines $vt - x = \sqrt{\varepsilon_h} v \dfrac{|y|}{c}$, which have a slope $\theta = \pm \arctan\left(c / \left(v\sqrt{\varepsilon_h}\right)\right)$, consistent with Fig. 3.2**(c)**.

In order to study the influence of the nanowire structure in the emitted radiation, it is useful to compare the field diagrams of Fig. 3.2, with what would be obtained in the absence of the wire medium. In that case, the self-field of the moving particles reduces to [J1]:

$$H_{z,self}(x,y,t) = -\frac{n_z e v}{2\pi} y \frac{\sqrt{1 - v^2/c^2}}{(x - tv)^2 + \left(1 - v^2/c^2\right) y^2} \ . \tag{2.14}$$

Importantly, even though the magnetic field is discontinuous in the frequency domain, it is – with the exception of the singular point corresponding to the instantaneous position of the array of charges – continuous in the time domain. The expression of the self-field also confirms that the magnetic field at a generic instant of time differs only from the magnetic field at an earlier instant by a translation along the x-direction of the distance $x_0 = vt_0$.

It is interesting to note that Eq. (2.14) could have also been obtained simply by applying a Lorentz transformation to the electromagnetic fields [35, pp. 558], considering that in the co-moving frame (where the charges are at rest) the self-field is such that $\mathbf{H}'(x',y',t') = 0$ and $\mathbf{E}'(x',y',t') = \dfrac{-en_z}{2\pi\varepsilon_0} \dfrac{1}{x'^2 + y'^2} \left(x'\hat{\mathbf{x}}' + y'\hat{\mathbf{y}}'\right)$. A time snapshot at $t = 0$ of the magnetic field intensity associated with a pencil of charges moving at a constant velocity $v = 0.5c$ in a vacuum is depicted in Fig. 3.3.

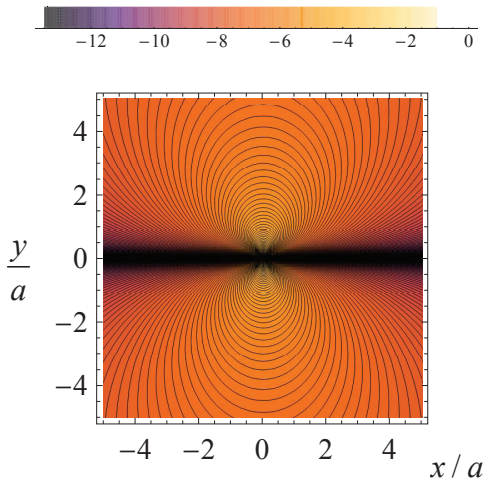

Fig. 3.3. Snapshot (at $t = 0$) of the magnetic field intensity (in arbitrary logarithmic units) for a linear array of charges moving in a vacuum with velocity $v = 0.5c$. The trajectory of the moving charges is confined to the plane $y = 0$.

Comparing the results of Fig. 3.3 and Fig. 3.2, particularly with Fig. 3.2**(b)** where the velocity of the charges is the same, it is seen that the presence of the wire medium significantly perturbs the near field. The most significant difference between both cases is that the magnetic field no longer has a maximal intensity along a specific direction θ. Since in the example of Fig. 3.3 the charges propagate in a vacuum, the Cherenkov velocity threshold is not satisfied, and in contrast to what is observed in the nanowire structure there is no Cherenkov radiation.

In the wire medium, the main radiation channel is associated with the q-TEM mode. When the nanowires are made of a PEC material ($\varepsilon_m = -\infty$) the dispersion relation of this mode is simply $|k_y| = k_h$. Therefore, the dispersion of the TEM mode is independent of k_x, and hence also independent of the velocity of the charges $v = \omega/k_x$. An immediate consequence of this type of dispersion is that it may always be possible to couple the moving charges to a propagating mode, ensuring the conservation of the momentum, no matter how small the velocity is. This indicates that in the nanowire structure there is no Cherenkov threshold.

This is a well-known property of periodic gratings [36-38]. As a consequence of the periodicity of such structures, they are able to generate waves with spatial wavelengths different from those imposed by the velocity of the moving particles. Specifically, because of the umklapp processes [38], the wave number k_x (determined by the charges velocity *v*) is equivalent to $k_x + 2\pi n / a$, with *n* being an integer and *a* the period of the grating. Hence, even for very small velocities, where $k_x = \omega / v$ may be very large as compared to $k_0 = \omega / c$, the periodic structure can generate waves with $k_x' << k_x$ (associated with a negative *n* and a proper tuning of the period *a*), which may permit us to have a better electron-photon momentum match, i.e. match k_x' with k_0, and allow for the emission of radiation.

It is important to stress that within the analytical model described in Sec. III.2.1 the wire medium is regarded as a continuous medium. Since there is no intrinsic periodicity, the aforementioned explanation for Cherenkov radiation with no velocity threshold does not directly apply. However, due to the explicit dependence on the frequency of the effective dielectric function given by Eq. (2.1), the effective medium model introduces another crucial characteristic: time dispersion. Consequently, the phase velocity of the electromagnetic waves supported by the effective medium is frequency dependent, and hence the Cherenkov condition may be satisfied in the effective medium, consistent with the property enunciated above for the q-TEM waves. In fact, the dispersive response of the effective medium retains the ability of the wire medium to tailor the characteristic spatial wavelength of electromagnetic radiation, but instead of taking into account all the generated spatial harmonics as in the microscopic theory, it provides an effective medium response based on a few spatial harmonics. It should be noted that the effective medium theory is valid provided the characteristic wavelength of interaction of the moving charges with the periodic structure is significantly larger than the lattice

period. As the effective medium response is defined over scales considerably larger than the period of the structure, the medium is not able to distinguish the harmonics with various $k_x + 2\pi n / a$, and all these harmonics contribute to the same principal mode of propagation in the medium.

Since the proposed analytical model relies on the effective medium theory, the validity of the calculated radiation patterns requires some discussion. Our effective medium theory models the response of the wire medium in terms of only a few eigenmodes: the TE, TM, and q-TEM waves, each characterized by its own dispersion [30, 33]. For this model to be physically valid, we must ensure that only these principal modes may propagate in the medium for a given excitation. As detailed in [J1], the model is valid provided most of the spectral content of the fields radiated by the pencil of moving charges is within the frequency range $\omega < \omega_{\max} = \pi v / a$.

For a fixed lattice period, the previous condition is comfortably fulfilled up to velocities on the order of $0.84c$, which introduces an upper bound for the velocity of the charges. To investigate the validity of the effective medium model in presence of loss and dispersion in the wires, it was assumed that the nanowires are made of silver, whose permittivity is characterized using the Drude dispersion model $\varepsilon_m(\omega) = 1 - \omega_p^2 / \omega(\omega + i\Gamma)$, with parameters $\omega_p / 2\pi = 2175\,[\mathrm{THz}]$ and $\Gamma / 2\pi = 4.35\,[\mathrm{THz}]$, consistent with the experimental data reported in the literature [39]. Interestingly, when the effects of loss and dispersion in the metal are taken into account, the spectrum of the field is narrowed (due to the absorption effects at high frequencies) and the model becomes valid over a broader range of velocities. Using the same criteria as in the PEC case, it was checked in [J1] that the model may be valid up to velocities on the order of $0.97c$.

Similar to Fig. 3.2, in Fig. 3.4 we show the spatial distribution of the magnetic field intensity inside a silver nanowires array, for charges moving at two distinct velocities, $v = 0.2c$ and $v = 0.5c$, but over a much more extended region of space. Although the field pattern is less defined than in the previous case, the main beam remains directed along the direction $\theta \sim \arctan\left(c/\left(v\sqrt{\varepsilon_h}\right)\right)$, but it is now less directive than in Fig. 3.2. Moreover, the value of θ is now slightly smaller than predicted by the formula, so that for charges moving at a velocity $v = 0.5c$, the maximum of the magnetic field intensity is directed along $\theta_{Ag} \approx \pm 59^{\circ}$, while the theoretical formula gives $\arctan\left(c/\left(v\sqrt{\varepsilon_h}\right)\right) = \pm 63^{\circ}$, and for $v = 0.2c$ the theoretical slope is $\arctan\left(c/\left(v\sqrt{\varepsilon_h}\right)\right) = \pm 78.7^{\circ}$ whereas in the calculated field pattern for the silver nanowires, the maximum is directed along $\theta_{Ag} \approx \pm 72.5^{\circ}$.

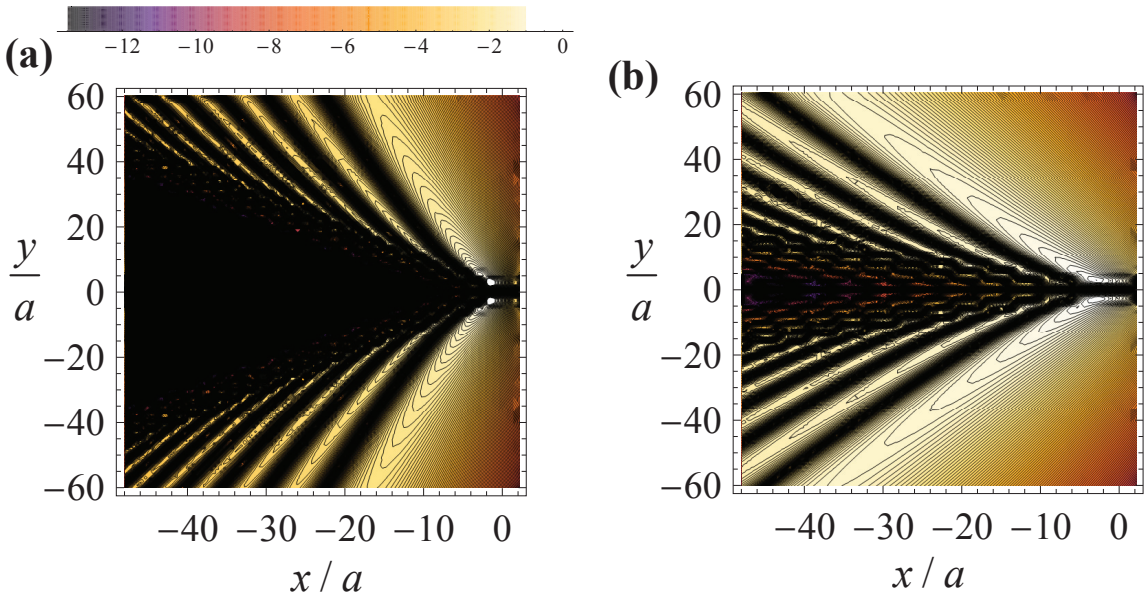

Fig. 3.4. Snapshot (at $t = 0$) of the magnetic field intensity (in arbitrary logarithmic units) radiated by a linear array of charges moving inside an unbounded wire medium with vacuum as the host medium and silver nanowires with radius $R = 0.05a$. The velocity of the charges is: **(a)** $v = 0.2c$, **(b)** $v = 0.5c$.

An interference pattern can also been observed in the results depicted in Fig. 3.4. The differences between the results of PEC nanowires and silver nanowires are caused by

the distinct velocities of the q-TEM mode in both scenarios. This can be easily understood from Eq. (2.9) by noting that the frequency dispersion in the metal causes the velocity of the q-TEM mode to depend on k_x. Consequently, different spectral components of the field travel along the *y*-direction with different velocities, and the beam becomes more diffuse as compared to the PEC case.

III.2.2.2 Secondary Radiative Channel

Having established that the main radiative decay channel is associated with the q-TEM mode, even in the presence of losses and dispersion in the nanowires, it is important to mention that the TM mode can also contribute to the Cherenkov emission. In the case of PEC nanowires, this requires the dispersion equation $\frac{\omega^2}{c^2}\varepsilon_h = k_p^2 + k_x^2 + k_y^2$ to generate a k_y real valued. Using $k_x = \omega/v$ in the previous equation it is found that:

$$k_y^2 = \frac{\omega^2}{c^2}\left(\varepsilon_h - \frac{c^2}{v^2}\right) - k_p^2 . \tag{2.15}$$

Hence the condition $(\omega/c)^2\left(\varepsilon_h - (c/v)^2\right) > k_p^2$ must be satisfied for the TM mode to contribute to the Cherenkov emission. Quite importantly, if the dispersion of the host material is neglected, it is seen that the charge velocity is required to be greater than the light velocity in the host material, i.e. $v > c/\sqrt{\varepsilon_h}$, which corresponds to the usual charge velocity threshold in the host medium. This is a sufficient condition to produce a k_y real valued, because if it is fulfilled the term $(\omega/c)^2\left(\varepsilon_h - (c/v)^2\right)$ can be made larger than k_p^2 for sufficiently large frequencies.

To illustrate how the TM mode may provide a secondary radiative decay channel for the moving particles, competing with that associated with the q-TEM mode, we

consider a scenario wherein the charges travel with a constant velocity $v = 0.7c$ in a PEC nanowire array. The wires are embedded in a host material whose dielectric constant follows the Debye dispersion model $\varepsilon_d(\omega) = \varepsilon_\infty + \dfrac{\varepsilon(0) - \varepsilon_\infty}{1 - i\omega\tau}$ with parameters $\varepsilon(0) = 11$, $\tau = 30[\text{as}]$ and $\varepsilon_\infty = 1$. The value of $\varepsilon_\infty = \lim_{\omega\to\infty} \varepsilon_d(\omega)$ was chosen to be unity so that the spectrum of emission of the host material had a high-frequency cutoff [5]. This property is consistent with the fact that the dielectric response of realistic media ceases for sufficiently large frequencies. It can be checked that k_y becomes dominantly real-valued at the normalized frequency $\omega a/c = 0.645$, which corresponds to $\omega a/c = \sqrt{k_p^2 \Big/ \left(\varepsilon(0) - (c/v)^2\right)}$. Figure 3.5**(a)** shows the time snapshot at $t = 0$ of the magnetic field intensity for the considered geometry.

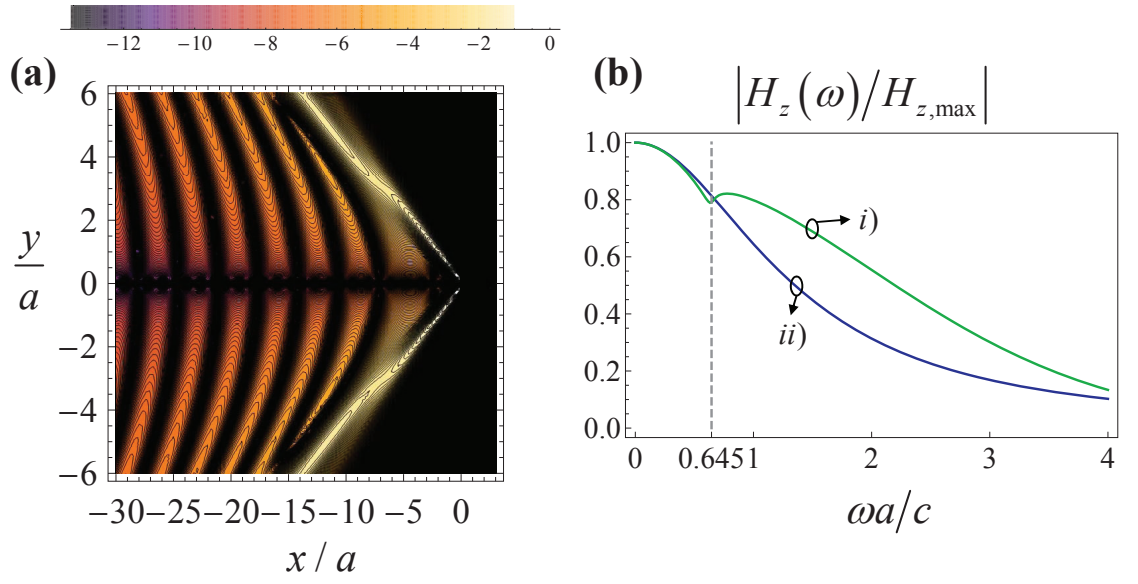

Fig. 3.5. (a) Snapshot (at $t = 0$) of the magnetic field intensity (in arbitrary logarithmic units) radiated by a linear array of charges moving inside an unbounded wire medium at a velocity $v = 0.7c$ inside an unbounded wire medium formed by PEC nanowires with wire radius $r = 0.05a$, for a host medium permittivity described by a Debye model with parameters, $\tau = 30[\text{as}]$, $\varepsilon_\infty = 1$ and $\varepsilon(0) = 11$. **(b)** Representation of the normalized spectrum of the magnetic field $H_z(x, y, \omega)$ produced by the moving charges ($v = 0.7c$) at the point $(x, y) = (-3a, -3a\tan\theta)$, along the direction wherein the contribution of the TEM mode is maximal, for a wire medium such that the host is: *i)* (green curve) the dielectric material considered in (a) and *ii)* (blue curve) vacuum.

The most striking difference between Fig. 3.5**(a)** and the results depicted in Fig. 3.2**(a)-(b)**, where the TM mode is not excited, is that there is an interference pattern inside the wire medium (particularly for $x<0$). The interference pattern is caused by different propagation characteristics of the waves associated with the q-TEM and TM modes. Moreover, there is not a well-defined direction along which the magnetic field has a maximal intensity, but instead the field pattern is more diffuse and the region of maximum intensity appears to be adjacent to a nodal line. On the other hand, it is observed that the magnetic field completely vanishes in the region $x>0$ at $t=0$ (assuming that the position of the charges at $t=0$ is $x=0$). Indeed, as the dielectric constant of the host material may be greater than unity, the emitted photons can travel at a smaller velocity than the charges provided $v>c/\sqrt{\varepsilon_d}$, i.e. when the velocity threshold for Cherenkov emission in the host material is satisfied.

In order to confirm that due to the excitation of the TM mode new spectral components may be present in the radiation field, figure 3.5**(b)** depicts the spectrum of the magnetic field calculated at the point $(x,y)=(-3a,-3a\tan\theta)$ inside the wire medium, along the direction θ of maximal radiation of the TEM mode, for the same host material considered in Fig. 3.5**(a)** (green curve) and for a vacuum as host material (blue curve). The results of Fig. 3.5**(b)** reveal that when the dielectric constant of the host material is characterized by the Debye model, the radiated field intensity is enhanced at the normalized frequency $\omega a/c=0.645$ as compared to the vacuum case. As aforementioned, at the normalized frequency $\omega a/c=0.645$ the dispersion equation of the TM mode generates a k_y with a real component, and the TM mode starts contributing to the spectrum of the radiated field. Hence, for larger frequencies the total field has new spectral components, resulting in an enhancement of the magnitude.

III.2.3. Stopping Power

When a charged particle emits radiation it loses energy in the process. However, so far it was assumed that all charges move with a constant velocity v. In fact, the velocity may only remain constant at the expense of an externally applied force. The amount of energy extracted from the particles can be calculated through the stopping power, defined as the average energy loss of the particles per unit of path length.

There are two main contributions to the stopping power: the losses associated with the absorption in the medium (also called "ionization losses" by some authors, see Ref. [5], chapter XIV) and the radiation losses, associated with the emitted Cherenkov radiation [5]. In natural materials, particularly in solid materials, there is also another contribution to the stopping power, associated with radiation emitted by accelerated charges when colliding with surrounding atoms, the bremsstrahlung [5]. As the Cherenkov radiation appears when the charges move with a constant velocity, the bremsstrahlung is a completely unrelated effect, and hence it will not be discussed in this thesis. Although for natural materials the Cherenkov radiation losses are usually calculated using the Frank-Tamm formula [2, 41], next we develop a formalism to calculate the total energy loss rate that is valid for both natural and structured media.

It is well known [5] that the total instantaneous power extracted from the charges moving at a constant velocity is given by $P_0 = -\int \mathbf{E}_{loc} \cdot \mathbf{J}\ d^3r$, where $\mathbf{E}_{loc}$ represents the local electric field that acts on the charges. As the charges are not accelerated, the self-field does not contribute to the stopping power [5]. Using the expression of the current density of moving charges given by Eq. (2.2), it follows that $P_0 = evE_{loc,x}\left(vt,0,t\right)n_z L_z$, where $E_{loc,x}$ is the x component of the local electric field (scattered by the wire

medium) and L_z represents the width of the current pencil along the z direction, so that $N_z = n_z L_z$ is the total number of moving charges.

From the analytical model framework proposed in Sec. III.2.1, the *x*-component of the electric field may be easily obtained in the frequency domain using $E_x(x,y,\omega) = -\frac{1}{i\omega\varepsilon_0\varepsilon_h}\frac{\partial H_z(x,y,\omega)}{\partial y}$, where H_z is given by Eq. (2.12), and it reads:

$$E_x(x,y,\omega) = -\frac{e\,n_z e^{ik_x x}}{2i\omega\varepsilon_0\varepsilon_h}\left(-\gamma_{TEM}\frac{\varepsilon_h\omega^2/c^2+\gamma_{TM}^2-k_x^2}{\gamma_{TEM}^2-\gamma_{TM}^2}e^{-\gamma_{TEM}|y|}+\gamma_{TM}\frac{\varepsilon_h\omega^2/c^2+\gamma_{TEM}^2-k_x^2}{\gamma_{TEM}^2-\gamma_{TM}^2}e^{-\gamma_{TM}|y|}\right). \quad (2.16)$$

Within this approach it is not a simple matter to separate the local electric field from the self-field. As previously mentioned, the self-field does not contribute to the stopping power [5], and hence the total energy loss rate of the moving charges may also be calculated using:

$$\frac{P_0}{N_z} = evE_x(vt,0,t). \quad (2.17)$$

Substituting $x = vt$ and $y = 0$ in Eq. (2.16) and calculating the inverse Fourier transform of the corresponding formula, one obtains the total instantaneous power extracted from the charges in the form of the integral:

$$\frac{P_0}{N_z} = \frac{ev}{2\pi}\int_{-\infty}^{+\infty} E_x(vt,0,\omega)e^{-i\omega t}d\omega. \quad (2.18)$$

The above expression can be trivially generalized to a scenario wherein the charges move with constant velocity inside an unbounded dielectric medium with permittivity ε_d. For that case, the *x*-component of electric field in the frequency domain reads:

$$E_x(x,y,\omega) = -\frac{1}{i\omega\varepsilon_0\varepsilon_d}\frac{\partial H_z}{\partial y} = -\frac{n_z e}{2}\frac{\gamma_d}{i\omega\varepsilon_0\varepsilon_d}e^{-\gamma_d|y|}e^{ik_x x}. \quad (2.19)$$

To assess the influence of the wire medium on the amount of emitted Cherenkov radiation, we consider a nanowire metamaterial with a lattice period $a = 100\,\text{nm}$ formed

by nanowires with radius $R = 0.05a$ standing in a vacuum ($\varepsilon_h = 1$). The stopping power of the nanowire array (P_{WM}) is compared with that characteristic of a natural unbounded dielectric (P_d). The dielectric material used in the calculations was water, as this material is widely used in the context of Cherenkov radiation detectors [27-28]. The dielectric constant of the water was characterized using the Debye dispersion model $\varepsilon_d(\omega) = \varepsilon_\infty + \frac{\varepsilon(0) - \varepsilon_\infty}{1 - i\omega\tau}$ with parameters $\tau = 9.36[\text{ps}]$, $\varepsilon(0) = 80.21$ and $\varepsilon_\infty = 5.6$ at $20^\text{o}\,\text{C}$, chosen accordingly to the experimental data reported in Ref. [40].

The computed ratio of the stopping powers is depicted in the red curve of Fig. 3.6, and confirms that the nanowires typically boost the stopping power. Particularly, for velocities close to $v/c \approx 0.35$, the stopping power of the wire medium can be more than 200 times larger than in water. This demonstrates that the wire medium can dramatically enhance the level of emitted Cherenkov radiation. Obviously, as the velocity of the particles increases the Cherenkov velocity threshold for the chosen dielectric is satisfied over a broader frequency spectrum [41], and therefore more radiation is emitted and absorbed. This causes an increase of the stopping power of the dielectric material, which in turn leads to a decrease in the ratio P_{WM}/P_d. The velocity range considered in the calculations takes into account that the permittivity of water does not approach unity as the frequency tends to infinity [5], i.e. $\varepsilon_\infty \neq 1$. As discussed in Sec. III.2.2.2 if the value of $\varepsilon_\infty = \lim_{\omega\to\infty} \varepsilon_d(\omega)$ is larger than unity, the spectrum of emission of the host material does not have a high-frequency cutoff [5]. If such a cutoff is not considered, the stopping power is infinite. Due to this reason the stopping power analysis is restricted to velocities smaller than $v_{\max} < c/\sqrt{\varepsilon_\infty} = 0.42c$.

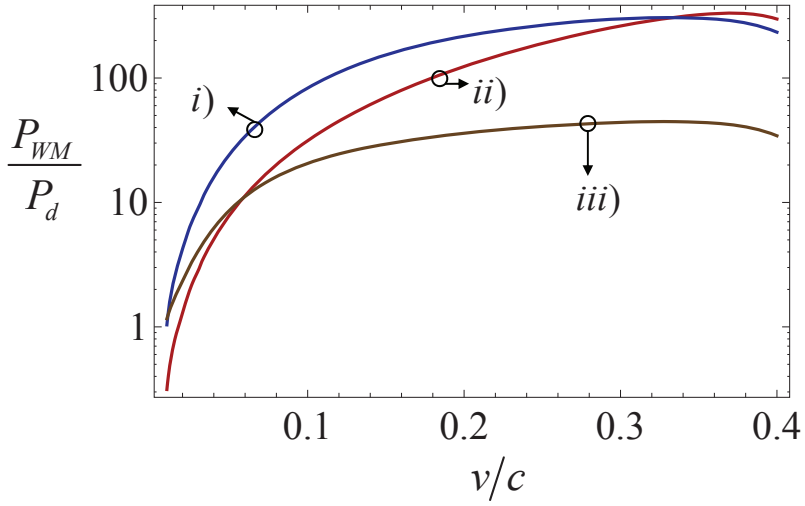

Fig. 3.6. Ratio between the stopping powers of the nanowire structure and water as a function of the charges velocity for: i) the host medium is a vacuum and the nanowires are made of silver. ii) the host medium is a vacuum and the nanowires are PEC. iii) the host medium is water and the nanowires are made of silver.

It is interesting to study the influence of the effects of dispersion and loss in the metallic nanowires on the amount of extracted radiation. In order to do so, the PEC wires are replaced by silver nanowires and the value of the stopping power is re-calculated for this structure (blue curve in Fig. 3.6). Despite the response of silver nanowires is qualitatively similar to that of PEC wires, the former typically extract more power from the moving charges than the PEC wires, likely because of the enhanced absorption loss by the metal. It is relevant to stress that when the wires are made of a PEC material, all the energy extracted from the charges is associated with emitted Cherenkov radiation, because in such case there is no absorption.

The Cherenkov emission was also studied in the nanowire structure when the host material is water (brown curve in Fig. 3.6). Also in this scenario there is a significant enhancement (~ 45) of the emitted Cherenkov radiation, even though not so dramatic as in the cases discussed before.

III.2.4. Density of States

It was discussed in Sec. III.1 that an array of nanowires in the long wavelength limit is characterized by an extremely large density of photonic states. This may allow for the enhancement of the Purcell emission rate [22-26] and also to boost the Casimir interaction between two bodies [18-20]. From Fig. 3.6, it is clear that the stopping power of the wire medium can surpass by two orders of magnitude the stopping power of natural media. Thus, it is natural to ask what is the influence of the large density of photonic states in the amount of emitted radiation. In this section we study the effect of varying the density of the wires (number of wires per unit of cross sectional area) on the value of the stopping power, and its relation with the density of electromagnetic states.

In Refs. [18, 19, 22] it was shown that the density of electromagnetic states in the wire medium is nearly independent of the frequency and non-zero in the low frequency limit. This is due to the contribution of the q-TEM mode to the radiated field which, as discussed in section III.2.2, is the main radiative decay channel. Without any loss of generality, the following discussion is focused on the density of states associated with the TEM mode for a wire medium composed of PEC wires embedded in a vacuum.

The density of photonic states in the wire medium may be obtained by considering a material volume $V = L_x \times L_y \times L_z$ within wire medium bounded by PEC walls. Since each wire can be set to a unique electrostatic potential, the total number of independent oscillators (standing waves) at a given frequency associated with TEM modes in the cavity is exactly equal to the number of nanowires $N = L_x L_z / a^2$. From the dispersion relation of the TEM waves it follows that in the frequency axis these modes are spaced by $\Delta\omega = \pi c / L_y$, therefore, the density of electromagnetic states is $D_{TEM}(\omega) = N/(V\Delta\omega) = 1/(\pi a^2 c)$, which is independent of the frequency. Therefore,

even at low frequencies, the number of electromagnetic states per unit of frequency is always non-zero and is roughly proportional to the density of wires ($1/a^2$).

The density of states may also be calculated from the phase space volume between the neighboring isofrequency surfaces in the wave vector space [19]. For the TEM mode it is given by:

$$D_{TEM}(\omega) = \frac{1}{(2\pi)^3}\int \delta(\omega - \omega_{\mathbf{k}})d^3\mathbf{k} \tag{2.20}$$

where $\omega_{\mathbf{k}}$ is obtained from the frequency dispersion of the TEM mode $\omega/c = |k_y|$, for PEC nanowires. The transverse wave vector associated with TEM waves must be restricted to the first Brillouin zone [18], as shown in Fig. 3.7**(a)**. It can be easily checked that Eq. (2.18) gives the same result as obtained before.

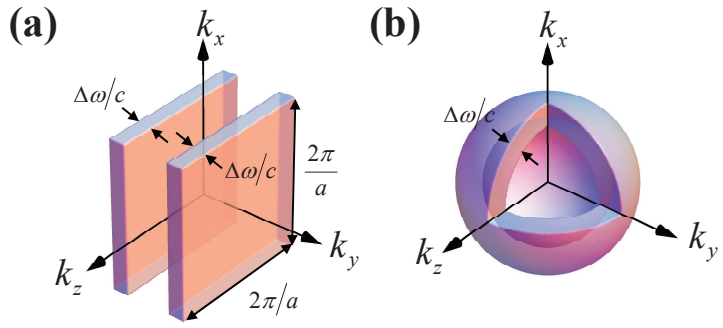

Fig. 3.7. Isofrequency surfaces for **(a)** the wire-medium and **(b)** conventional dielectric material. The density of states can be calculated through the phase space volume between the neighboring isofrequency surfaces.

On the other hand, in a vacuum the dispersion of the photonic states is given by $(\omega/c)^2 = |\mathbf{k}|^2$, where $\mathbf{k} = k_x\hat{\mathbf{x}} + k_y\hat{\mathbf{y}} + k_z\hat{\mathbf{z}}$, and the isofrequency surfaces are spheres with radius ω/c, as shown in Fig. 3.7**(b)**. Similarly to the wire medium, the density of states for a vacuum can be calculated from the phase space volume between the neighboring isofrequency surfaces. From the isofrequency surfaces shown in Fig. 3.7**(b)**, it can be

easily checked that $N/(V\Delta\omega) = \omega^2/(2\pi^2 c^3)$ [19]. Importantly, the density of states scales with ω^2, and thus vanishes in the zero-frequency limit. This contrasts with the wire medium, where the number of photonic states is roughly proportional to the number of wires and independent of the frequency, thus much larger than in free space in the long wavelength limit.

Because the density of states in the wire medium is proportional to $1/a^2$, one may expect that an increase in the density of wires ($1/a$ increases) will result in an increase in the number of available radiative channels, therefore causing the enhancement of the Cherenkov emission. To investigate this, the total energy loss rate was calculated for different values of the lattice spacing [Fig. 3.8]. In all the examples, the PEC nanowires have a radius $R = 0.05a$ and stand in a vacuum. It is important to stress that the effective medium model may yield less accurate results for large values of *a,* as discussed in [J1]. To circumvent this, the energy loss rate was calculated using Eq. (2.18) by truncating the integration range to the frequency spectrum where the effective medium model is valid, i.e. to $\omega < \omega_{\max} = \pi v/a$.

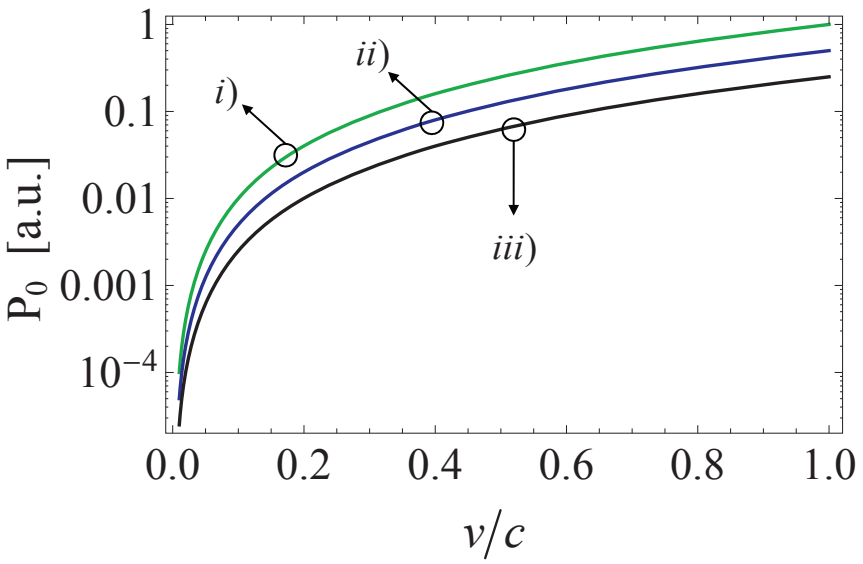

Fig. 3.8. Total energy loss rate (in arbitrary units) of an unbounded wire medium with $\varepsilon_h = 1$ and PEC nanowires as a function of the velocity of the charges, for different values of the lattice spacing: a) 100 nm , b) 200 nm , c) 425 nm .

As is seen in Fig. 3.8, as the lattice period decreases (the number of wires per unit area increases) the value of the energy loss rate, and thus the stopping power, increases. This happens because the density of states increases with the density of wires, and, as discussed before, a larger number of photonic states results in a larger number of decay channels available for radiation. This will evidently boost the amount of extracted Cherenkov radiation and therefore enhance the value of the stopping power.

III.3. Summary

Based on an effective medium framework, in this chapter we proposed an analytical model to characterize the Cherenkov emission by charged particles travelling within a nanowire metamaterial. This model was used in Sec. III.2.2 to calculate the radiation patterns associated the Cherenkov emission, and it was shown that the magnetic field has a maximum along a very specific direction, which depends on the velocity of the charges and on the dielectric constant of the host medium, even when loss and dispersion in the metal are taken into account. In addition, it was shown that the q-TEM

mode is the main radiative decay channel in the structure and that contrary to natural materials, the Cherenkov emission in such structures has no velocity threshold.

In Sec. III.2.3 the stopping power due to the emission of Cherenkov radiation was calculated for both the wire medium and natural media. It was shown that the amount of energy extracted from the particles in the nanowire metamaterial may be more than two orders of magnitude larger than in natural media, even in the limit where the nanowires are perfectly conducting, where there is no absorption of electromagnetic energy by matter. Importantly, it was revealed that contrary to natural media, the density of states of the wire medium in the long wavelength regime is independent of the frequency and that increasing the density of wires will result in an enhancement of the Cherenkov emission.

References

[1] P. A. Čerenkov, "Visible radiation produced by electrons moving in a medium with velocities exceeding that of light", *Phys. Rev.* **52**, 378, 1934.

[2] I. M. Frank, and I. E. Tamm, "Coherent visible radiation of fast electrons passing through matter", *Dokl. Akad. Nauk SSSR* **14**, 109, 1937.

[3] Yu. K. Akimov, "Cherenkov detectors in particle physics", *Physics of Atomic Nuclei* **67**, 1385, 2011.

[4] V. G. Veselago, "The electrodynamics of substances with simultaneously negative values of ε and μ", *Sov. Phys. Usp.* **10**, 509, 1968.

[5] L. D. Landau, E. M. Lifshitz, and L. P. Pitaevskii, *Electrodynamics of Continuous Media*, Elsevier Butterworth-Heinemann, Oxford, 2nd ed., 2004.

[6] J. Lu, T. M. Grzegorczyk, Y. Zhang, J. P. Jr, B.-I. Wu, and J. A. Kong, "Čerenkov radiation in materials with negative permittivity and permeability", *Opt. Express* **11**, 723, 2003.

[7] S. Xi, H. Chen, T. Jiang, L. Ran, J. Huangfu, B.-I. Wu, J. A. Kong, and M. Chen, "Experimental Verification of Reversed Cherenkov Radiation in Left-Handed Metamaterial", *Phys. Rev. Lett.* **103**, 194801, 2009.

[8] C. Luo, M. Ibanescu, S. G. Johnson, and J. D. Joannopoulos, "Cerenkov Radiation in Photonic Crystals", *Science* **299**, 368, 2003.

[9] V. S. Zuev, and G. Ya. Zueva, "Vavilov–Cherenkov Like Effect in Metal Nanofilms", *Opt. Spectrosc.* **108**, 640 (2010).

[10] S. N. Galyamin, T. A. V. Tyukhtin, A. Kanareykin, and P. Schoessow, "Reversed Cherenkov-Transition Radiation by a Charge Crossing a Left-Handed Medium Boundary", *Phys. Rev. Lett.* **103**, 194802, 2009.

[11] J. Zhou, Z. Duan, Y. Zhang, M. Hu, W. Liu, P. Zhang, and S. Liu, "Numerical investigation of Cherenkov radiations emitted by an electron beam bunch in isotropic double-negative metamaterials", *Nucl. Instr. and Meth. Phys. Res Sec. A* **654**, 475, 2011.

[12] V. S. Zuev, and G. Ya. Zueva, "Particular features of a Vavilov-Cherenkov-like phenomenon with emission of surface plasmons", *Opt. Spectrosc.* **112**, 159, 2012.

[13] J.-K. So, J.-H. Won, M. A. Sattorov, S.-H. Bak, K.-H. Jang, G.-S. Park, D. S. Kim, and F. J. Garcia-Vidal, "Cerenkov radiation in metallic metamaterials", *Appl. Phys. Lett.* **97**, 151107, 2010.

[14] Viktor V. Vorobev, and Andrey V. Tyukhtin, "Nondivergent Cherenkov Radiation in a Wire Metamaterial", *Phys. Rev. Lett.* **108**, 184801, 2012.

[15] A. Tyukhtin, and V. Vorobev, "Cherenkov radiation in a metamaterial comprised of coated wires", *J. Opt. Soc. Am. B* **30**, 1524, 2013.

[16] V. Ginis, J. Danckaert, I. Veretennicoff, and P. Tassin, "Controlling Cherenkov Radiation with Transformation-Optical Metamaterials", *Phys. Rev. Lett.* **113**, 167402, 2014.

[17] S. N. Galyamin, and A. V. Tyukhtin, "Dielectric Concentrator for Cherenkov Radiation", *Phys. Rev. Lett.* **113**, 064802, 2014.

[18] S. I. Maslovski, and M. G. Silveirinha, "Ultralong-range Casimir-Lifshitz forces mediated by nanowire materials", *Phys. Rev. A* **82**, 022511, 2010.

[19] S. I. Maslovski, and M. G. Silveirinha, "Mimicking Boyer's Casimir repulsion with a nanowire material", *Phys. Rev. A* **83**, 022508, 2011.

[20] T. A. Morgado, S. I. Maslovski, M. G. Silveirinha, "Ultrahigh Casimir Interaction Torque in Nanowire Systems", *Opt. Express* **21**, 14943, 2013.

[21] M. G. Silveirinha, P. A. Belov, and C. R. Simovski, "Ultimate limit of resolution of subwavelength imaging devices formed by metallic rods", *Opt. Lett.* **33**, 1726, 2008.

[22] Z. Jacob, I. Smolyaninov, and E. Narimanov, "Broadband Purcell effect: Radiative decay engineering with metamaterials", arXiv:0910.3981v2, 2009.

[23] Z. Jacob, J.-Y. Kim, G. Naik, A. Boltasseva, E. Narimanov, and V. Shalaev, "Engineering photonic density of states using metamaterials", *Appl. Phys. B: Lasers Opt.* **100**, 215, 2010.

[24] M. A. Noginov, H. Li, Y. A. Barnakov, D. Dryden, G. Nataraj, G. Zhu, C. E. Bonner, M. Mayy, Z. Jacob, and E. E. Narimanov, "Controlling spontaneous emission with metamaterials", *Opt. Lett.* **35**, 1863, 2010.

[25] A. N. Poddubny, P. A. Belov, and Y. S. Kivshar, "Spontaneous radiation of a finite-size dipole emitter in hyperbolic media", *Phys. Rev. A* **84**, 023807, 2011.

[26] I. Iorsh, A. N. Poddubny, A. Orlov, P. A. Belov, and Y. S. Kivshar, "Spontaneous emission enhancement in metal–dielectric metamaterials", *Phys. Lett. A* **376**, 185, 2012.

[27] G. B. Yodh, "Water Cherenkov detectors:MILAGRO", *Space Sci. Rev.* **75**, 199, 1996.

[28] K. Nakamura, "Hyper-Kamiokande - A Next Generation Water Cherenkov Detector", *Int. J. of Mod. Phys. A* **18**, 4053, 2003.

[29] P. A. Belov, R. Marques, S. I. Maslovski, I. S. Nefedov, M. Silveirinha, C. Simovski, and S. A. Tretyakov, "Strong spatial dispersion in wire media in the very large wavelength limit", *Phys. Rev. B* **67**, 113103, 2003.

[30] M. G. Silveirinha, "Nonlocal homogenization model for a periodic array of ε-negative rod" *Phys. Rev. E* **73**, 046612, 2006.

[31] S. I. Maslovski, T. A. Morgado, M. G. Silveirinha, C. S. R. Kaipa, and A. B. Yakovlev, "Generalized additional boundary conditions for wire media", *New J. Phys.* **12**, 113047, 2010.

[32] M. G. Silveirinha, "Additional boundary conditions for nonconnected wire media", *New. J. Phys.* **11**, 113016, 2009.

[33] M. G. Silveirinha, P. A. Belov, and C. R. Simovski, "Subwavelength imaging at infrared frequencies using an array of metallic nanorods", *Phys. Rev. B* **75**, 035108, 2007.

[34] S. I. Maslovski, and M. G. Silveirinha, "Nonlocal permittivity from a quasistatic model for a class of wire media", *Phys. Rev. B* **80**, 245101, 2009.

[35] J. D. Jackson, *Classical Electrodynamics*, John Wiley, New York, 3rd Ed., 1999.

[36] S. J. Smith, and E. M. Purcell, "Visible Light from Localized Surface Charges Moving across a Grating", *Phys. Rev.* **92**, 1069, 1953.

[37] F. J. García de Abajo, "Interaction of Radiation and Fast Electrons with Clusters of Dielectrics: A Multiple Scattering Approach", *Phys. Rev. Lett.* **82**, 2776, 1999.

[38] F. J. García de Abajo, "Optical excitations in electron microscopy", *Rev. Mod. Phys.* **82**, 209, 2010.

[39] M. A. Ordal, R. J. Bell, R. W. Alexander, Jr., L. L. Long, and M. R. Query, "Optical properties of fourteen metals in the infrared and far infrared: Al, Co, Cu, Au, Fe, Pb, Mo, Ni, Pd, Pt, Ag, Ti, V, and W.", *Appl. Opt.* **24**, 4493, 1985.

[40] U. Kaatze, "Complex permittivity of water as a function of frequency and temperature", *J. Chem. Eng. Data* **34**, 371, 1989.

[41] L. Fülöp, and T. Biró, "Cherenkov radiation spectrum", *Int. J. of Theor. Phys*. **31**, 64, 1992.

IV. SPATIAL SOLITONS IN METALLIC NANOWIRE ARRAYS

IV.1. Introduction

This history of the previous century shows that the quest for increasingly small functional devices runs in parallel with new technological advances and breakthroughs. Importantly, the downscaling of photonic devices poses serious challenges, as the spatial confinement of light in natural materials is fundamentally limited by diffraction. A nonlinear response may be instrumental to surpass these limitations.

In the context of nonlinear phenomena in photonic systems, the formation and propagation of optical solitons is a subject that has fascinated the scientific community for a long time. Although several definitions can be used to describe the soliton, a simple picture of this phenomenon is a wave that maintains its shape while it propagates at a constant velocity in a medium. In optics, there can be two distinct types of solitary waves: temporal and spatial solitons. In the first case, the nonlinear response of the medium compensates the effects of dispersion in the propagation of a confined optical field [1]. This phenomenon allows sending pulses that do not change its shape as they propagate in the nonlinear medium. On the other hand, spatial solitons are often associated with the propagation of an optical field where the nonlinearities of the medium balance the effects of diffraction [1]. In these circumstances, the refractive index of the medium is changed by variations of the amplitude of the optical field, and the structure resembles a graded-index fiber. The tailoring of the refractive index of the medium allows the optical field to remain confined and maintain its shape while propagating in the medium.

As discussed in the previous chapters of this thesis, artificial media, and in particular metallic nanowire arrays, can open new inroads in photonics and enable the scattering engineering, enhancing the light emission by electrons, as well as many others, such as manipulating the electromagnetic radiation on a subwavelength scale [2-5]. Remarkably, it was predicted that the subwavelength manipulation of radiation in the wire media can also take place in the nonlinear regime, such that metallic nanowire arrays embedded in a nonlinear Kerr-type dielectric material may allow the formation and propagation of subwavelength spatial solitons [6-8] and other families of plasmonic lattice solitons [9,10]. A nonlinear Kerr-type dielectric medium is characterized by an electric permittivity that, for a fixed frequency, can be expressed as $\varepsilon = \varepsilon_h^0 \left(1 + \delta\varepsilon\right)$, where $\delta\varepsilon = \alpha \mathbf{e}^* \cdot \mathbf{e}$ is a nonlinear function of the microscopic electric field $\mathbf{e}$ and $\alpha = 3\chi^{(3)} / \varepsilon_{h,r}^0$ is a constant that determines the strength of the nonlinear effects and is proportional to the third order electric susceptibility $\chi^{(3)}$ of the material.

The findings of Refs. [6, 7, 9, 10] rely on a theoretical framework based on the coupled mode theory, which provides a somewhat limited physical understanding of the solitons formation mechanism in the metamaterial. More recently, Ref. [11] proposed an effective medium model for the nanowires metamaterial embedded in a Kerr-type dielectric material, which regards the structure as a continuous medium characterized by a few effective parameters. Using this effective medium framework, in Ref. [8] it was investigated the conditions for the formation and propagation of two-dimensional (2-D) unstaggered bright spatial solitons, i.e. modes that vary slowly in the scale of the period of the metamaterial.

In this Chapter it will be shown that the findings of Ref. [8] can be further extended to characterize the formation and propagation of three-dimensional (3-D) bright and dark spatial solitons with cylindrical symmetry. As the terminology of the latter

suggests, the physical behavior of dark solitons is much different from the bright solitons. In fact, stable dark spatial solitons consist of dip-like shapes in the amplitude of a constant wave background [12-14]. This is the opposite of the more typical bright solitons that are self-trapped localized states with a "pulse-like" shape. Depending on the amplitude of the dip in the constant wave and on the phase of the dark solitons profile, they can be classified as "black" dark spatial solitons – when the dip goes to zero and the phase is flat with an odd symmetry – or "gray" if the dip does not go to zero and the phase has odd symmetry but it is not flat [13, 14]. Dark spatial solitons have interesting properties such as the possibility of being created without a threshold in the input power [15, 16], amongst others.

Because our study uses the effective medium model of Ref. [11], the corresponding formalism will be briefly reviewed in Sec. IV.2. Using this framework, in Sec. IV.3 the conditions for the formation of solitary waves in the metamaterial will be discussed, particularly the type of nonlinear host medium required for the formation of bright and dark solitons: either a self-defocusing material, where $\chi^{(3)} < 0$, or a self-focusing material, for which $\chi^{(3)} > 0$. In Sec. IV.4 and IV.5 two families of 3-D spatial solitons with cylindrical symmetry will be characterized, and parametric numerical simulations will be presented to highlight the impact that structural parameters and losses have in the propagation of such solitary waves.

IV.2. Effective Medium Model for Nonlinear Nanowire Arrays

In this section, the effective medium model introduced in Ref. [11] for the uniaxial wire medium embedded in nonlinear Kerr-type dielectric is reviewed. Similarly to what was considered in Chapter II and Chapter III, the wire medium is formed by a set of infinitely long parallel metallic wires with complex permittivity ε_m and radius r that are arranged in a square lattice with period a, as shown in Fig. 4.1.

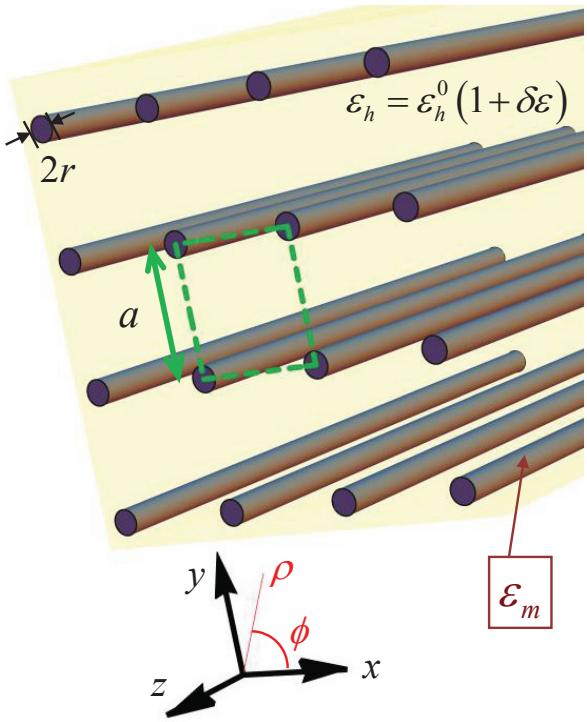

Fig. 4.1 Geometry of the periodic array of metallic nanowires embedded in a nonlinear Kerr-type host material.

However, in this case the host medium is a nonlinear Kerr-type dielectric material such that for a fixed frequency the electric permittivity can be expressed as $\varepsilon = \varepsilon_h^0\left(1+\alpha\mathbf{e}^*\cdot\mathbf{e}\right)$. In the homogenization model proposed in Ref. [11], the dynamics of the electromagnetic field is described by an eight component state vector $\left(\mathbf{E},\mathbf{H},\varphi,I\right)$ that in the absence of external optical sources, satisfies the following nonlinear first-order partial-differential system of equations:

$$\nabla \times \mathbf{E} = i\omega\mu_0 \mathbf{H}\,, \tag{4.1}$$

$$\nabla \times \mathbf{H} = -i\omega\varepsilon_{ef,h}\mathbf{E} + \frac{I}{A_c}\hat{\mathbf{z}} + \frac{1}{A_c}\mathbf{Y}\varphi\,, \tag{4.2}$$

$$\frac{\partial \varphi}{\partial z} = i\omega L\zeta_w I + E_z\,, \tag{4.3}$$

$$\frac{\partial I}{\partial z} = i\omega C_n \varphi - \mathbf{Y}\cdot\mathbf{E}_t\,. \tag{4.4}$$

Within this approach, **E** and **H** represent the macroscopic electromagnetic field (after spatial averaging of the microscopic fields **e** and **h**), I is the current that flows through the nanowires (interpolated in a such a manner that it is defined over all the space) [17] and φ is a quasistatic potential defined as the average potential drop measured from the center of the wire to the boundary of the unit cell [17]. Moreover $\zeta_w = 1 - \frac{Z_w}{i\omega L}$, $Z_w = -\left(i\omega\pi r^2(\varepsilon_m - \varepsilon_h^0)\right)^{-1}$ is the p.u.l. self-impedance of the nanowires [17], $L = \frac{\mu_0}{2\pi}\log\left(\frac{a^2}{4r_w(a-r)}\right)$ is the p.u.l. inductance of the wires [17] and $A_c = a^2$ is the area of the unit cell of the metamaterial. The parameters $\varepsilon_{ef,h}$, C, and **Y** are nonlinear functions of the macroscopic state variables and read [11]:

$$\varepsilon_{ef,h} = \varepsilon_h^0\left[1 + \alpha\left(\mathbf{E}\cdot\mathbf{E}^* + k_p^2\varphi\varphi^*\right)\right], \tag{4.5}$$

$$C_n = C^0\left[1 + \alpha\left(\mathbf{E}\cdot\mathbf{E}^* + \tilde{B}k_p^2\varphi\varphi^*\right)\right], \tag{4.6}$$

$$\mathbf{Y} = -i\omega C^0\frac{\alpha}{2}\left(\varphi\mathbf{E}_t^* + \varphi^*\mathbf{E}_t\right), \tag{4.7}$$

where $k_p = a^{-1}\sqrt{\mu_0/L}$ is the geometrical component of the plasma wave-number of the effective medium [17], $\mathbf{E}_t = E_x\hat{\mathbf{x}} + E_y\hat{\mathbf{y}}$ is the transverse component of the electric field,

$C^0 = k_p^2 \varepsilon_h^0 a^2$ and from Ref. [11], $\tilde{B} = 2\pi k_p^4 a^6 \int_r^a \left[\frac{1}{2\pi\rho} - \frac{1}{2\pi(a-\rho)} \right]^4 \rho d\rho$. As expected, if the nonlinearity is removed from the host medium, i.e. if $\alpha = 0$, the effective medium model reduces to that used in the Chapter II and Chapter III for the standard wire medium structure.

From Ref. [8, 11] it is known that paraxial optical beams propagating along the *z*-direction are expected to be quasiplane waves that barely penetrate into the metallic wires, so that the electric field is quasi-transverse $\left(|E_z| \ll |\mathbf{E}_t|\right)$. In fact, since φ corresponds to a potential that is created by the electric charge density induced in the metallic wires, it is also expected that $|\varphi/a| \ll |\mathbf{E}_t|$. Therefore, in the paraxial approximation, the nonlinear dynamics arising from contributions of φ and E_z may be neglected, so that $\mathbf{Y} = 0$ and the state variables $(\mathbf{E}, \varphi)$ satisfy the following second-order nonlinear partial-differential system:

$$\nabla \times \nabla \times \mathbf{E} - k_h^2 n_{ef,h}^2 \mathbf{E} = \frac{k_p^2}{\zeta_w} \left(\frac{\partial \varphi}{\partial z} - E_z \right) \hat{\mathbf{z}}, \tag{4.8}$$

$$\frac{\partial^2 \varphi}{\partial z^2} + k_h^2 \zeta_w n_{ef,h}^2 \varphi = \frac{\partial E_z}{\partial z}, \tag{4.9}$$

where the parameter $n_{ef,h}^2$ is the effective (squared) normalized refractive index of the host medium defined by:

$$n_{ef,h}^2 \approx 1 + \alpha \mathbf{E}_t^* \cdot \mathbf{E}_t. \tag{4.10}$$

Importantly, even for paraxial light beams, where $|E_z| \ll |\mathbf{E}_t|$, it is not possible to neglect E_z because in wire media the permittivity along the *z*-direction can be extremely large [17, 18], and thus the normalized *z*-component of the electric displacement D_z / ε_0 typically has a magnitude comparable to $|\mathbf{E}_t|$.

Assuming that the electromagnetic waves have a variation along the *z*-direction of the form $e^{ik_z z}$, Eq. (4.8) can be simplified to:

$$\nabla \times \nabla \times \mathbf{E} - \omega^2 \mu_0 \overline{\overline{\varepsilon}}_{eff}\left(\omega, k_z\right) \cdot \mathbf{E} = 0 \tag{4.11}$$

where $\overline{\overline{\varepsilon}}_{eff}\left(\omega, k_z\right)$ has the meaning of a nonlocal dielectric function that satisfies:

$$\frac{1}{\varepsilon_h^0} \overline{\overline{\varepsilon}}_{eff}\left(\omega, k_z\right) = n_{ef,h}^2 \overline{\overline{\mathbf{I}}} - \frac{1}{\zeta_w} \frac{k_p^2}{\left(k_h^2 - k_z^2 / n_w^2\right)} \hat{\mathbf{z}}\hat{\mathbf{z}} \,. \tag{4.12}$$

The parameter $n_w^2 \approx \zeta_w n_{ef,h}^2$ is the slow-wave factor with the same physical meaning as in Chapter II. Note that $\overline{\overline{\varepsilon}}_{eff}\left(\omega, k_z\right)$ is a nonlinear function of the transverse electric field because of the dependence on $n_{ef,h}^2$ (see Eq. (4.10)). In this level of approximation, the nonlinear effects in the host medium are manifested in the macroscopic response simply by replacing the microscopic expression of the host permittivity $\varepsilon_h = \varepsilon_h^0\left(1 + \alpha \mathbf{e}^* \cdot \mathbf{e}\right)$ by the macroscopic formula $\varepsilon_h = \varepsilon_h^0\left(1 + \alpha \mathbf{E}_t^* \cdot \mathbf{E}_t\right)$.

IV.3. Trapped States

In this section, we derive the conditions required for the formation of both bright and dark spatial solitons in the metamaterial.

IV.3.1. Photonic Modes

Similarly to what was done in Chapter II, the characteristic equation for the photonic modes can be obtained substituting the permittivity tensor (given by Eq. (4.12)) into the Maxwell equations and calculating the plane-wave solutions (eigenmodes) with a spatial variation of the form $e^{i\mathbf{k}\cdot\mathbf{r}}$, being $\mathbf{k} = \mathbf{k}_t + k_z \hat{\mathbf{z}}$, $\mathbf{k}_t = k_x \hat{\mathbf{x}} + k_y \hat{\mathbf{y}}$ the transverse part of the wave vector, and the direction of propagation corresponding the *z*-direction. This yields the following dispersion relation for TM-polarized eigenwaves [11]:

$$\frac{\left|\mathbf{k}_t\right|^2}{\varepsilon_{zz}} + k_z^2 = n_{ef,h}^2 k_h^2 \text{, with} \qquad \varepsilon_{zz} \equiv 1 - \frac{\beta_p^2}{\zeta_w n_{ef,h}^2 k_h^2 - k_z^2}. \tag{4.13}$$

The dispersion of the photonic states depends on $n_{ef,h}^2$ and thus on the intensity of the optical field. For a fixed value of $k_t = \left|\mathbf{k}_t\right|$, the dispersion relation (4.13) can be reduced to a quadratic polynomial equation in k_z^2. Consistent with Sec. II.2.1, the bulk wire medium supports two distinct propagating eigenmodes for TM-polarized excitations: a q-TEM mode and a TM mode [17, 18]. In this Chapter the focus will be on the q-TEM mode, as it has no cutoff frequency and is the only mode that propagates below the plasma frequency of the effective medium (frequency wherein $\varepsilon_{zz}(\omega, k_z) = 0$).

The isofrequency contours of the q-TEM mode may be obtained from the solution of Eq. (4.13) and correspond to hyperbolic contours [18, 19]. Therefore, to a first approximation, the effective medium can be regarded as a hyperbolic medium whose frequency contours depend on the structural parameters of the metamaterial [11] and also on the strength of the nonlinear effects ($n_{ef,h}^2$ is a function of the electric field amplitude). Hyperbolic metamaterials are of great interest due to their numerous applications such as the negative refraction of light [20], optimization of radiative heat transfer [21], enhancement of Casimir interaction [22], novel light sources based on the Cherenkov effect [J1, 23], amongst many others [24].

IV.3.2. Formation of Solitary Waves

Next we explain the physical mechanisms involved in the formation of solitons in wire media.

IV.3.2.1 Bright Solitons

To begin with, we discuss the formation of bright solitons in a standard nonlinear isotropic dielectric. It is well known that the formation of those trapped states requires that the nonlinear material is of the self-focusing type [1]. The profile of the spatial solitons changes the refractive index of the medium. Thus, the formation of the trapped states may be explained as a consequence of the total internal reflection caused by self-induced refractive index changes. The formation of trapped states can also be understood from the dynamics of the isofrequency contours of the photonic states as a function of the nonlinear effects. For a fixed frequency, a trapped state associated with a generic *z*-propagation constant k_{z0} is allowed if the medium supports a photonic state with $k_z = k_{z0}$ for strong electric field amplitudes and for weak electric fields there are no photonic states with $k_z = k_{z0}$ available for propagation. In other words, the radiation needs to be trapped for sufficiently strong electric field intensities and it is not coupled to photonic states associated with weak field amplitudes.

This can be better illustrated if we calculate the dispersion of the photonic states of a standard Kerr-type dielectric. The dispersion of the photonic states in conventional Kerr media reads:

$$k^2 c^2 = \omega^2 n^2 , \tag{4.14}$$

where *n* is the refractive index that grows with the amplitude of the electric field if it is a self-focusing medium or decreases if the medium is of a self-defocusing type. For both types of media the isofrequency contours are spherical surfaces whose radius varies with the field strength, as shown in Fig. 4.2.

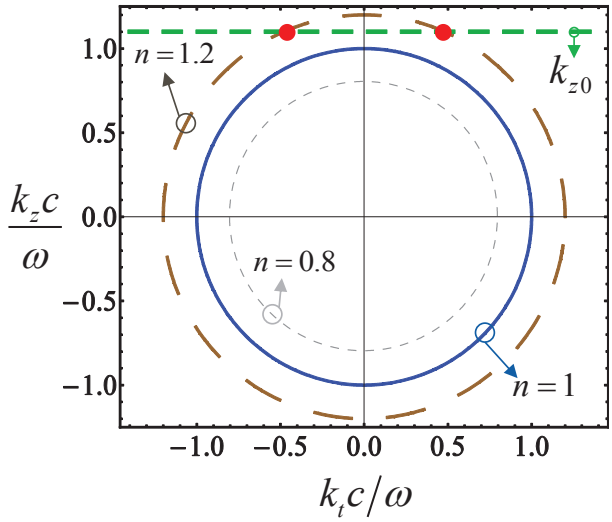

Fig. 4.2 Isofrequency contours of a conventional self-focusing Kerr dielectric for weak field amplitudes (solid blue line, $n=1.0$), for strong field amplitudes in self-focusing media (long dashed brown line, $n=1.2$), and for strong field amplitudes in self-defocusing media (dashed gray line, $n=0.8$). The red dots correspond to a trapped state associated with $k_z = k_{z0}$ that is allowed only in case of sufficiently strong fields. For clarity, in the figures we considered large variations of n.

The results of Fig. 4.2 reveal that in self-focusing media the radius of the spherical isofrequency surfaces increases with the amplitude of the electromagnetic field. Therefore, according to the previous discussion, a trapped state associated with a generic k_{z0} is required to satisfy $k_{z0} > n_0\omega/c$, being n_0 the refractive index for weak field amplitudes. This is shown in Fig. 4.2 as the green dashed horizontal line (photonic states with $k_z = k_{z0}$) intersects the isofrequency contour associated with a strong field intensity (red dots in the picture) but does not intersect the surface of allowed photonic states for low field amplitudes.

Understanding the formation of spatial solitons in natural media is useful, since the same concepts can be extended to the formation of spatial solitons in the nonlinear nanowire metamaterial. To this end, the first step is to study the impact of the nonlinear response on the dispersion of the effective medium. Using Eq. (4.13) the isofrequency contours of the q-TEM mode can be calculated for several values of $n_{ef,h}^2$. It is supposed that the nanowires are made of silver, so that in the infrared domain the complex

permittivity ε_m of silver may be described by a Drude model $\varepsilon_m - \varepsilon_h^0 \sim \varepsilon_0 \frac{-\omega_m^2}{\omega(\omega + i\Gamma)}$ with a plasma frequency $\omega_m/2\pi = 2175\,\text{THz}$ and a collision frequency $\Gamma/2\pi = 4.35\,\text{THz}$ [25]. Without any loss of generality it was considered that the wires have radius $r = 0.1a$, for a lattice period $a = 200\text{nm}$, and are embedded in a dielectric background with $\varepsilon_h^0 = \varepsilon_0$ for an operation wavelength $\lambda_0 = 1550\text{nm}$. Figure 4.3 shows the hyperbolic isofrequency contours of the photonic states for the case of a weak field intensity (i.e. in the linear regime - curve with $n_{ef,h}^2 = 1.0$), and for a strong field intensity in a self-focusing host medium (curve with $n_{ef,h}^2 > 1.0$) and in a self-defocusing host medium (curve with $n_{ef,h}^2 < 1.0$). For the sake of simplicity in these plots the material loss was neglected.

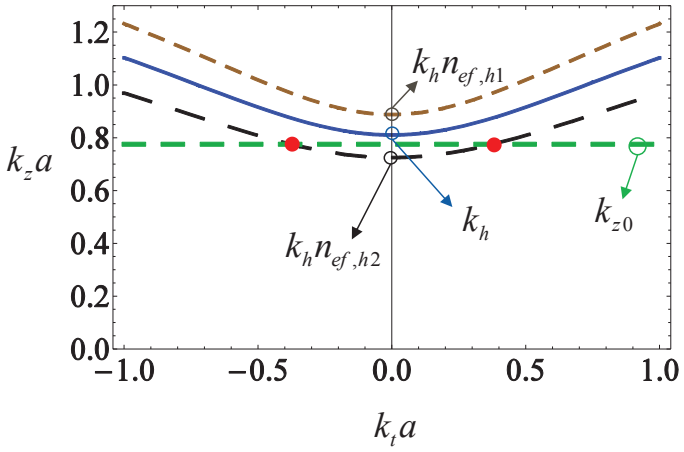

Fig. 4.3 Dispersion of the photonic states associated with the q-TEM mode in a silver nanowire material at $\lambda_0 = 1550\text{nm}$. The nanowires are embedded in a dielectric background with $\varepsilon_h^0 = \varepsilon_0$, the lattice period is $a = 200\text{nm}$, and the wire radius is $r = 0.1a$. The contours are calculated for: a self-focusing host material (dashed brown curves, $n_{ef,h1}^2 = 1.2$), a self-defocusing host material (long dashed black curves, $n_{ef,h2}^2 = 0.8$) and for a linear host (blue curves, $n_{ef,h}^2 = 1.0$). The red dots correspond to a trapped state associated with $k_z = k_{z0}$ that is allowed only in case of sufficiently strong fields. For clarity, in the figures we considered large variations of n and positive values of k_z.

As seen the topology of the isofrequency contours of the wire medium is completely different from those of Kerr-media depicted in Fig. 4.2. The differences between the

spherical isofrequency surfaces of conventional media and the hyperbolic isofrequency contours of the metamaterial influence the formation of spatial solitons in the nonlinear wire media. Importantly, the formation of bright solitons in the metamaterial is only possible if the radiation is trapped for a sufficiently strong optical field and no radiation is coupled to photonic states associated with weak field amplitudes. This means that a trapped state associated with a certain k_{z0} is only allowed if the metamaterial supports a photonic state with $k_z = k_{z0}$ for strong electric field amplitudes and there are no photonic states with $k_z = k_{z0}$ available for propagation in case of a weak electric field.

Using the isofrequency contours depicted in 4.3 , we can see that to fulfill these conditions it is necessary that the line $k_z = k_{z0}$ is below the vertex of the hyperbola (point of the hyperbola where $k_t = 0$ and $k_z = k_h n_{ef,h}$) associated with the weak nonlinearities (solid blue line). In this case, the green dashed horizontal line (photonic states with $k_z = k_{z0}$) only intersects the isofrequency contour associated with a strong field intensity in a self-defocusing medium (red dots in the picture). Therefore, under an effective medium framework, self-trapped states corresponding to bright solitons can only be formed when the dielectric host is a self-defocusing material [8]. Interestingly, it is seen that even though the dielectric host is a self-defocusing material, the effective medium behaves as a self-focusing material. However, it should be mentioned that it is possible to have staggered bright solitons when the host is a self-focusing material, but such solitary waves vary quickly on the scale of the unit cell of the metamaterial [7], and thus cannot be described using effective medium techniques.

IV.3.2.2 Dark Solitons

Next we discuss the formation of dark solitons. Similar to the previous subsection, first we consider simple isotropic Kerr-type dielectrics.

As discussed in Sec. IV.1, a dark soliton consists of a dip-like shape in the amplitude of a constant wave background. Thus, one may perceive the dark soliton as a weakly guided mode where most of the field energy is concentrated in the "cladding" region. Since in the "cladding" region the refractive index is smaller than in the "core", this type of behavior is consistent with a self-defocusing nonlinear medium, where the refractive index is depleted for strong optical intensities. In fact, it is well known stable dark solitons can only be formed in isotropic nonlinear media if the medium is of a self-defocusing type [13-16]. Although not as common as the self-focusing media, examples of self-defocusing materials include sodium vapor, some organic compounds and also certain polymers [26-28].

The formation mechanism of dark spatial solitons may also be understood from the isofrequency contours of Kerr-media depicted in Fig. 4.2. Since these trapped states are weakly guided by the "core", it becomes mandatory that for low field intensities (core region) there are allowed photonic states, while for strong field intensities (cladding region) all photonic states are forbidden. This corresponds to imposing that a trapped state associated with a generic k_{z0} satisfies the condition $k_{z0} < n_0\omega/c$, being n_0 the refractive index for weak field amplitudes. From Fig. 4.2 it follows that the line $k_z = k_{z0}$ needs to intersect the surface associated with weak nonlinearities (solid blue curve), while it cannot intersect the curve associated with a strong optical field. Crucially, this is only satisfied in case of self-defocusing materials (gray dashed line in Fig. 4.2).

The conditions required for the formation of dark solitons in nonlinear nanowire metamaterials can also be studied using similar ideas. As previously discussed, it must

be ensured that for low field intensities there are allowed photonic states, while for strong field intensities there are no photonic states available for propagation. The two conditions can be satisfied simultaneously only if the line $k_z = k_{z0}$ is above the vertex of the blue hyperbola in Fig. 4.3 and below the vertex of a hyperbola associated with a strong field intensity. Evidently, this is only possible when the host is a self-focusing material (brown hyperbola). Thus, to have dark spatial solitons it is necessary that for $k_t = 0$ the condition $k_h < k_{z0} < k_h n_{ef,h1}$ is satisfied. Again, even though the dielectric host medium is a self-focusing material, the effective medium behaves as a self-defocusing medium.

IV.4. Bright Spatial Solitons

Based on the effective medium model introduced in Sec. IV.2, in this section we characterize a family of 3-D bright spatial solitons with cylindrical symmetry. We study the effects of the isofrequency contours on the confinement of the solitary waves, and the impact of dielectric and metal absorption on the propagation of such solitons. Without any loss of generality, it is supposed that the wires are made of silver and the losses in the dielectric are modeled by the loss tangent $\tan\delta$, such that $\varepsilon_h^0 = \varepsilon_0\left(1 + i\tan\delta\right)$.

Because of the interest in solitary waves with cylindrical symmetry, it is convenient to use cylindrical coordinates, such that the transverse part of the electric field is given by $\mathbf{E}_t = E_\rho \hat{\boldsymbol{\rho}} + E_\phi \hat{\boldsymbol{\phi}}$, where E_ρ, E_ϕ are the radial and azimuthal components of the electric field (see Fig. 4.1). The family of solitons studied in this section is characterized by a transverse electric field which only has a radial component and a radial variation, i.e. the solitons have $E_\phi = 0$ and $\frac{\partial}{\partial\phi} = 0$. For this family of spatial solitons it can be

checked that the electric field satisfies $\hat{\boldsymbol{\rho}}\cdot\nabla^2\mathbf{E}=\nabla^2E_\rho-E_\rho/\rho^2$. Using this result, together with the inner product of both sides of Eq. (4.11) with the radial unity vector $\hat{\boldsymbol{\rho}}$, it is found that:

$$\frac{\partial}{\partial\rho}\nabla\cdot\mathbf{E}-\nabla^2E_\rho+E_\rho/\rho^2=k_h^2n_{ef,h}^2E_\rho. \tag{4.15}$$

Moreover, from Eq. (4.11) it follows that $\nabla\cdot\left[\overline{\overline{\varepsilon}}_{eff}\left(\omega,k_z\right)\cdot\mathbf{E}\right]=0$ with $k_z=-i\dfrac{\partial}{\partial z}$. Neglecting the spatial variation of $n_{ef,h}^2$, this implies that the divergence of the electric field is equal to:

$$\nabla\cdot\mathbf{E}=\rho^{-1}\frac{\partial}{\partial\rho}\left(\rho E_\rho\right)\left(1-\varepsilon_{zz}^{-1}\right), \tag{4.16}$$

where $\varepsilon_{zz}\left(\omega,k_z\right)$ is defined as in Eq. (4.13). Substituting this result into Eq. (4.15), and writing the radial component of the electric field as $E_\rho=\tilde{E}_\rho\left(\rho,z\right)e^{ik_zz}$, where the $\tilde{E}_\rho\left(\rho,z\right)$ is an envelope function supposed to vary slowly compared to the propagation factor, one finally finds that the field envelope is satisfies:

$$\frac{1}{\varepsilon_{zz}\left(\omega,k_z\right)}\left(\frac{\partial^2\tilde{E}_\rho}{\partial\rho^2}+\frac{1}{\rho}\frac{\partial\tilde{E}_\rho}{\partial\rho}-\frac{\tilde{E}_\rho}{\rho^2}\right)+2ik_z\frac{\partial}{\partial z}\tilde{E}_\rho=\left(k_z^2-k_h^2n_{ef,h}^2\right)\tilde{E}_\rho. \tag{4.17}$$

This second order nonlinear differential equations can be numerically solved to calculate the profile of the soliton and its spatial evolution. To determine the spatial solitons profile, the material loss parameters are set to zero (in both dielectric host and metallic wires) and the solution of Eq. (4.17) is calculated with $\dfrac{\partial}{\partial z}=0$, i.e. assuming that the field envelope is independent of the *z*-coordinate. It is important to mention that consistent with the hypothesis that the field envelope is slowly varying in space, the

standard paraxial approximation $\frac{\partial^2}{\partial z^2} \to 2ik_z \frac{\partial}{\partial z} - k_z^2$ was used in the derivation of Eq. (4.17).

Crucially, since Eq. (4.17) is a second order differential equation, two suitable boundary conditions must be specified to numerically solve the equation. The first condition is $\tilde{E}_\rho\big|_{\rho=0} = 0$, because the cylindrical symmetry of the solitary waves with $E_\phi = 0$ implies that the radial component is also null at the origin. The second boundary condition is determined by the value of the radial derivative of the electric field at the origin $\left.\frac{\partial \tilde{E}_\rho}{\partial \rho}\right|_{\rho=0^+} = A$, where A is a constant that depends on k_z and on the structural parameters of the metamaterial. This constant is calculated iteratively by imposing that the field vanishes as $\rho \to +\infty$.

In summary, the profile of bright solitons with $E_\phi = 0$ and $\frac{\partial}{\partial \phi} = 0$ can be obtained by solving Eq. (4.17) with $\frac{\partial}{\partial z} = 0$ and no material losses, and imposing the boundary conditions:

$$\tilde{E}_\rho\big|_{\rho=0^+} = 0 \text{ and } \left.\frac{\partial \tilde{E}_\rho}{\partial \rho}\right|_{\rho=0^+} = A. \tag{4.18}$$

Using these ideas, the profile of bright spatial solitons was calculated for an array of silver nanowires embedded in a self-defocusing medium, for $k_z = 0.995k_h$ and different frequencies of operation and structural parameters. The results are shown in Fig. 4.4**(a)**, where it is depicted the electric field envelope normalized to the strength of the nonlinear response (α). The numerical simulations confirm that bright solitons are allowed when the host medium is a self-defocusing material. The cylindrical symmetry

of the solitary waves together with the initial condition $\tilde{E}_\rho\big|_{\rho=0^+}=0$ forces the electric field maximum not to be centered at $\rho=0$. Consistent with the self-defocusing host it is seen, in Fig. 4.4**(b)**, that the refractive index is depleted in the regions of strong field intensity.

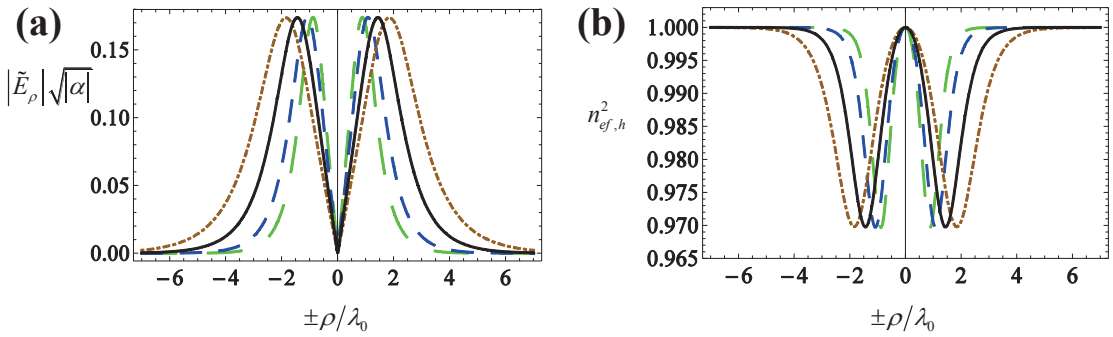

Fig. 4.4 Normalized field envelope $|\tilde{E}_\rho|\sqrt{|\alpha|}$ (panel **(a)**) and profile of the refractive index (panel **(b)**) associated with a spatial soliton with $k_z=0.995k_h$. The silver nanowire array is embedded in a dielectric host with $\varepsilon_h^0=\varepsilon_0$, the nanowires radius is $r=20\text{nm}$ and the lattice period and wavelength are such that: Long dashed green lines: $r_w/a=0.15$, $\lambda_0=1550\text{nm}$; Solid black lines: $r/a=0.1$, $\lambda_0=1550\text{nm}$; Dashed-dotted brown lines: $r/a=0.1$, $\lambda_0=1300\text{nm}$; Dashed blue lines: $r/a=0.15$, $\lambda_0=1300\text{nm}$.

The results shown in Fig. 4.4**(a)** also reveal the influence of the structural parameters and the oscillation frequency on the characteristic beamwidth of the trapped states. It is seen that the confinement of the solitons is worse for dilute systems, i.e. system with small r/a (thin nanowires), and for short wavelengths of operation, two scenarios for which the isofrequency contours of the wire media have a more pronounced hyperbolicity. This is consistent with the findings of Ref. [8], where it was shown that the spatial confinement is determined by the degree of hyperbolicity of the isofrequency contours, such that for the same optical field intensity the confinement is poorer for metamaterials with more pronounced hyperbolic dispersion. Ultimately, when the metallic wires are made of a PEC material such that $\zeta_w=1.0$ and $n^2_{ef,h}=1.0$, the isofrequency contours correspond to two flat parallel lines and it is possible to have spatial-solitons with a vanishingly small nonlinear response [8]. Indeed, it is well

known that for PEC nanowires the metamaterial supports diffractionless propagation of light beams even in the linear regime [3, 8, 19]. The strength of the electric field required to have a subwavelength modal size ($W < \lambda_0$) in the nonlinear wire media will be discussed further ahead.

To characterize the effect of losses in the propagation of the solitary waves, the term $2ik_z\partial_z\tilde{E}_\rho$ and the parameters associated with dielectric and metal dissipation in Eq. (4.17) are retained, and this equation is now solved subject to a new set of boundary conditions. The pertinent boundary conditions are such that $\tilde{E}_\rho(\rho, z=0)$ is taken equal to the profile of the spatial soliton calculated in the absence of loss, and $\tilde{E}_\rho(\rho_{\max}, z) = 0$ where $\rho_{\max} >> W$ and W is the characteristic half-power beamwidth of the soliton [8], which ensures that the profile of the soliton vanishes for a very large radial distance. Figure 4.5**(a)** reports the spatial evolution of a self-trapped wave associated with $k_z = 0.990k_h$ at $\lambda_0 = 1550\text{nm}$, after a propagation distance of $12\lambda_0$ in the *z*-direction in a nonlinear wire media characterized by a self-defocusing host, silver nanowires with $r = 20\text{nm}$ and lattice period $a = 200\text{nm}$, for several lossy scenarios. As previously discussed, the dissipation in the silver nanowires is modeled by the collision frequency parameter of the Drude model, that is equal to $\Gamma/2\pi = 4.35\text{THz}$ [25], whereas the dielectric loss is modeled by the loss tangent $\tan\delta$ which is set to $\tan\delta = 0.01$.

The results depicted in Fig. 4.5**(a)** reveal that the dominant absorption mechanism of the optical field is dielectric heating. Indeed, the effect of metallic loss may be negligible at $\lambda_0 = 1550\text{nm}$, at least for the considered level of dielectric loss. This type of behavior is consistent with the fact that the light beam is a q-TEM beam, such that its energy is mostly concentrated in the dielectric region. Therefore, the optical field is

much more sensitive to absorption in the host medium rather than to the absorption in metal.

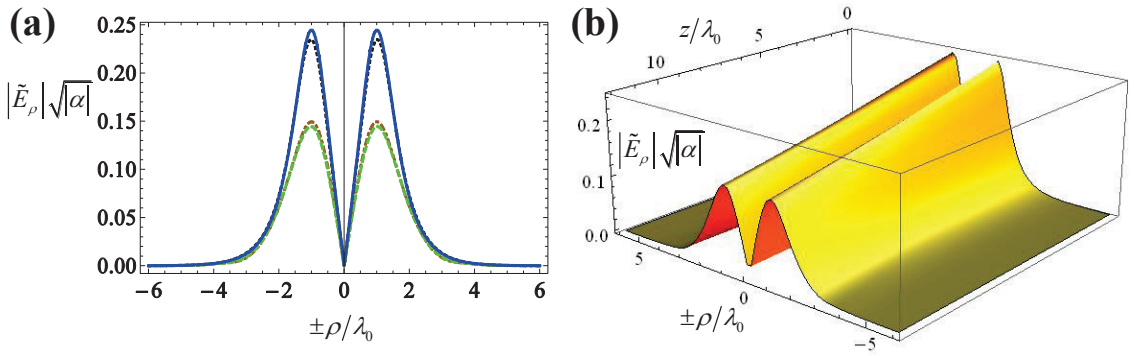

Fig. 4.5 Panel **(a)** Normalized field envelope $|\tilde{E}_\rho|\sqrt{|\alpha|}$ for a spatial soliton with $k_z = 0.990k_h$ in a nanowire metamaterial with a dielectric host with $\varepsilon_h^0 = \varepsilon_0(1+i\tan\delta)$ and silver nanowires with radius $r = 20\text{nm}$, lattice period $a = 200\text{nm}$, after a propagation distance of $12\lambda_0$ with $\lambda_0 = 1550\text{nm}$. Solid blue curves: lossless case; Black dotted curves: with metallic loss; Dot-dashed brown curves: dielectric loss tangent $\tan\delta = 0.01$ and no metallic loss; Green curves: with dielectric and metallic loss. Panel **(b)** Profile of the spatial soliton as it propagates along the *z*-direction and both metal and dielectric absorption are considered. The remaining structural parameters are as in panel **(a)**.

This is emphasized in Fig. 4.5**(b)** where it is depicted the profile of the spatial soliton calculated as it propagates along the *z*-direction considering both metal and dielectric absorption.

IV.5. Dark Spatial Solitons

Next, the study of the previous section is extended to dark spatial solitons of the same family, i.e. dark solitons with cylindrical symmetry and with $E_\phi = 0$ and $\frac{\partial}{\partial\phi} = 0$. Consistent with the findings of Sec. IV.3.2.2, now the host medium needs to be of the self-focusing type with $\alpha > 0$.

The formalism used to characterize the dark solitons is the same as in Sec. IV.4. In particular, the electric field associated with the dark spatial solitons satisfies the same nonlinear second order differential equation, i.e. Eq. (4.17), and the boundary conditions listed in Eq. (4.18) are also the same. However, since stable dark spatial solitons consist

of dip-like shapes in the amplitude of a constant wave background [12-14], the constant $\left.\frac{\partial \tilde{E}_\rho}{\partial \rho}\right|_{\rho=0^+} = A$ is now iteratively tuned so that the electric field tends to a non-zero constant value as $\rho \to +\infty$.

Using this effective medium framework the profile of the dark solitons associated with $k_z = 1.005 k_h$ was calculated for different structural parameters and wavelengths of operation. The results are depicted in Fig. 4.6.

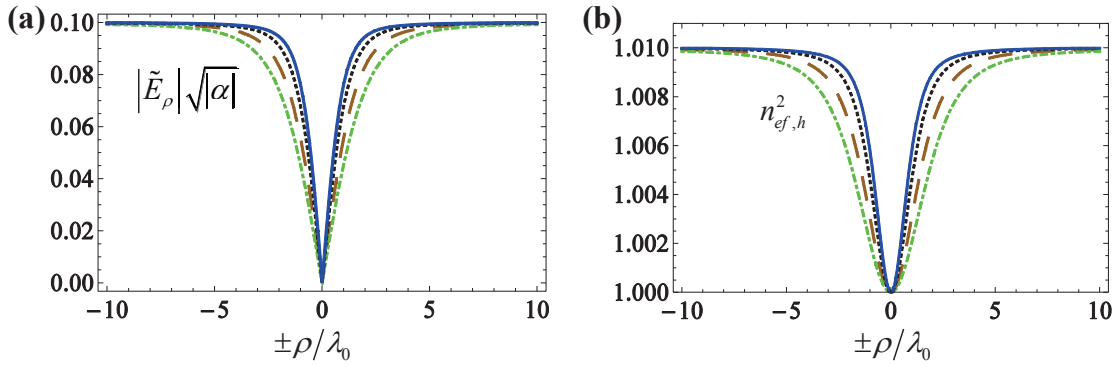

Fig. 4.6 Profile of **(a)** the radial electric field envelope $|\tilde{E}_\rho|\sqrt{|\alpha|}$ and **(b)** refractive index associated with a spatial soliton with $k_z = 1.005 k_h$. The silver nanowire array is embedded in a self-focusing dielectric host with $\varepsilon_h^0 = \varepsilon_0$, has a lattice period $a = 200\,\text{nm}$ and the nanowire radius and the wavelength of operation are such that: Dot-dashed green lines: $r = 20\,\text{nm}$, $\lambda_0 = 1300\text{nm}$; Dotted black lines: $r = 30\,\text{nm}$, $\lambda_0 = 1300\text{nm}$; Solid blue lines: $r = 30\,\text{nm}$, $\lambda_0 = 1550\text{nm}$; Dashed brown lines: $r = 20\,\text{nm}$, $\lambda_0 = 1550\text{nm}$.

As expected, the solitons consist of a dip-like shape in a constant wave background [12-14] and this type of behavior also extends to the refractive index profiles shown in Fig. 4.6 **(b)**, where consistent with the self-focusing host, the refractive index increases in the regions of strong field intensity. The specific type of dark solitons, either "gray" or "dark", is related to the behaviour of the dip in the constant wave and to the phase of the dark solitons. Since the electric field is null at the origin and the profile of the envelopes phase is flat, these solitons are of the "black" type. Moreover, the results of Fig. 4.6**(a)** also reveal that the characteristic size of the solitary waves is strongly influenced by the hyperbolicity of the isofrequency contours of the wire medium.

Similar to the results shown in Fig. 4.4**(a)** for the 3-D bright solitons, it is seen that structural parameters that originate a more pronounced hyperbolic dispersion, such as dilute systems and smaller wavelengths of operation, also increase the characteristic size of the solitary beams.

The strength of the nonlinear effects required to obtain a "black" dark soliton is also comparable to what is required for the formation of bright solitons. In fact it is interesting to compare the half-power beamwidth W of the spatial solitons as a function of the peak value of the normalized squared amplitude of the electric field $|\alpha||E|^2$ for both dark solitons and bright solitons. This is shown in Fig. 4.7 for 3-D spatial solitons propagating in an array formed by lossless silver nanowires with radius $r = 30\text{nm}$, lattice period $a = 150\text{nm},$ embedded in a dielectric host with $\varepsilon_h^0 = \varepsilon_0$ at an operating wavelength $\lambda_0 = 1550\text{nm}$. As seen, the beamwidth W is very similar for both types of solitons.

Moreover, since $|\alpha||E|^2$ is equal to the maximum variation on the refractive index profile ($n_{ef,h}^2 = 1 + \alpha \mathbf{E}_t^* \cdot \mathbf{E}_t$ with $\mathbf{E}_t = E_\rho \hat{\boldsymbol{\rho}}$) it can be checked that to have a subwavelength modal size ($W < \lambda_0$) it is necessary that $n_{ef,h}^2 \approx 1.0146$ for the dark solitons and $n_{ef,h}^2 \approx 0.983$ for the bright solitons, which in practice may be rather challenging to obtain.

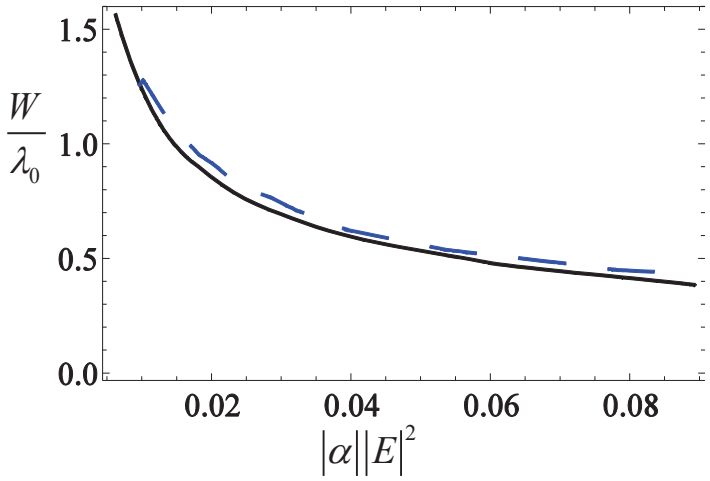

Fig. 4.7 Normalized half-power beamwidth W of 3-D spatial solitons as a function of the peak value of $|\alpha||E|^2$. The nanowire array is formed by lossless silver nanowires with radius $r = 30\text{nm}$, lattice period $a = 150\text{nm}$, embedded in a dielectric host with $\varepsilon_h^0 = \varepsilon_0$ at the wavelength $\lambda_0 = 1550\text{nm}$. Solid curve: bright solitons family; Dashed curve: dark solitons family.

The effect of dielectric and metal loss in the propagation of the dark solitons is studied in Fig. 4.8. In this figure it is represented the spatial evolution of a dark spatial solitary wave associated with $k_z = 1.005k_h$ at $\lambda_0 = 1550\text{nm}$, propagating in a nonlinear wire media characterized by silver nanowires with radius $r = 30\text{nm}$, lattice period $a = 150\text{nm}$ and a self-focusing host, after a propagation distance of $5\lambda_0$ in the z-direction, for several lossy scenarios. The numerical technique used to obtain these results was the same as described in Sec. IV.4 for the effect of losses in the spatial evolution of bright solitons, i.e. solving Eq. (4.17) with the term $2ik_z\partial_z\tilde{E}_\rho$ and the parameters associated with dielectric and metal dissipation. However, the pertinent boundary conditions are now slightly different. Similar to what was done for the bright solitons, the function $\tilde{E}_\rho(\rho, z=0)$ is taken equal to the profile of the spatial soliton calculated in the absence of loss. In addition, we impose that $\frac{\partial}{\partial\rho}\tilde{E}_\rho(\rho_{\max}, z) = 0$, which ensures the characteristic constant wave background of dark solitons.

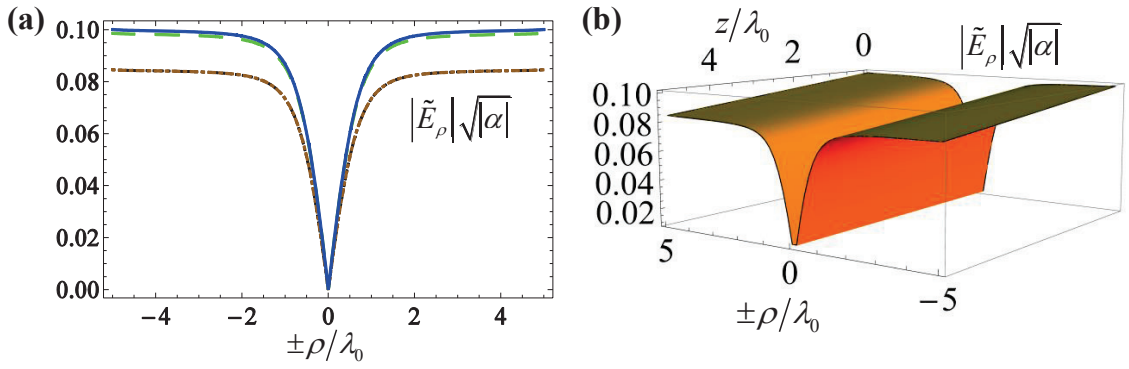

Fig. 4.8 Panel **(a)** Normalized field envelope $|\tilde{E}_\rho|\sqrt{|\alpha|}$ for a dark spatial soliton with $k_z = 1.005k_h$ in a nanowire metamaterial with a dielectric host with $\varepsilon_h^0 = \varepsilon_0(1 + i\tan\delta)$ and silver nanowires with radius $r = 30\text{nm}$, lattice period $a = 150\text{nm}$, after a propagation distance of $5\lambda_0$ with $\lambda_0 = 1550\text{nm}$. Solid blue curves: lossless case; Green curves: with metallic loss; Dot-dashed brown curves: dielectric loss tangent $\tan\delta = 0.01$ and no metallic loss; Black dotted curves: with dielectric and metallic loss. Panel **(b)** Profile of the spatial soliton as it propagates along the *z*-direction and both metal and dielectric absorption are considered. The remaining structural parameters are as in panel **(a)**.

The results depicted in Fig. 4.8 are qualitatively analogous to the bright solitons studied in Sec. IV.4 (see Fig. 4.5), as it is seen that the dissipation in the metamaterial is dominated by losses in the dielectric host rather than in the metallic wires.

IV.6. Concluding Remarks

In this chapter we studied the formation and propagation of three dimensional bright and dark unstaggered spatial solitons with cylindrical symmetry in a nanowire array embedded in a Kerr-type nonlinear medium. The analysis was performed based on an effective medium theory introduced in [8, 11], and it was found that unlike conventional nonlinear dielectric media, within an effective medium framework dark (bright) solitons can be formed only when the host medium is a self-focusing (defocusing) Kerr dielectric.

In Sec. IV.4 we developed a formalism that allowed for the complete characterization of the spatial solitons. The proposed theory applies to both bright and dark spatial solitons, with the only differences being in the boundary conditions used to numerically solve the problem. Using this framework, we performed a numerical

analysis to study the influence of the structural parameters of the metamaterial and the oscillation frequency on the confinement of the solitary waves. It was checked that for both dark and bright solitons, variations of the structural parameters that increase the hyperbolicity of the isofrequency contours of the metamaterial, will be detrimental to the confinement of the solitons.

It was also confirmed that the main decay channel of the solitons is associated with absorption in the dielectric host rather than metallic loss, which typically is of secondary importance. Moreover, it was shown that for sufficiently large optical field intensities, the spatial solitons can, in theory, have a subwavelength modal size ($W < \lambda_0$). However, the required field strength may be rather difficult to achieve.

As a final remark, it is important to mention that in Ref. [J3] we investigated another family of bright solitons, characterized by a transverse electric field $\mathbf{E}_t = E_\rho \hat{\boldsymbol{\rho}} + E_\phi \hat{\boldsymbol{\phi}}$ and an azimuthal derivative $\frac{\partial}{\partial \phi} = im$, with $m = \pm 1$. It was checked that spatial solitons of this new family have an optical field with a maximum at $\rho = 0$, i.e. at the beam center. The dependence of the solitons with respect to variations of structural parameters, operating frequency and losses are qualitatively similar to what was reported in Sec. IV.4.

References

[1] R. W. Boyd, *Nonlinear Optics*, Elsevier, Amsterdam, 3rd Ed., 2008.

[2] C. R. Simovski, P. A. Belov, A. V. Atrashchenko, and Y. S. Kivshar, "Wire Metamaterials: Physics and Applications", *Adv. Mater.* **24**, 4229, 2012.

[3] P. A. Belov, Y. Hao, and S. Sudhakaran, "Subwavelength microwave imaging using an array of parallel conducting wires as a lens", *Phys. Rev. B* **73**, 033108 , 2006.

[4] P. Ikonen, C. Simovski, S. Tretyakov, P. Belov, and Y. Hao, "Magnification of subwavelength field distributions at microwave frequencies using a wire medium slab operating in the canalization regime", *Appl. Phys. Lett.* **91**, 104102, 2007.

[5] G. Shvets, S. Trendafilov, J. B. Pendry, and A. Sarychev, "Guiding, Focusing, and Sensing on the Subwavelength Scale Using Metallic Wire Arrays", *Phys. Rev. Lett.* **99**, 053903, 2007.

[6] Y. Liu, G. Bartal, D. A. Genov, and X. Zhang, "Subwavelength Discrete Solitons in Nonlinear Metamaterials", *Phys. Rev. Lett.* **99**, 153901, 2007.

[7] F. Ye, D. Mihalache, B. Hu, and N. C. Panoiu, "Subwavelength Plasmonic Lattice Solitons in Arrays of Metallic Nanowires", *Phys. Rev. Lett.* **104**, 106802, 2010.

[8] M. G. Silveirinha, "Theory of Spatial Optical Solitons in Metallic Nanowire Materials", *Phys. Rev. B* **87**, 235115, 2013.

[9] F. Ye, D. Mihalache, B. Hu, and N. C. Panoiu, "Subwavelength vortical plasmonic lattice solitons", *Opt. Lett.* **36**, 1179, 2011.

[10] Y. Kou, F. Ye, and X. Chen, "Multipole plasmonic lattice solitons", *Phys. Rev. A* **84**, 033855, 2011.

[11] M. G. Silveirinha, "Effective Medium Response of Metallic Nanowire Arrays with a Kerr-type Dielectric Host", *Phys. Rev. B* **87**, 165127, 2013.

[12] A. Hasegawa, and F. Tappert, "Transmission of stationary nonlinear optical pulses in dispersive dielectric fibers. II. Normal dispersion", *Appl. Phys. Lett.* **23**, 171, 1973.

[13] Y. S. Kivshar, "Dark solitons in nonlinear optics", *IEEE J. Quantum Electron.* **29**, 250, 1993.

[14] Y. S. Kivshar, and B. Luther-Davies, "Dark optical solitons: physics and applications", *Phys. Rep.* **298**, 81, 1998.

[15] S. A. Gredeskul, and Y. S. Kivshar, "Generation of dark solitons in optical fibers", *Phys. Rev. Lett.* **62**, 977, 1989.

[16] S. A. Gredeskul, and Y. S. Kivshar, "Dark soliton generation in optical fibers", *Opt. Lett.* **14**, 1281, 1989.

[17] S. I. Maslovski, and M. G. Silveirinha, "Nonlocal permittivity from a quasistatic model for a class of wire media", *Phys. Rev. B* **80**, 245101, 2009.

[18] M. G. Silveirinha, "Nonlocal homogenization for a periodic array of ε-negative rods", *Phys. Rev. E* **73**, 046612, 2006.

[19] M. G. Silveirinha, P. A. Belov, and C. R. Simovski, "Subwavelength imaging at infrared frequencies using an array of metallic rods", *Phys. Rev. B* **75**, 035108, 2007.

[20] J. Yao, Z. Liu, Y. Wang, C. Sun, G. Bartal, A. M. Stacy, and X. Zhang, "Optical Negative Refraction in Bulk Metamaterials of Nanowires", *Science* **321**, 5891, 2008.

[21] C. R. Simovsky, S. Maslovski, I. Nefedov, and A. Tretyakov, "Optimization of radiative heat transfer in hyperbolic metamaterials for thermophotovoltaic applications", *Opt. Express* **21**, 14988, 2013.

[22] T. Morgado, S. Maslovski, and M. Silveirinha, "Ultrahigh Casimir interaction torque in nanowire systems", *Opt. Express* **21**, 14943, 2013.

[23] V. V. Vorobev, and A. V. Tyukhtin, "Nondivergent Cherenkov Radiation in a Wire Metamaterial", *Phys. Rev. Lett.* **108**, 184801, 2012.

[24] C. L. Cortes, W. Newman, S. Molesky, and Z. Jacob, "Quantum nanophotonics using hyperbolic metamaterials", *J. Opt.* **14**, 063001, 2012.

[25] M. A. Ordal, R. J. Bell, R. W. Alexander Jr., L. L. Long, and M. R. Querry, "Optical properties of fourteen metals in the infrared and far infrared: Al, Co, Cu, Au, Fe, Pb, Mo, Ni, Pd, Pt, Ag, Ti, V, and W", *Appl. Opt.* **24**, 4493, 1985.

[26] G. A. Swartzlander Jr., D. R. Andersen, J. J. Regan, H. Yin, and A. E. Kaplan, "Spatial dark-soliton stripes and grids in self-defocusing materials", *Phys. Rev. Lett.* **66**, 1583, 1991.

[27] R. W. Boyd, and G. L. Fischer, *Nonlinear Optical Materials, Encyclopedia of Materials: Science and Technology*, Elsevier, Oxford, 2nd Ed., 2001.

[28] L. Kamath, K. B. Manjunatha, S. Shettigar, G. Umesh, B. Narayana, S. Samshuddin, and B. K. Sarojini, "Investigation of third-order nonlinear and optical power limiting properties of terphenyl derivatives", *Opt. Laser Technol.* **56**, 425, 2014.

V. GRAPHENE SUPERLATTICES

V.1. Introduction

As discussed in Chapter I, despite the fundamental differences between electrons and photons, there are important similarities between the wave propagation of light and matter in periodic structures [1]. For instance, since an electron is characterized by a de Broglie wavelength, it can interfere with itself, similar to the interference phenomena in electromagnetism. The parallelism also extends to the influence of the band structure in the motion of electrons in semiconductors and light propagation in photonic crystals [1, 2, 3], amongst others [4].

In 1970, Esaki and Tsu [6] set an important milestone in using artificial media in electronics. In their seminal work, they suggested that superlattices obtained by variations in the composition of certain alloys or by periodically doping a monocrystalline semiconductor, might allow engineering the conduction and valence bands into many sub-bands and permit a negative differential conductance in the medium. This work ultimately proved to be invaluable to numerous advances in electronics, including the invention of quantum cascade lasers [7], the realization of semiconductor superlattices with an ultra-high mobility [8, 9], amongst many others [10].

Aside from some isolated studies [11, 12] the parallelisms between electromagnetic metamaterials and superlattices received little attention in the scientific literature. However, a significant effort was recently made to bridge these two fields of physics, particularly extending the concept of transformation optics to matter waves [10],

proposing several designs to obtain the electronic analogs of the Veselago-Pendry lens [12, 13], and in the development of the effective medium techniques to characterize the propagation electron waves in semiconductors [4], artificial graphene [14] and graphene superlattices [15]. This Chapter follows this paradigm as we study the electronic analogs of some phenomena typically associated with photons in metamaterials in the context of graphene based structures.

Graphene is a two-dimensional material that consists of a one-atom thick monolayer of graphite where the carbon atoms are arranged in a honeycomb-shaped lattice. This material is characterized by unusual properties, such as a remarkably high crystal quality and an unusual electronic "relativistic" spectrum that creates many intriguing and exciting opportunities in low-dimensional physics, such as the possibility of mimicking quantum relativistic phenomena in a condensed-matter system [16-22]. Since the first experimental realization of graphene [23], several modifications of the original structure have been proposed [24, 25]. These modifications aim to provide some control over the transport properties of electrons in graphene, and it has been recently suggested that the proper tailoring of an externally-applied periodic electrostatic potential on the surface of graphene, may allow gaining some control over the propagation of the charge carriers [26-28]. These structures, known as graphene superlattices, may be realized using different techniques, such as periodically patterned gates, deposition of adatoms on graphene's surface, or using a crystalline substrate [29-34]. Graphene superlattices may also enable to mimic some electromagnetic phenomena in systems dealing with matter waves [26-28], such as permitting to obtain an electron "perfect lens" [15, 35]. In the work reported in [15, 35] it was suggested that in some conditions two materials with complementary properties may effectively behave as some form of "matter-antimatter" and annihilate one another from the electronic point

of view, such that the paired materials provide a perfect "tunnel" for *any* extended or bounded stationary states. This "wormhole" connects two regions of space, as if the region in between was nonexistent, allowing to delocalize the wave function stationary states, similar to the light wormholes [36] based on transformation optics [37-39].

Building on these studies, in this chapter it is investigated the existence of electron wormholes based on one-dimensional (1-D) graphene superlattices, and unveil the actual physical response provided by such structures. To do so, we use an effective medium model framework that allows to completely characterize the propagation of electron waves in graphene based heterostructures. This framework will be introduced in Sec. V.2, and it relies on the effective medium model proposed in Ref. [15]. With the purpose of validating the effective medium model framework, in Sec. V.3 we present a thorough numerical comparison between the scattering properties of a cascade of GSL slabs calculated with both the macroscopic and microscopic approach (where all the granular details of the superlattice are retained).

Section V.4 investigates the possibility of having the negative refraction of electron waves at the heterojunction of graphene based heterostructures. It is important to mention that the negative refraction of electron waves was already proposed in previous works as the basis for the electronic analog of the Veselago's lens [12, 15]. In Ref. [12] it was shown that using a *p*-*n* junction in graphene would allow obtaining a Veselago's lens under a semi-classical approach, and in Ref. [15] it was proposed that two properly tailored graphene superlattices would generalize this behavior to all complex electronic states.

Finally, Sec. V.5 studies the possibility of obtaining wormholes for electron waves using graphene superlattice structures.

V.2. Effective Medium Model for Electron Wave Propagation

Similar to what was done in the previous chapters of this thesis for nanowire arrays, one can model graphene based nanomaterials as continuous media. In fact, according to the findings reported in Ref. [15], provided the initial electronic state is not more localized than the characteristic period *a* of the superlattice, effective medium techniques can be used to characterize the propagation of electrons in graphene superlattices. This theory homogenizes the granular details of the superlattice and allows for an analytical analysis of the GSL as if it was a continuous medium characterized by some effective parameters.

Similar to the homogenization techniques for metamaterials [4], this macroscopic approach is based on the spatial averaging of the high frequency spatial harmonics, so that only the spatial harmonics with the wave vector **k** within the first Brillouin zone are retained after the spatial filtering. Next, the effective medium model proposed in Ref. [15] for graphene superlattices is briefly reviewed.

V.2.1. Effective Hamiltonian

In this thesis the focus will be on 1-D graphene superlattices, such that the microscopic electrostatic potential has a step-type spatial variation, with two different values $V = V_{av} \pm V_{osc}$, as shown in Fig. 5.1.

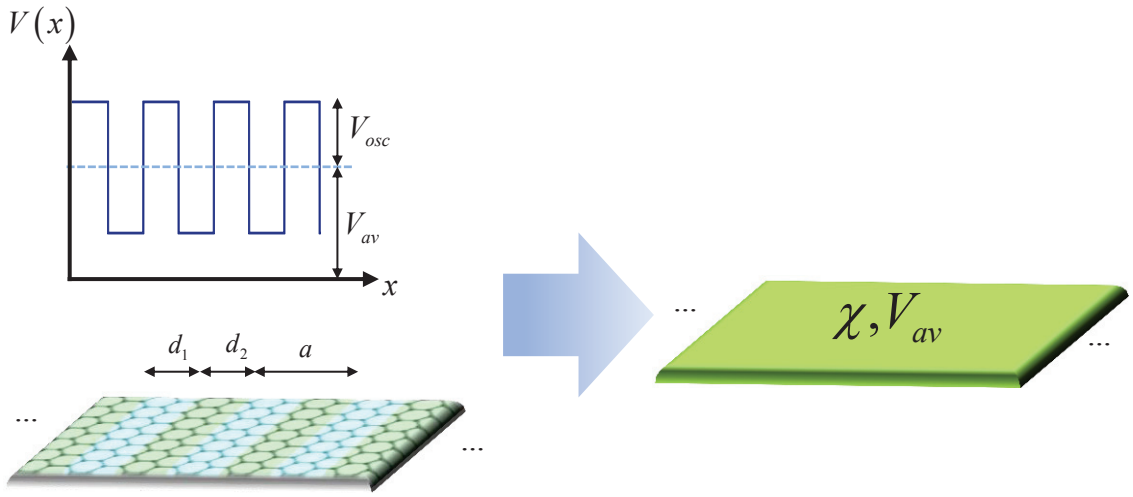

Fig. 5.1 Sketch of a graphene superlattice characterized by a step-like periodic electrostatic potential $V(x) = V_{\text{av}} + V_{\text{osc}}\ \text{sgn}\left[\sin(2\pi x/a)\right]$.

The propagation of the charge carriers with pseudo-momentum near the *K* point in the graphene superlattices is described by the massless Dirac equation:

$$\left(\hat{H}\boldsymbol{\psi}\right)(\mathbf{r}) = i\hbar\frac{\partial}{\partial t}\boldsymbol{\psi}\,, \tag{5.1}$$

where $\left(\hat{H}\boldsymbol{\psi}\right)(\mathbf{r}) = -i\hbar v_F\left(\boldsymbol{\sigma}_x\frac{d}{dx} + \boldsymbol{\sigma}_y\frac{d}{dy}\right)\boldsymbol{\psi} + V(\mathbf{r})\boldsymbol{\psi}$ is the microscopic Hamiltonian that takes into account all the granular details of the graphene material, $\boldsymbol{\psi} = \{\Psi_1, \Psi_2\}$ is a two component pseudospinor that characterizes the charge carriers, $v_F \approx 10^6\, m/s$ is the Fermi velocity and $\boldsymbol{\sigma} = \boldsymbol{\sigma}_x\hat{\mathbf{x}} + \boldsymbol{\sigma}_y\hat{\mathbf{y}}$ with $\boldsymbol{\sigma}_x$, $\boldsymbol{\sigma}_y$ the Pauli matrices. Solving this partial differential equation system allows for the complete characterization of the wave function $\boldsymbol{\psi}$. However, because of the dependence on $V(\mathbf{r})$, the microscopic Hamiltonian is strongly dependent on the granularity of the system, and typically Eq. (5.1) corresponds to a rather complex system of equations.

One way to reduce the complexity of the problem is to apply effective medium techniques to homogenize the microscopic structure. It was recently shown that the low energy states in GSLs can be characterized by an effective Hamiltonian that describes

the dynamics of the wave function envelope [15]. Within this approach, the GSL is regarded as a continuous medium characterized by some effective parameters. For an unbounded superlattice the effective Hamiltonian reads [15]:

$$\left(\hat{H}_{ef}\boldsymbol{\psi}\right)(\mathbf{r}) = \left[-i\hbar v_F \boldsymbol{\sigma}(\chi)\cdot\nabla + V_{av}\right]\cdot\boldsymbol{\psi}(\mathbf{r}), \tag{5.2}$$

where V_{av} is the average electrostatic potential, $\boldsymbol{\sigma}(\chi) = \boldsymbol{\sigma}_x\hat{\mathbf{x}} + \chi\boldsymbol{\sigma}_y\hat{\mathbf{y}}$, and χ is an effective medium parameter designated by anisotropy ratio which depends on the fluctuating part of the microscopic potential V_{osc} [15]. As thoroughly described in [J4], within this formalism $\boldsymbol{\psi}^*\cdot\boldsymbol{\psi} = |\boldsymbol{\psi}|^2$ can be regarded as a probability density function, and the time evolution of the pseudospinor $\boldsymbol{\psi}$ is determined by $i\hbar\dfrac{\partial\boldsymbol{\psi}}{\partial t} = \hat{H}_{ef}\boldsymbol{\psi}$.

The dependence of the anisotropy ratio on V_{osc} may be obtained using the techniques described in Ref. [15] and it is shown in Fig. 5.2.

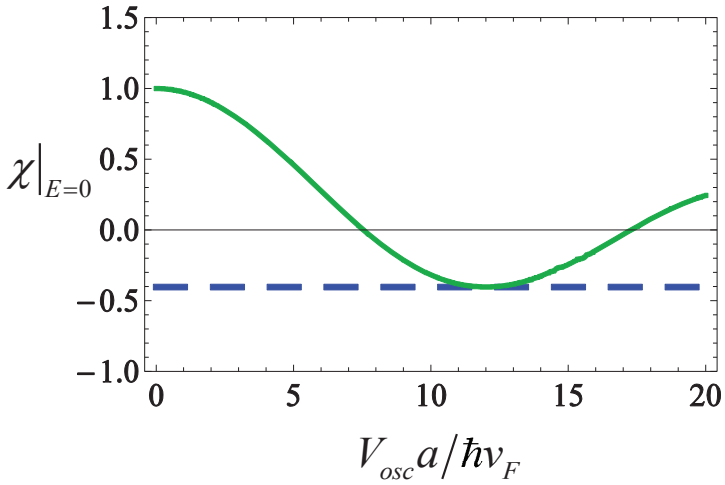

Fig. 5.2 Anisotropy ratio for an electrostatic potential $V_{\text{osc}}\,\text{sgn}\left[\sin(2\pi x/a)\right]$.

Evidently, for pristine graphene, where $V_{osc} = 0$, the anisotropy ratio is unity. However, the proper tuning of microscopic potential may allow to obtain negative values of χ, and even regimes characterized by an extreme anisotropy, where $\chi = 0$.

As seen in Fig. 5.2, for a step-like potential $V_{\text{osc}}\,\text{sgn}\left[\sin\left(2\pi x/a\right)\right]$, the anisotropy ratio may vary in the range of $\chi \approx -1/5.6$ up to $\chi = 1$ (pristine graphene).

V.2.2. Energy Dispersion of Stationary States

The stationary states energy dispersion may also be analyzed using the effective medium model introduced in Ref. [15]. For an unbounded GSL characterized by an anisotropy ratio χ and average electrostatic potential V_{av}, the dispersion relation reads [15]:

$$\left|E - V_{av}\right| = \hbar v_F \sqrt{k_x^2 + \chi^2 k_y^2}\,, \tag{5.3}$$

where E is the energy of the electrons and $\mathbf{k} = \left(k_x, k_y\right)$ is the wave vector associated with the electronic state. Importantly, it is seen that the dispersion of GSLs corresponds to a stretched Dirac cone [15]. To emphasize this, first we calculate the energy dispersion of pristine graphene ($\chi = 1.0$). The results are depicted in Fig. 5.3**(a)**, and it is seen that the energy dispersion matches the conventional Dirac cone [18].

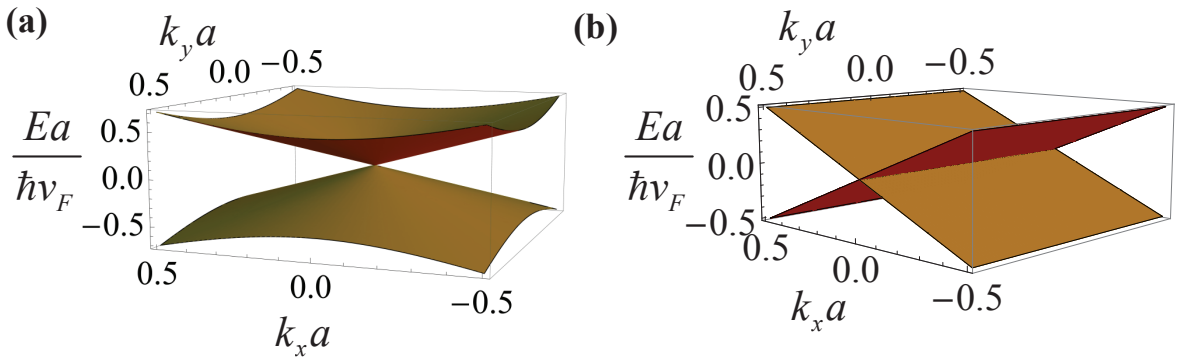

Fig. 5.3 Energy dispersion of: **(a)** Pristine graphene ($\chi = 1.0$) **(b)** Graphene superlattice in the extreme anisotropy limit ($\chi = 0$).

The dispersion of pristine graphene also reveals that electrons propagate in the pristine graphene with an isotropic velocity. This may be easily checked from the group velocity of electrons in GSLs:

$$\mathbf{v} = \nabla_k \left(E - V_{av} \right) / \hbar = v_F \frac{\left(k_x, \chi^2 k_y \right)}{\left| \mathbf{k} \right|}. \tag{5.4}$$

For pristine graphene it is seen that $\mathbf{v} = v_F \dfrac{\mathbf{k}}{|\mathbf{k}|}$. On the other hand, for an electronic state propagating in a GSL characterized by an extreme anisotropy ($\chi = 0$), the dispersion corresponds to a Dirac cone stretched along the *y*-direction, as shown in Fig. 5.3**(b)**. In fact, it is well known that GSLs may yield strongly anisotropic Dirac cones and particle velocities and, in the limit of extreme anisotropy, may allow for the propagation of electron waves with virtually no diffraction [30, 31]. This is also clear from the expression of the group velocity of electrons Eq. (5.4). For a GSL characterized by an extreme anisotropy $\left(\chi = 0 \right)$ the group velocity is equal to $\mathbf{v} = v_F \dfrac{\left(k_x, 0 \right)}{\left| \mathbf{k} \right|}$.

Importantly, the pseudospinor associated with a stationary state with energy E and wave vector $\mathbf{k}$ is of the form,

$$\boldsymbol{\psi}_{E,k_y} = \frac{e^{i\mathbf{k}\cdot\mathbf{r}}}{\sqrt{2}} \begin{pmatrix} 1 \\ s e^{i\theta_{\mathbf{q}}} \end{pmatrix}. \tag{5.5}$$

The parameter $\theta_{\mathbf{q}}$ is equal to the angle between $\mathbf{q} = \left(k_x, \chi k_y \right)$ and the *x*-axis and $s = \operatorname{sgn}\left(E - V_{av} \right)$, so that it is possible to write $s e^{i\theta_{\mathbf{q}}} = \hbar v_F \left(k_x + i\, \chi k_y \right) / \left(E - V_{av} \right)$ [15].

V.3. Validation of the Effective Medium Model

Because the effective medium formalism only applies in the long wavelength limit, the physical response of the GSL calculated with the macroscopic and microscopic theory may show some discrepancies if the spectrum of the wave function extends beyond the edge of the first Brillouin zone, or if the electronic state is more localized than the period of the microscopic potential. In this section the validity of the effective medium

will be addressed, particularly the agreement between the scattering properties of complex GSL structures, calculated with the effective medium model and with the microscopic model. In Sec. V.3.1 we introduce a formalism to solve scattering problems in GSLs. This formalism is applied in Sec. V.3.2 to investigate the validity of the effective medium theory.

V.3.1. Scattering Problems in Graphene Superlattices

To characterize the scattering properties of an incoming electron plane wave $\boldsymbol{\psi}_{E,k_y}$, with energy E and transverse quasi-momentum k_y, propagating in an a homogeneous region characterized by an anisotropy χ and electric potential V, we use a transfer matrix formalism [28]. Assuming that the spatial variation along the y-direction is of the form $e^{ik_y y}$, the transfer matrix $\mathbf{M}=\mathbf{M}\left(x,E,k_y,\chi\right)$ relates the wave function calculated at two points of space as $\boldsymbol{\psi}\left(x_0+x\right)=\mathbf{M}\cdot\boldsymbol{\psi}\left(x_0\right)$. This transfer matrix $\mathbf{M}$ satisfies [J4]:

$$\mathbf{M}=\begin{pmatrix} \cos\left(k_x x\right)+\chi k_y\dfrac{\sin\left(k_x x\right)}{k_x} & i\sqrt{k_x^2+\chi^2k_y^2}\,\dfrac{\sin\left(k_x x\right)}{s\,k_x} \\ i\sqrt{k_x^2+\chi^2k_y^2}\,\dfrac{\sin\left(k_x x\right)}{s\,k_x} & \cos\left(k_x x\right)-\chi k_y\dfrac{\sin\left(k_x x\right)}{k_x} \end{pmatrix}, \tag{5.6}$$

where $s=\mathrm{sgn}\left(E-V\right)$ and k_x is the solution of $\left|E-V\right|=\hbar v_F\sqrt{k_x^2+\chi^2k_y^2}$. The above formula generalizes the theory of [28] to materials with nontrivial anisotropy ratio ($\chi\neq 1$), and therefore can be used for both microscopic and effective medium models.

The problem under study is illustrated in Fig. 5.4 and corresponds to an electronic state propagating in pristine graphene that impinges on a cascade of l=1,…,N homogeneous regions (with $V=V_l$ in the l-th region) followed by another a pristine graphene region. From here on the energy scale is fixed so that $E=0$ corresponds to

the tip of the Dirac cone in the pristine graphene region, and therefore the electric potential is $V_{av,0}=0$ in these regions.

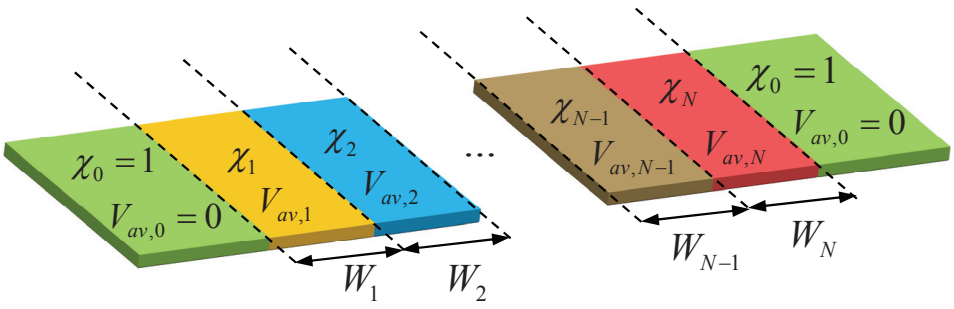

Fig. 5.4 Geometry of the cascade of l=1,…,N graphene superlattices strips (with $V=V_l$ in the l-th strip) encapsulated in a pristine graphene with an average potential offset $V_{av,0}=0$.

Within this transfer matrix formalism, the wave function at the input $(\boldsymbol{\psi}_i)$ and output $(\boldsymbol{\psi}_o)$ interfaces of the structure is related by $\boldsymbol{\psi}_o=\mathbf{M}_{glob}\cdot\boldsymbol{\psi}_i$, where $\mathbf{M}_{glob}$ is the global transfer matrix for the cascade of homogeneous regions. Using Eq. (5.5) the pseudospinor at the input and output interfaces may be written as [15]:

$$\boldsymbol{\psi}_i=\begin{pmatrix}1\\ s_i\dfrac{k_{x,i}+ik_y}{\sqrt{k_{x,i}^2+k_y^2}}\end{pmatrix}+R\begin{pmatrix}1\\ s_i\dfrac{-k_{x,i}+ik_y}{\sqrt{k_{x,i}^2+k_y^2}}\end{pmatrix}, \tag{5.7}$$

$$\boldsymbol{\psi}_o=\begin{pmatrix}1\\ s_i\dfrac{k_{x,i}+ik_y}{\sqrt{k_{x,i}^2+k_y^2}}\end{pmatrix}, \tag{5.8}$$

where T and R are the transmission and reflection coefficients, $k_{x,i}$ is the x-propagation constant of the incident wave and $s_i=\mathrm{sgn}(E)$. Considering that that wave function at the input and output interfaces is related by $\boldsymbol{\psi}_o=\mathbf{M}_{glob}\cdot\boldsymbol{\psi}_i$, the values of the coefficients T and R maybe simply obtained from the solution of the linear system:

$$\mathbf{M}_{glob}\cdot\boldsymbol{\psi}^+ + R\,\mathbf{M}_{glob}\cdot\boldsymbol{\psi}^- = T\boldsymbol{\psi}^+, \tag{5.9}$$

where $\boldsymbol{\psi}^{\pm} = \left(1 \quad s_i\left(\pm k_{x,i} + i\,k_y\right)/\sqrt{k_{x,i}^2 + k_y^2}\right)^T$.

The calculation of $\mathbf{M}_{glob}$ for the microscopic structure, where all the granular details of the superlattice are taken into account, is discussed next. Due to the step-like modulation of the microscopic potential on the surface of pristine graphene, each period of a superlattice may be regarded as two homogeneous regions with anisotropy ratio $\chi = 1$, thickness $a/2$ and electric potentials $V = V_{av} \pm V_{osc}$, respectively. Thus, the microscopic structure may be regarded as a cascade of *l*=1,…,*N* homogeneous regions (with $V = V_l$ in the *l*-th region), which is similar to the effective medium approach discussed below the difference being that in the microscopic model $\chi = 1$ in all space and the total number of regions is obviously larger. Since in pristine graphene the pseudospinor is continuous across the interfaces, it can be easily checked that the global transfer matrix is $\mathbf{M}_{glob} = \prod_{l=1}^{N} \mathbf{M}_l\left(d_l, V_l\right)$, where $d_l = a/2$ is the thickness of the *l*-th slab.

Under an effective medium model approach, there are *l*=1,…, N' homogeneous regions characterized by $V = V_l$ and $\chi = \chi_l$ in the *l*-th region, as shown in Fig. 5.4. Therefore one might expect that the global transfer matrix should simply be an extension of the previous result such that $\mathbf{M}_{glob} = \prod_{l=1}^{N'} \mathbf{M}_l\left(d_l, V_l, \chi_l\right)$, with $\mathbf{M}_l\left(d_l, V_l, \chi_l\right)$ the transfer matrix of each region, which depends on the average potential offsets V_l, anisotropy ratio χ_l and thickness d_l of each superlattice. However, it was shown in [J4] that this hypothesis leads to unsatisfactory results. The reason behind this conclusion is that within the macroscopic approach there is no compelling physical reason to enforce the continuity of the wave function at an interface between distinct

superlattices, as it was considered in the microscopic model. The crucial requirement is that the probability current density j_x is continuous at the interfaces normal to the *x*-direction. The probability current density is equal to $j_x = v_F \boldsymbol{\psi}^* \cdot \boldsymbol{\sigma}_x \cdot \boldsymbol{\psi}$ [J4], and its continuity is evidently guaranteed by the continuity of $\boldsymbol{\psi}$. Nevertheless, this is not the only possibility. In fact, it can be checked that a generalized boundary condition of the type $\left\lfloor \mathbf{U}(\chi) \cdot \boldsymbol{\psi} \right\rfloor_{x=x_0} = 0$, where the operator $\left\lfloor \ \right\rfloor_{x=x_0}$ is defined in the same manner as in Sec. II.2.2, is compatible with the continuity of j_x at an interface $x = x_0$. In this notation $\mathbf{U}_{x_0^{\pm}}$ are linear operators that depend on the effective media, and the boundary condition is valid provided the operators $\mathbf{U}$ are such that $\mathbf{U}^{-1,\dagger} \cdot \boldsymbol{\sigma}_x \cdot \mathbf{U}^{-1}$ is the same for all media. Since for pristine graphene $\mathbf{U}$ must be taken equal to the identity matrix, the validity of this boundary condition also requires that $\mathbf{U}^{-1,\dagger} \cdot \boldsymbol{\sigma}_x \cdot \mathbf{U}^{-1} = \boldsymbol{\sigma}_x$. All these conditions can be satisfied if $\mathbf{U}$ commutes with $\boldsymbol{\sigma}_x$ and is unitary. Any $\mathbf{U}$ of the form

$$\mathbf{U} = e^{iu\boldsymbol{\sigma}_x} = \begin{pmatrix} \cos u & i\sin u \\ i\sin u & \cos u \end{pmatrix}, \tag{5.10}$$

with *u* real valued, satisfies these restrictions. The parameter *u* depends on the effective medium parameters (χ) and for pristine graphene should be taken equal to zero. A numerical fitting of the microscopic and macroscopic model results showed that $u(\chi) = c_1 \arccos\left(1 + c_2(\chi - 1)\right)$, with $c_1 = 0.689$ and $c_2 = 1.650$, may accurately model the wave scattering at the interfaces (see [J4] for more details) between distinct superlattices.

In summary, contrasting with the microscopic model where the continuity of the wave function at the interfaces of homogeneous regions is required, within the effective medium approach a nontrivial boundary condition of the type $\left\lfloor \mathbf{U}(\chi) \cdot \boldsymbol{\psi} \right\rfloor_{x=x_0} = 0$ must

be considered. By including this boundary condition in the calculation of the global transfer matrix, it can be easily checked that the global transfer matrix of the cascade of homogenized superlattices is equal to $\mathbf{M}_{glob} = \prod_{l=1}^{N'} \mathbf{U}(\chi_l) \cdot \mathbf{M}_l(d_l, V, \chi_l) . \mathbf{U}^{-1}(\chi_l)$.

V.3.2. Numerical Results

To begin with, the formalism described in the previous subsection will be used to calculate the scattering properties of an electronic wave with energy $E_0 a/\hbar v_F = 0.1$, which for a lattice period $a = 10\text{nm}$, which will be fixed from here on, corresponds to $E_0 \approx 6.6\text{meV}$, propagating in pristine graphene and that impinges in a cascade of two superlattices. The GSLs are characterized by the same anisotropy ratio $\chi_1 = \chi_2 = \chi = 0.4$ and thickness $W_1 = W_2 = 20a$, but have distinct average potential offsets so that $V_{1,\text{av}} a/\hbar v_F = -0.25$ and $V_{2,\text{av}} a/\hbar v_F = 0.25$, which for the considered lattice period correspond to $V_{1,2,\text{av}} \approx \mp 16.6\text{meV}$. Using the methods described in Ref. [15] it can be checked that these anisotropy ratios correspond to microscopic potentials with $V_{\text{osc}} a/\hbar v_F \approx 4.25$ ($V_{\text{osc}} \approx 0.28\,\text{eV}$). The coefficients R and T are calculated for $E = E_0$ as a function of k_y. For a fixed value of the energy of the electron waves E_0, the value of k_y determines the incidence angle. In fact, it can be easily checked that $k_y = 0$ corresponds to normal incidence, and since $k_{y,\text{e}} = E_0/\hbar v_F$ corresponds to grazing incidence, all values of k_y larger than $k_{y,\text{e}}$ originate a k_x that is purely imaginary, resulting in non-normalizable complex electronic states. This is the electronic analog of the evanescent electromagnetic waves. The scattering properties of the structure are depicted in Fig. 5.5, and reveal a remarkable agreement between the microscopic theory (discrete symbols) and effective medium model (thick solid lines) results, particularly in

the range of $k_{y,\max}a < 1.2$. These results validate the effective medium theory for electron wave propagation in GSLs, proving that the superlattices may be indeed be regarded as a continuous medium characterized by some effective parameters.

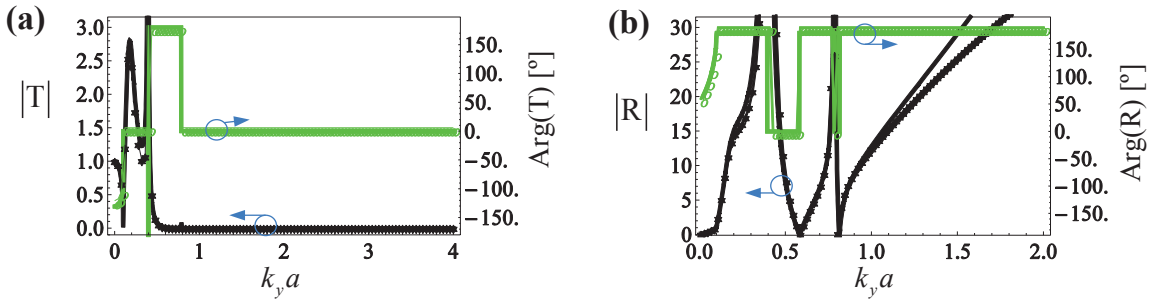

Fig. 5.5 Amplitude and phase of the **(a)** transmission and **(b)** reflection coefficients for an electron plane wave that travels in pristine graphene with energy $E_0 a/\hbar v_F = 0.1$ and impinges on a cascade of two GSL slabs characterized by equal thicknesses $W_2 = W_1 = 20a$ and anisotropy ratios $\chi = \chi_1 = \chi_2 = 0.4$ (in the microscopic model $V_{\text{osc}} a/\hbar v_F \approx 4.25$), but with different average potential offsets $V_{1,2,\text{av}} a/\hbar v_F = \mp 0.25$. The discrete symbols (joined by thin lines) correspond to the results calculated using the microscopic model whereas the solid thick curves correspond to the effective medium model results.

Remarkably, since the value $k_{y,\max}$ is about twelve times larger than $k_{y,\text{e}}$, the validity of the effective medium model extends well beyond the spectrum of the propagating electronic states. Moreover, for some values of $k_y > k_{y,\text{e}}$ the amplitude of the transmission coefficient T is larger than one, particularly in the range of $k_{y,\text{e}} < k_y < 0.75/a$, suggesting that there is some amplification of part of the evanescent electronic states spectrum. As shown in Ref. [15, 35], the exponential amplification of complex electronic states in GSLs may allow to compensate for the exponential decay in the outside regions of the GSL slab, and thus obtain the electronic analog of the Pendry lens [40].

As a second example, we characterize the scattering properties of a cascade of four distinct GSLs encapsulated in pristine graphene. The first two superlattices are very similar to the ones considered in the previous example and are characterized by the following parameters: anisotropy ratio $\chi_1 = \chi_2 = 0.4$, thickness $W_1 = W_2 = 20a$, and

average potential offsets $\left(V_{1,\mathrm{av}}-E_0\right)a/\hbar v_F=-0.25$ and $\left(V_{2,\mathrm{av}}-E_0\right)a/\hbar v_F=0.25$, for an electronic state with energy $E_0a/\hbar v_F=1.0$. The anisotropy ratio of the third superlattice is $\chi_3=0.3$ (in the microscopic model $V_{\mathrm{osc},3}a/\hbar v_F\approx 5.19$), while its thickness is $W_3=10a$ and the average potential offset is $\left(V_{3,\mathrm{av}}-E_0\right)a/\hbar v_F=0.2$. Finally the last superlattice is characterized by an average potential offset $\left(V_{4,\mathrm{av}}-E_0\right)a/\hbar v_F=0.125$, thickness $W_4=6a$ and an anisotropy ratio $\chi_4=0.1$, which in the microscopic theory corresponds to a oscillating potential with amplitude $V_{\mathrm{osc},4}a/\hbar v_F\approx 5.71$. The scattering properties of this structure are shown in Fig. 5.6.

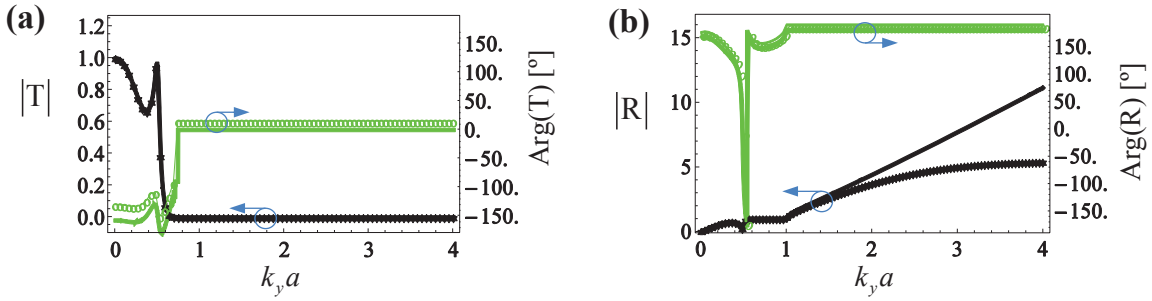

Fig. 5.6 Amplitude and phase of the **(a)** transmission and **(b)** reflection coefficients for an electron plane wave that travels in pristine graphene with energy $E_0a/\hbar v_F=1.0$ and impinges on a cascade of four GSL slabs. The first two are characterized by equal thicknesses $W_2=W_1=20a$ and anisotropy ratios $\chi_1=\chi_2=0.4$, but with different average potential offsets $\left(V_{1,2,\mathrm{av}}-E_0\right)a/\hbar v_F=\mp 0.25$. The third superlattice has a thickness $W_3=10a$, anisotropy ratio $\chi_3=0.3$ (in the microscopic model $V_{\mathrm{osc},3}a/\hbar v_F\approx 5.19$) and average potential offset $\left(V_{3,\mathrm{av}}-E_0\right)a/\hbar v_F=0.2$. Finally the last superlattice is characterized by an average potential offset $\left(V_{4,\mathrm{av}}-E_0\right)a/\hbar v_F=0.125$, thickness $W_4=6a$ and an anisotropy ratio $\chi_4=0.1$, which in the microscopic theory corresponds to a oscillating potential with amplitude $V_{\mathrm{osc},4}a/\hbar v_F\approx 5.71$. The discrete symbols (joined by thin lines) correspond to the results calculated using the microscopic model whereas the solid thick curves correspond to the effective medium model results.

Clearly, even for this more complex heterostructure the agreement between the results of the macroscopic and the microscopic theories is still very good. This demonstrates in a conclusive manner the validity of effective medium model for electron wave propagation in graphene superlattices.

V.4. Negative Refraction of Electron Waves

The negative refraction of photons using DNG media was first proposed by Victor Veselago in 1968 [5]. In his pioneering work, Veselago theoretically demonstrated that DNG media might allow for negative refraction, so that a light beam impinging at an interface between a conventional material and a DNG material obeys a reversed Snell's law, as illustrated in Fig. 5.7. In this section the concept of negative refraction of light in metamaterials [41,42] will be extended to the electron wave propagation in graphene based nanomaterials. The conditions required for this phenomenon to be observed at the heterojunctions between distinct GSLs will be analyzed, and some numerical examples will illustrate this phenomenon. The analysis relies on the effective medium model introduced in Sec. V.2.

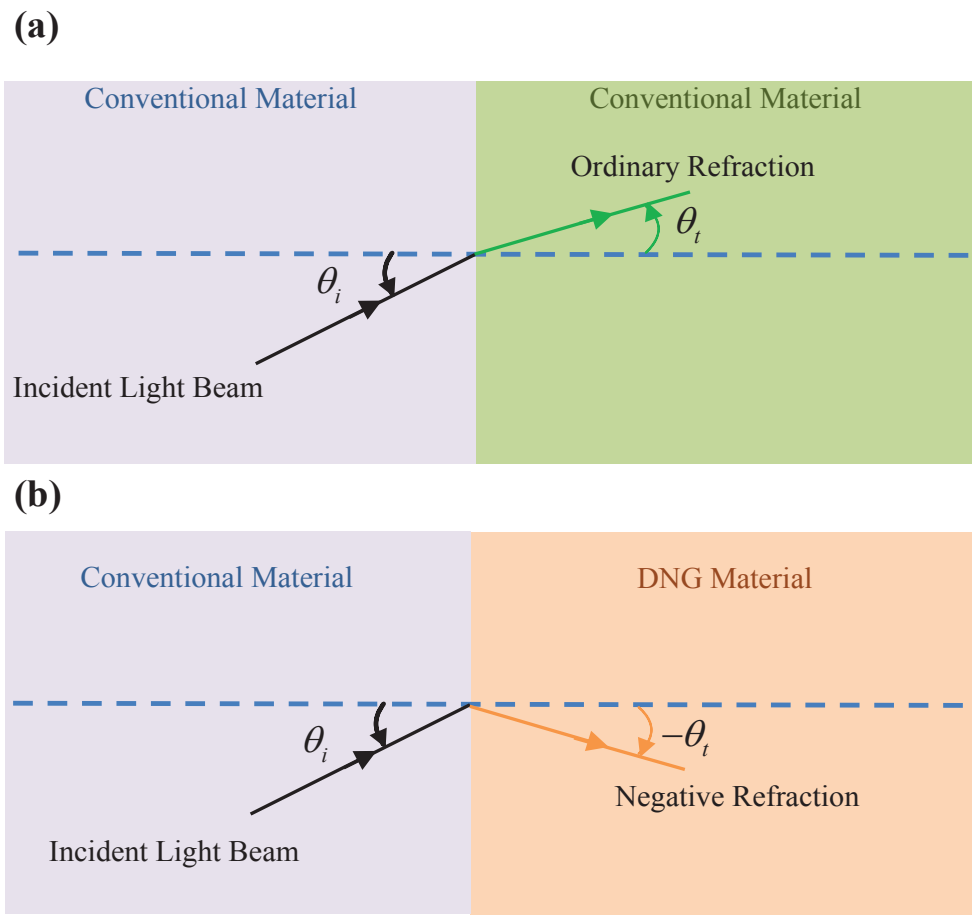

Fig. 5.7 Graphic representation of: **(a)** a light beam propagating in a conventional material experiencing ordinary refraction, **(b)** a light beam propagating in a conventional material being negatively refracted at the interface with a DNG material.

First, we define the propagation angle θ_P of an electron plane wave in a graphene superlattice. The angle θ_P is measured between the direction of the group velocity and the direction normal to the interface (*x*-direction). From Eq. (5.4), the propagation angle of electron waves in graphene superlattices may be written as:

$$\theta_P = \tan^{-1}\left(v_y / v_x\right) = \tan^{-1}\left(\chi^2 k_y / k_x\right). \tag{5.11}$$

Using equation (5.3), the longitudinal component of the pseudo-momentum k_x may be written as a function of the energy of the electrons E_0 and transverse component of the pseudo-momentum k_y, and is equal to:

$$k_x = \mathrm{sgn}\left(E_0 - V_{av}\right)\sqrt{\left(\frac{\left(E_0 - V_{av}\right)}{\hbar v_F}\right)^2 - \chi^2 k_y^2}\ . \tag{5.12}$$

Therefore, substituting this result into Eq. (5.11), it is seen that variations in the average potential of the superlattice can severely affect θ_P:

$$\theta_P = \tan^{-1}\left(\frac{\chi^2 k_y}{\mathrm{sgn}\left(E_0 - V_{av}\right)\sqrt{\left(\left(E_0 - V_{av}\right)/\hbar v_F\right)^2 - \chi^2 k_y^2}}\right). \tag{5.13}$$

In fact, it was recently proposed that electron waves may be negatively refracted at the heterojunction between two superlattices with properly chosen average potential offsets [15]. This can be easily explained using the developed formalism. For a fixed value of k_y and E_0, if the term $E_0 - V_{av}$ has opposite signs in the two regions, then from Eq. (5.12) the value of k_x is also symmetric, and therefore propagation angle θ_P will flip its sign. Thus, the negative refraction of electron waves may occur at the interface between two superlattices with $E_0 - V_{av}$ with opposite signs.

To illustrate these ideas first we consider a pristine graphene ($\chi = 1$) heterojunction with the following electric potential distribution:

$$V(x)=\begin{cases}0 & x<0\\ 2E_0, & x>0\end{cases}, \tag{5.14}$$

so that in both regions the relation $E_0 - V$ has the same amplitude but has opposite signs. It can be checked that in these conditions an electron wave propagating in the $x<0$ region with a fixed incidence angle is refracted at the heterojunction $x=0$ with an angle symmetric to the incidence angle.

We consider the scenario wherein a Gaussian electron wave propagates in the $x<0$ region. The Gaussian beam is taken equal to:

$$\boldsymbol{\psi}^{inc}(x,y)=\int_{-\infty}^{+\infty}\boldsymbol{\psi}_{E_0,k_y}(x-x_i,y)e^{-\left(k_y-k_{y,0}\right)R_G^2/4}dk_y\,, \tag{5.15}$$

where $\boldsymbol{\psi}_{E_0,k_y}$ is the pseudospinor distribution for a plane wave stationary state with fixed energy $E=E_0$ and the pseudo-momentum $k_{y,0}$. The parameter R_G can be regarded as the beamwidth at the reference plane $x_i=-25a$, which is taken coincident with the input plane. The probability density distribution $|\boldsymbol{\psi}|^2$ in all space is calculated for a Gaussian electron wave with beamwidth $R_G=10a$, energy $E_0a/\hbar v_F=\sqrt{2}$ and pseudo-momentum $k_{y,0}a=1.0$, so that the propagation angle of the incident beam is $\theta_{p,i}=45^{\circ}$.

The pseudospinor distribution for a plane wave stationary state $\boldsymbol{\psi}_{E_0,k_y}$ is calculated using the transfer matrix formalism described in Sec. V.3.1. First, the scattering coefficients are calculated using Eq. (5.9). Next, these parameters are used in Eqs. (5.5), (5.7) and (5.8) to obtain the spatial distribution of pseudospinor for a plane wave stationary state. The distribution of the pseudospinor is then used in Eq. (5.15) to calculate the Fourier integral and obtain the value of the wave function in all space. The spatial distribution of the wave function for the considered structure is shown in Fig.

5.8**(a)**, and reveals that the transmission angle is symmetric to the incidence angle, i.e. $\theta_{p,t} = -\theta_{p,i} = -45^{\circ}$, confirming in this manner that the Gaussian electron wave experiences a negative refraction at the heterojunction $x = 0$.

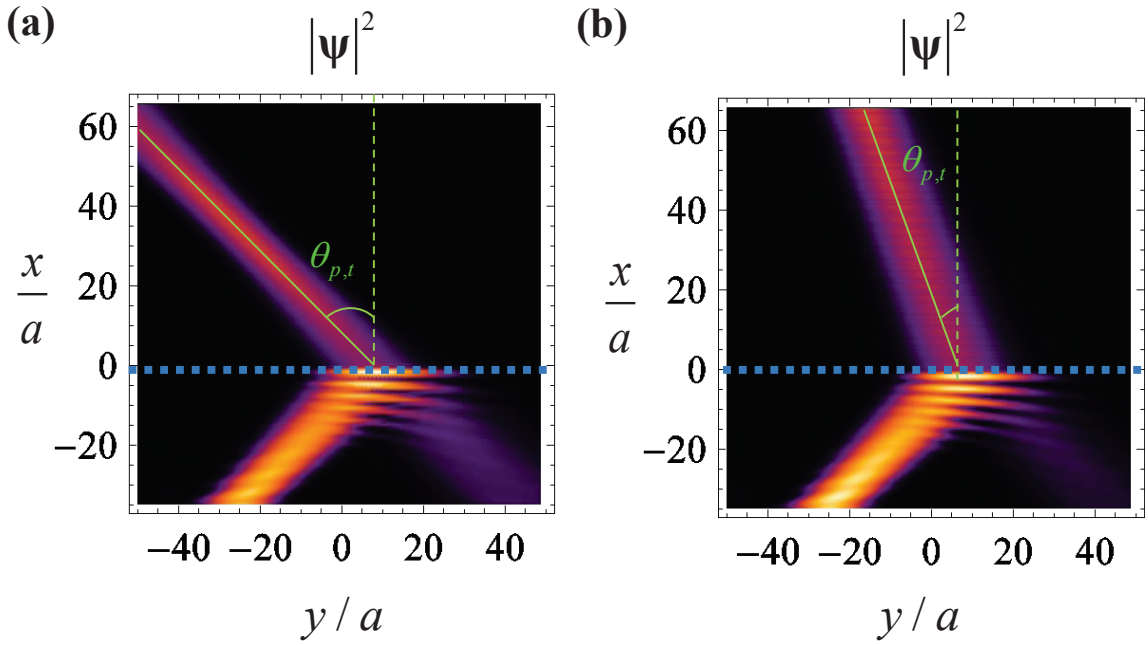

Fig. 5.8 Density plots of $|\psi|^2$ calculated for an incident Gaussian electron wave with $R_G = 10a$, $E_0 a/\hbar v_F = \sqrt{2}$ and pseudo-momentum $k_{y,0}a = 1.0$, propagating in pristine graphene $(x < 0)$ with potential $V_0 = 0$, that impinges on another pristine graphene region with electrtic potential **(a)** $V = 2E_0$ and **(b)** $V = 3E_0$.

It is curious to see that Eq. (5.13) predicts that as the electric potential increases, the transmitted electron waves tend to propagate in a direction closer to the normal to the interface. This is illustrated in Fig. 5.8**(b)**, which shows the probability density distribution $|\psi|^2$ in all space when the electric potential of the second superlattice is increased from $V = 2E_0$ to $V = 3E_0$, maintaining the remaining of the structural parameters as in the previous example.

Since the term $E_0 - V$ has opposite signs in two regions, the Gaussian electron wave is still negatively refracted at the interface. However, comparing these results with ones

depicted in Fig. 5.8**(a)**, it is seen that the refracted angle is smaller, and now it is equal to $\theta_{p,t} \approx -20.7^{\circ}$.

To demonstrate that the negative refraction of electron waves occurs at interfaces of graphene superlattices, next we calculate the probability density $|\psi|^2$ for a structure consisting of a GSL slab encapsulated in pristine graphene, similar to what is shown in Fig. 5.4. The superlattice is characterized by an anisotropy ratio $\chi = -1/5.6$ ($V_{\text{osc}} a/\hbar v_F \approx 7.83$), thickness $W = 20a$ and an electric potential $(E_0 - V)a/\hbar v_F = -1.6$, for a Gaussian electron wave with energy $E_0 a/\hbar v_F = \sqrt{2}$, pseudo-momentum $k_{y,0} a = 1.0$ and beamwidth $R_G = 1.0a$. The spatial distribution of the probability density distribution was calculated using the microscopic ($|\psi_{mic}|^2$) and macroscopic models ($|\psi_{ef}|^2$), and the results are shown in Fig. 5.9. Since the microscopic wave function ψ_{mic} has strong fluctuations on the scale of the period of the superlattices, the plots represent the spatially averaged probability density function $|\psi_{mic}|^2_{av}(x,y) = \frac{1}{a}\int_{-a/2}^{a/2} |\psi_{mic}(x+x',y)|^2 \, dx'$, where these spatial oscillations are filtered.

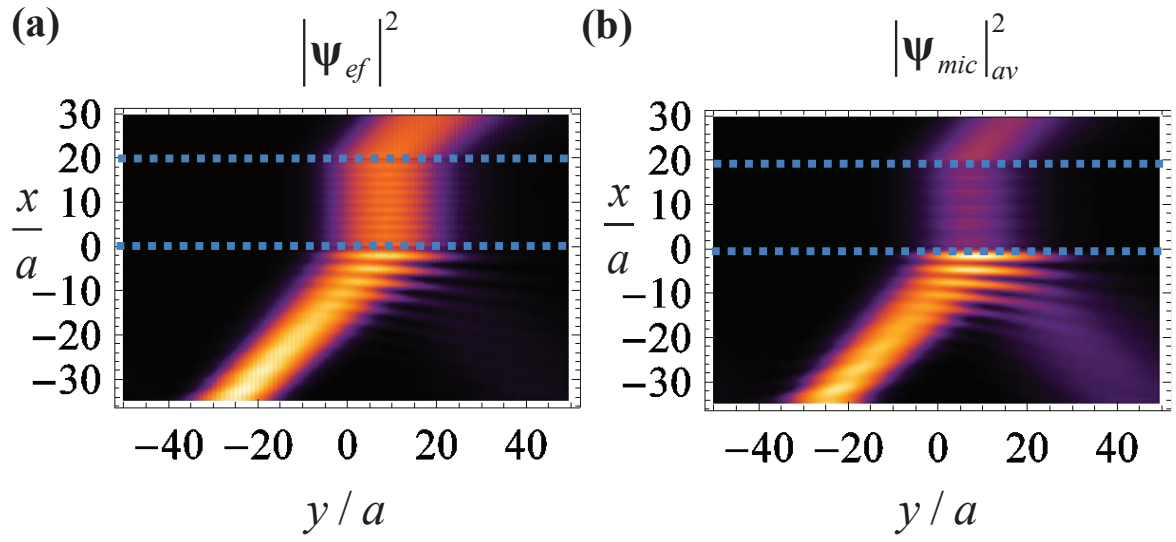

Fig. 5.9 (a) Density plot of $|\psi|^2$ calculated with the effective medium model with for an incident Gaussian electron wave with $R_G = 10a$, $E_0 a/\hbar v_F = \sqrt{2}$ and pseudo-momentum $k_{y,0}a = 1.0$, that impinges on a GSL slab encapsulated in a pristine graphene with an average potential offset $V_0 = 0$. The GSL is characterized by an anisotropy ratio $\chi = -1/5.6$, thickness $W = 20a$ and an electric potential $(E_0 - V)a/\hbar v_F = -1.6$. **(b)** Similar to **(a)** but calculated with the exact microscopic theory, where the superlattice is characterized by a step-like potential with amplitude $V_{\text{osc}} a/\hbar v_F \approx 7.83$.

Remarkably, the results of effective medium model show a good agreement with the microscopic theory, and both theories confirm that the electron beam is negatively refracted at the interfaces of the slab. From both Eq. (5.13) and the results depicted in Fig. 5.9, it can be checked that the propagation angle of the refracted beam in the graphene superlattice is $\theta_{p,SL} \approx -1.2°$, which means that the beam experiences a negative refraction at both interfaces of the slab. It is also interesting to note that while for pristine graphene an average potential offset equal to $(E_0 - V)a/\hbar v_F = -1.6$ and a pseudo-momentum $k_{y,0}a = 1.0$ would generate a propagation angle of $\theta_p \approx -39°$, the corresponding angle in the superlattice is much smaller, confirming that the group velocity in superlattices may be strongly anisotropic.

V.5. Wormhole for electron waves in graphene superlattices

It was recently suggested in Ref. [15, 35] that in some conditions two superlattice materials with complementary properties may behave as some form of "matter-antimatter", annihilating one another from an electronic point of view. As discussed in Sec. V.1, this effect mimics the properties of a "wormhole" that connects two regions of space, as if the region in between was nonexistent. Motivated by these analogies, in this section we study the possibility of obtaining a wormhole for electron waves using a cascade of graphene superlattices encapsulated in pristine graphene, as shown in Fig. 5.4.

It is important to stress that the desired response is rather different from the Klein tunneling phenomenon [18-20], where a single potential barrier ensures the complete transmission of an electron wave for normal incidence, but for wide incidence angles the electron waves are typically strongly scattered. The work described in this section intends to extend in a nontrivial manner the Klein tunneling to electron waves with wide incidence angles, including grazing incidence and evanescent waves.

In the work reported in Refs. [15, 35], it was predicted that two GSLs with symmetric anisotropy ratios $\chi_1 = -\chi_2$ and equal x-widths $W_1 = W_2$ are dual, in the sense that for electron waves with an energy level $E_0 = \left(V_{1,\mathrm{av}} + V_{2,\mathrm{av}}\right)/2$, the superlattices have no effect on the wave propagation (see Fig 5.10), so that any incoming electronic wave packet is tunneled through the paired GSLs as if they were absent.

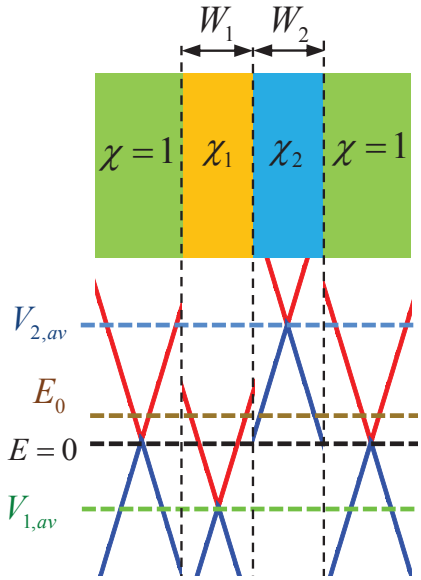

Fig. 5.10 Geometry of two dual graphene superlattices slabs encapsulated in pristine graphene and the energy diagram associated with each material.

To demonstrate this idea, we consider two dual superlattices with anisotropy ratios $\chi_1 = -1/5.6$ and $\chi_2 = -\chi_1$, which in the microscopic theory correspond to oscillating potentials with amplitude with $V_{1,\mathrm{osc}} a/\hbar v_F \approx 7.83$ and $V_{2,\mathrm{osc}} a/\hbar v_F \approx 5.30$ ($V_{1,\mathrm{osc}} \approx 0.52\,\mathrm{eV}$ and $V_{2,\mathrm{osc}} \approx 0.35\,\mathrm{eV}$). It is supposed that the two superlattices have finite widths $W_1 = W_2 = 20a$ and are encapsulated in pristine graphene, as shown in Fig 5.10. The average potential offsets in the superlattices are taken equal to $\left(V_{1,\mathrm{av}} - E_0\right) a/\hbar v_F = -0.5$ and $\left(V_{2,\mathrm{av}} - E_0\right) a/\hbar v_F = 0.5$, and the energy level wherein the perfect transmission is supposed to occur is set to $E_0 a/\hbar v_F = 0.3$. Similarly to what was considered in Sec. V.3, the energy scale is fixed so that $E = 0$ corresponds to the tip of the Dirac cone in pristine graphene. Using the techniques described in Sec. V.3.1, we characterized the scattering of an incoming electron plane wave as a function of k_y. The calculated *R* and *T* for both the microscopic theory (discrete symbols) and effective medium model (thick solid lines), are shown in Fig. 5.11.

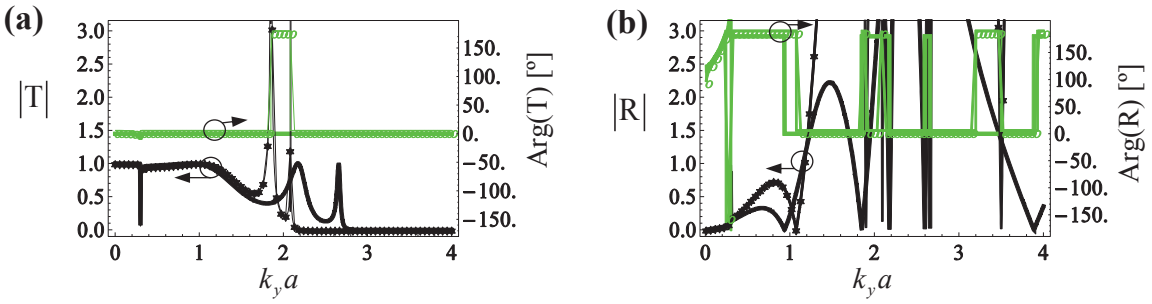

Fig. 5.11 Amplitude and phase of the **(a)** transmission and **(b)** reflection coefficients for an electron plane wave that travels in pristine graphene with energy $E_0 a/\hbar v_F = 0.3$ and impinges on a slab of two dual GSLs with total thickness $W = 40a$, with $\chi_{1,2} = \mp 1/5.6$ and an average potential offset $\left(V_{1,2,\mathrm{av}} - E_0\right) a/\hbar v_F = \mp 0.5$.

The results reveal a good agreement between the microscopic and the effective medium models, especially for incident waves with $\left|k_y\right| < k_{y,\max}$, where $k_{y,\max} a \approx 1.1$ is the pseudo momentum value for which the transmission coefficient satisfies to an excellent approximation $T \approx 1$, i.e. the amplitude is near unity and the phase is near to zero degrees. Hence, the paired GSLs can indeed bridge the input and output interfaces of the structure behaving as a wormhole tunnel for electron waves, and the parameter $k_{y,\max}$ may be regarded as the breaking point in the validity of the effective medium model. Note that that spectral region $\left|k_y\right| < k_{y,\max}$ includes all the propagating states in pristine graphene at $E = E_0$. In fact, for the considered structure $k_{y,\mathrm{e}} a = 0.3$ corresponds to grazing incidence, and thus $k_{y,\max} \approx 3.67 k_{y,\mathrm{e}}$. The performance of the paired GSLs is less satisfactory from the reflection point of view, because R is near zero only for $\left|k_y\right| < 0.4/a$.

It must be emphasized that the combined effect of the two superlattices is essential to short-circuit the input and output interfaces and have the graphene wormhole. To demonstrate this, we studied the individual response of each superlattice. The calculated

amplitude and phase of the transmission coefficient for each superlattice is depicted in Fig. 5.12.

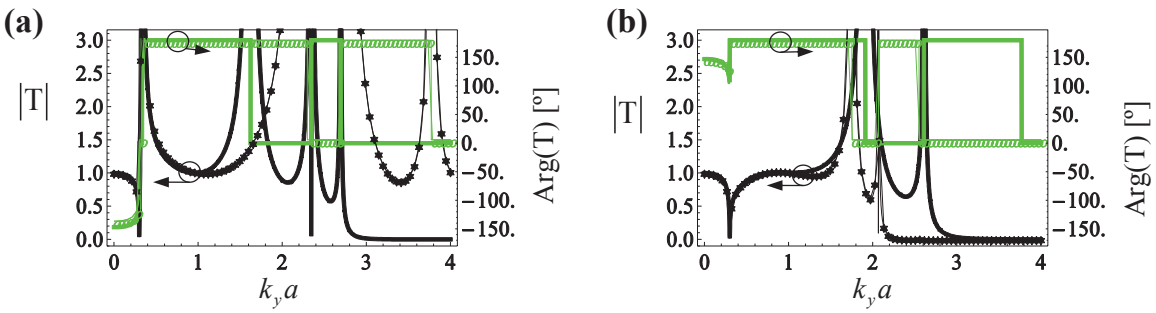

Fig. 5.12 Amplitude and phase of the transmission coefficient for an electron plane wave that travels in pristine graphene with energy $E_0 a/\hbar v_F = 0.3$ and impinges on a slab of: **(a)** a GSL with thickness $W = 20a$, anisotropy ratio $\chi_1 = -1/5.6$ and an average potential offset $\left(V_{1,\mathrm{av}} - E_0\right)a/\hbar v_F = -0.5$; **(b)** a GSL with thickness $W = 20a$, anisotropy ratio $\chi_2 = 1/5.6$ and an average potential offset $\left(V_{2,\mathrm{av}} - E_0\right)a/\hbar v_F = +0.5$.

Clearly, if each superlattice is taken separately, the transmission coefficient is completely different from $T \approx 1$ and therefore the wormhole phenomenon disappears. Curiously, it is seen that the agreement between the microscopic and the effective medium results is within the same range of incidence angles as in Fig. 5.11**(a)**.

It should be noted that even when both superlattices are taken together there the transmission coefficient is not unity for all values of k_y (see Fig. 5.11), and therefore the structure does not behave as an ideal wormhole for all incidence angles. In fact, it can be checked that within the effective medium framework with the nontrivial boundary condition, the requirements for perfect transmission are met only when $u(\chi_1) = u(\chi_2)$. This condition is exactly satisfied only when the paired superlattices are characterized by anisotropy ratios $\chi_1 = -\chi_2 = 0$. In this scenario, the paired superlattices mimic perfectly a wormhole within the effective medium model, with $T = 1$ and $R = 0$ for all the incoming waves with energy E_0. In Fig. 5.13, we depict T and R for a design where

$\chi_1 = -\chi_2 = 0$ (which corresponds to $V_{\text{osc},1} = V_{\text{osc},2} \approx 6.28\hbar v_F / a \approx 0.42\,\text{eV}$ in the microscopic model) and average potential offsets $\left(V_{1,2,\text{av}} - E_0\right) a / \hbar v_F = \mp 0.5$.

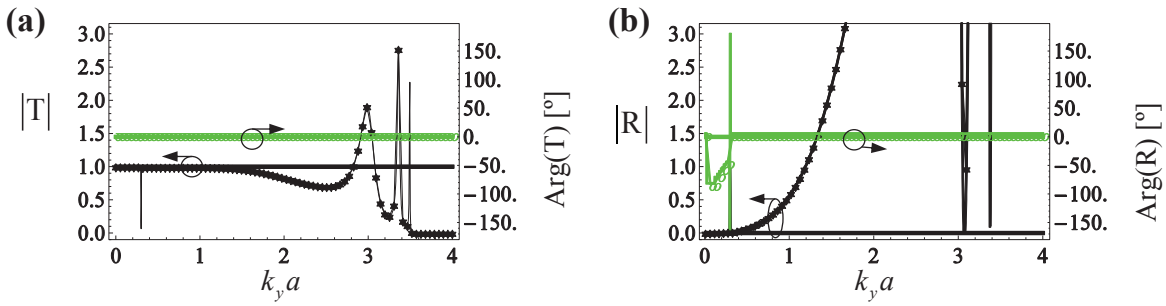

Fig. 5.13 Amplitude and phase of the **(a)** transmission and **(b)** reflection coefficients for an electron plane wave that travels in pristine graphene with energy $E_0 a / \hbar v_F = 0.3$ and impinges on a slab of two dual GSLs with total thickness $W = 40a$, with $\chi_1 = \chi_2 = 0$ (which corresponds to $V_{\text{osc},1} = V_{\text{osc},2} \approx 6.28\hbar v_F / a \approx 0.42\,\text{eV}$ in the microscopic model) and average potential offsets $\left(V_{1,2,\text{av}} - E_0\right) a / \hbar v_F = \mp 0.5$.

Interestingly, in the example of Fig. 5.13 the agreement between the microscopic and macroscopic theories extends to $k_{y,\max} a \approx 1.2$ in terms of having perfect transmission. Similar to the first design, the performance for the reflection coefficient is less satisfactory, since *R* is near zero only for $|k_y| < 0.35 / a$.

As discussed in Sec. V.2.2, superlattices in the extreme anisotropy limit may allow for an electron wave to be supercollimated along the direction of propagation with virtually no diffraction. To illustrate this phenomenon we calculated the probability density distribution $|\psi|^2$ for the structure considered in Fig. 5.13. The energy of the electrons was set to $E_0 a / \hbar v_F = 0.025$ and the electric potentials changed to $\left(V_{1,2,\text{av}} - E_0\right) a / \hbar v_F = \mp 0.1$. The probability density distribution $|\psi|^2$ was calculated using both the microscopic ($|\psi_{mic}|^2$) and macroscopic models ($|\psi_{ef}|^2$), and the results are shown in in Fig. 5.14.

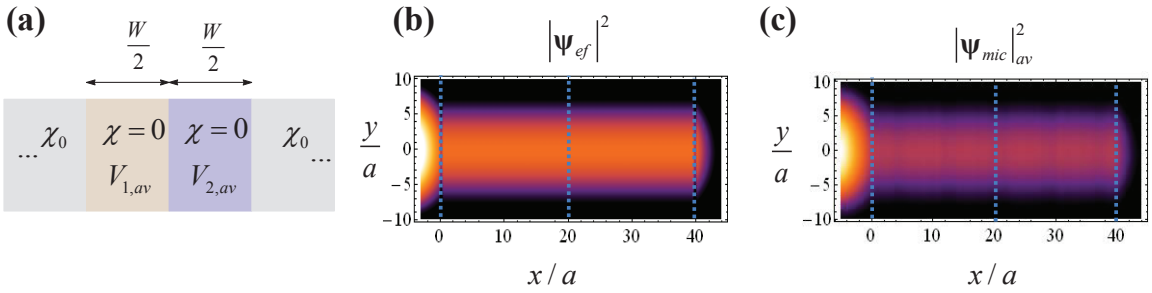

Fig. 5.14 (a) Geometry of the GSL slab embedded in pristine graphene ($\chi_0 = 1$). **(b)** Density plots of $|\psi|^2$ (in a logarithmic scale) calculated with the effective medium theory for an incident Gaussian electron wave with $R_G = 2.86a$. **(c)** Similar to **(b)** but calculated with the exact microscopic theory. In all the examples, $E_0 a/\hbar v_F = 0.025$, and the GSLs are characterized by $\chi = 0$ and $\left(V_{1,2,\mathrm{av}} - E_0\right) a/\hbar v_F = \mp 0.1$.

The results depicted in Fig. 5.14 reveal that the Gaussian electron wave experiences nearly no diffraction as it propagates inside the superlattice slab, which is consistent with the findings reported in Refs. [15, 30, 31]. It is interesting to note within a macroscopic approach, when $\chi = 0$ the transfer matrix $\mathbf{M}$ [Eq. (5.6)] is unitary and of the form $\mathbf{M} = \exp\left(\pm i \dfrac{|E - V_{av}|}{\hbar v_F} x \boldsymbol{\sigma}_x \right)$. Because of this, the transfer matrix is independent of k_y and it can be checked that the calculated probability density function does not depend on the *x* coordinate in the GSLs regions. Hence the profile of the wave function at the input and output planes is exactly coincident.

To illustrate how the dual GSLs with $\chi_1 = -\chi_2 = -1/5.6$ may also enable bridging the input and output region for an incoming spatially confined wave packet, we consider a scenario wherein a Gaussian electron wave impinges on the dual GSL nanomaterials, similar to what was done in Sec. V.4. The dual GSLs have the same structural parameters as in Fig 5.11, except that the tunneling energy is set to $E_0 a/\hbar v_F = 0.025$ and the average potentials offsets are adjusted to $\left(V_{1,2,\mathrm{av}} - E_0\right) a/\hbar v_F = \mp 0.5$. For this design the conditions $T \approx 1$ and $R \approx 0$ are approximately satisfied for $|k_y| < k_{y,\max}$ with $k_{y,\max} a = 1.1$, as shown in Fig. 5.15.

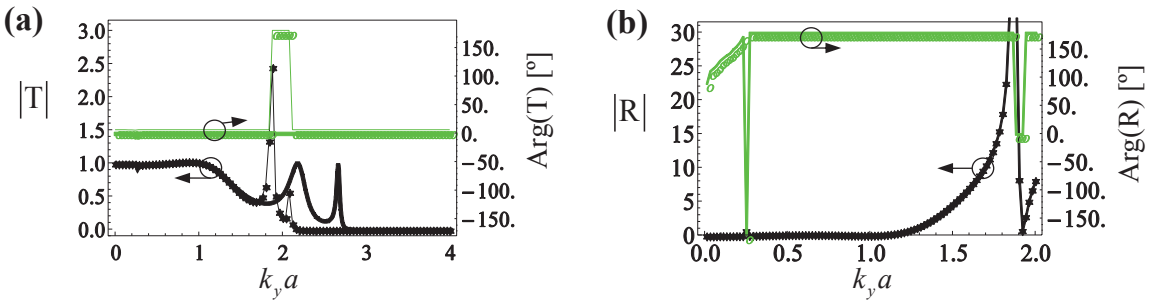

Fig. 5.15 Amplitude and phase of the **(a)** transmission and **(b)** reflection coefficients for an electron plane wave that travels in pristine graphene with energy $E_0 a/\hbar v_F = 0.025$ and impinges on a slab of two dual GSLs with total thickness $W = 40a$, with $\chi_{1,2} = \mp 1/5.6$ and an average potential offset $\left(V_{1,2,\mathrm{av}} - E_0\right) a/\hbar v_F = \mp 0.5$.

Using the results of Fig. 5.15, we can estimate that for a Gaussian beam with a characteristic size larger than $R_{G,\min} = \lambda_{\max}/2 = 2.86a$, with $\lambda_{\max} = 2\pi/k_{y,\max}$, the dual GSL should mimic a "wormhole" at $E = E_0$, for normal incidence. Figure 5.16 depicts the calculated wave function profiles at the input and output planes for the characteristic sizes **(a)** $R_{G,1} = R_{G,\min}$ and **(b)** $R_{G,2} = R_{G,\min}/2.5$.

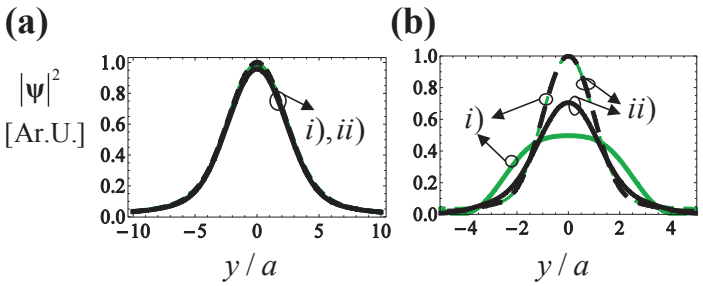

Fig. 5.16 Profile of the wave function amplitude $|\psi|^2$ normalized to arbitrary unities [Ar. U.], at the input (dashed curves) and output (solid curves) interfaces of the graphene "wormhole" for an incoming packet with **(a)** $R_{G,1} = 2.86a$ and **(b)** $R_{G,2} = 1.14a$, calculated with *i)* (green curves) the microscopic model and *ii)* (black curves) the effective medium model.

As seen, when $R_{G,1} = R_{G,\min}$ (Fig. 5.16**(a)**) the electron wave is perfectly reproduced at the output plane, whereas in Fig. 5.16**(b)** – when the localization is so fine that the response of spatial harmonics $|k_y| > k_{y,\max}$ becomes relevant – the wave function profiles at the input and output planes are quite different. Notably, in this example $R_{G,\min}$ is

extremely subwavelength as compared to the electron wavelength in pristine graphene at $E = E_0$ ($R_{G,\min} = 0.011\lambda_0$). This elucidates how well the dual GSLs can effectively short-circuit the two interfaces and imitate a wormhole for electron waves.

To further unravel the mechanisms that permit the nearly perfect transmission of the incoming electron wave, the probability density distribution $|\psi|^2$ was computed in all space using both the microscopic ($|\psi_{mic}|^2$) and macroscopic models ($|\psi_{ef}|^2$). We considered two distinct configurations represented in Figs. 5.17**(a*i*)** and 5.17**(b*i*)**. In both cases the total thickness of the two dual GSLs is the same. Thus, because dual GSLs with the same thickness "annihilate" one another, both configurations are expected to imitate a wormhole. In this example, the energy of the electrons was set to $E_0 a/\hbar v_F = 0.025$, and the average potential offsets $\left(V_{1,2,\text{av}} - E_0\right) a/\hbar v_F = \mp 0.1$, while the remaining structural parameters are the same as in Fig. 5.11. The Gaussian beam has a beamwidth $R_G = 2.86a$ at the reference plane $x_i = -5a$, and $x = 0$ is taken as the interface with the GSLs. The calculated distribution for $|\psi|^2$ is depicted in Figs. 5.17**(a)** and 5.17**(b)**.

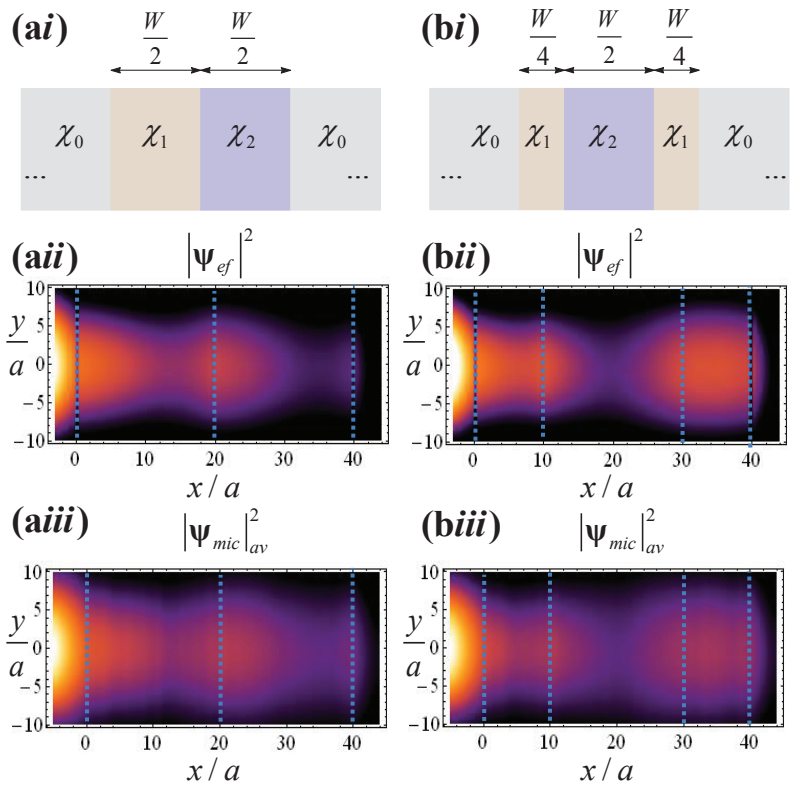

Fig. 5.17 ***(i)*** Geometries of the different dual GSLs embedded in pristine graphene ($\chi_0 = 1$). ***(ii)*** Density plots of $|\psi|^2$ (in a logarithmic scale) calculated with the effective medium theory for an incident Gaussian electron wave with $R_G = 2.86a$. ***(iii)*** Similar to ***(ii)*** but calculated with the exact microscopic theory. In all the examples, $E_0 a/\hbar v_F = 0.025$, and the GSLs are characterized by $\chi_{1,2} = \mp 1/5.6$ and $\left(V_{1,2,\mathrm{av}} - E_0\right) a/\hbar v_F = \mp 0.1$.

As seen, there is a good agreement between the effective medium model and the exact microscopic theory. Moreover, the results reveal that in this example the probability density function is peaked at the interfaces of dual graphene based nanomaterials. This should not be confused with the resonant behavior characteristic of Pendry's optical lens due to the excitation of plasmons [40], and of the HgCdTe semiconductor lens described in [35]. Indeed, it can be verified that most of the spatial spectrum inside the GSLs is associated with propagating waves. The panel ***(ii)*** of Fig. 5.18 shows the profile of the probability density function $|\psi|^2$ calculated along the line $y = 0$.

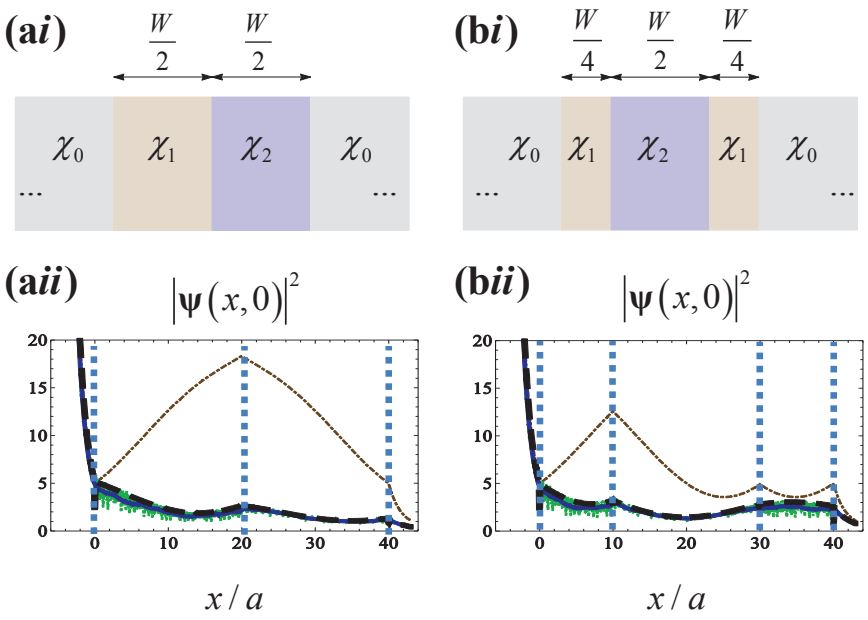

Fig. 5.18 (*i*) Geometries of the different dual GSLs embedded in pristine graphene ($\chi_0 = 1$). **(*ii*)** The pseudospinor profiles (normalized to arbitrary units, and along the $y = 0$ line) $|\psi(x,0)|^2$ as a function of the *x*-coordinate calculated using the microscopic model (green curves), the microscopic model with spatial averaging (blue curves), with the effective medium model (dashed thick black curves). The dot-dashed (brown) curves represent the results obtained with the effective medium model based on the simplistic boundary condition $\lfloor \psi \rfloor_{x=x_0} = 0$. In all the examples, $E_0 a/\hbar v_F = 0.025$, and the GSLs are characterized by $\chi_{1,2} = \mp 1/5.6$ and $\left(V_{1,2,\mathrm{av}} - E_0\right) a/\hbar v_F = \mp 0.1$.

In Fig. 5.18, the dot-dashed lines represent the effective medium results based on the naive boundary condition $\lfloor \psi \rfloor_{x=x_0} = 0$. As seen, such approach highly overestimates the peak value of $|\psi|^2$, leading to a completely erroneous distribution for $|\psi|^2$. This reinforces the idea that in the effective medium model the boundary condition is different from that of the microscopic theory.

V.6. Concluding Remarks

In this chapter, we showed that some phenomena previously studied in photonics, such as the negative refraction of light and light wormholes, can be successfully extended to electronics. We developed a framework that based on a transfer matrix formalism, allows characterizing the scattering properties of a cascade of graphene based nanomaterials. As a by-product, it was checked that the dynamics of electron waves in graphene superlattices can be described using an effective medium approach based on a nontrivial boundary condition. This formalism was used to study the negative refraction of electron waves at the interfaces of GSLs.

Finally, it was theoretically demonstrated that GSLs with opposite signed anisotropy ratios may enable the perfect transmission of electron waves with a specific energy, mimicking a wormhole that effectively bridges the input and output interfaces, and that superlattices in the extreme anisotropy limit allow for nondifractive propagation of electron waves.

References

[1] J. D. Joannopoulos, S. G. Johnson, J. N. Winn, and R. D. Meade, *Photonic Crystals: Molding the Flow of Light,* Princeton University Press, Princeton, 2008.

[2] E. Yablonovitch, "Inhibited Spontaneous Emission in Solid-State Physics and Electronics", *Phys. Rev. Lett.* **58**, 2059, 1987.

[3] S. John, "Strong localization of photons in certain disordered dielectric superlattices", *Phys. Rev. Lett.* **58**, 2486, 1987.

[4] M. G: Silveirinha, and N. Engheta, "Metamaterial-inspired model for electron waves in bulk semiconductors", *Phys. Rev. B* **86**, 245302, 2012.

[5] V. G. Veselago, "The electrodynamics of substances with simultaneously negative values of ε and μ," *Sov. Phys. Usp.* **10**, 509, 1968.

[6] L. Esaki, and R. Tsu, "Superlattice and Negative Differential Conductivity in Semiconductors", *IBM J. Res. Dev.* **14**, 61, 1970.

[7] J. Faist, F. Capasso, D. L. Sivco, C. Sirtori, A. L. Hutchinson, and A. Y. Cho, "Quantum Cascade Laser", *Science* **264**, 553, 1994.

[8] J. R. Meyer, C. A. Hoffman, F. J. Bartoli, J. W. Han, J. W. Cook, J. F. Schetzina, X. Chu, J. P. Faurie, and J. N. Schulman., "Ultrahigh electron and hole mobilities in zero-gap Hg-based superlattices" *Phys. Rev. B* **38**, 2204, 1988.

[9] M. König, S. Wiedmann, C. Brüne, A. Roth, H. Buhmann, L. W. Molenkamp, X.-L. Qi, and S.-C. Zhang, "Quantum Spin Hall Insulator State in HgTe Quantum Wells", *Science* **318**, 766, 2007.

[10] M. G: Silveirinha, and N. Engheta, "Transformation electronics: Tailoring the effective mass of electrons", *Phys. Rev. B* **86**, 161104(R), 2012

[11] L. Jelinek, J. D. Baena, J. Voves, and R. Marqués, "Metamaterial-inspired perfect tunnelling in semiconductor heterostructures", *New J. Phys*. **13**, 083011, 2011.

[12] V.V. Cheianov, V. Fal'ko, and B. L. Altshuler, "The Focusing of Electron Flow and a Veselago Lens in Graphene p-n Junctions", *Science* **315**, 1252, 2007.

[13] I. Hrebikova, L. Jelinek, J. Voves, and J. D. Baena, "A perfect lens for ballistic electrons: An electron-light wave analogy", *Photonics Nanostruct. Fundam. Appl.* **12**, 9, 2014.

[14] S. Lannebère, and M. G. Silveirinha, "Effective Hamiltonian for electron waves in artificial graphene: A first-principles derivation", *Phys. Rev. B* **85**, 195413, 2012.

[15] M. G. Silveirinha, and N. Engheta, "Effective medium approach to electron waves: Graphene superlattices", *Phys. Rev. B* **85**, 195413, 2012.

[16] K. S. Novoselov, A. K. Geim, S. V. Morozov, D. Jiang, M. I. Katsnelson, I. V. Grigorieva, S. V. Dubonos, and A. A. Firsov, "Two-dimensional gas of massless Dirac fermions in graphene", *Nature* **438**, 197, 2005.

[17] A. K. Geim, and K. S. Novoselov, "The rise of graphene", *Nature Mater.* **6**, 183, 2007.

[18] A. H. Castro Neto, F. Guinea, N. M. R. Peres, K. S. Novoselov, and A. K. Geim, "The electronic properties of graphene", *Rev. Mod. Phys.* **81**, 109, 2009.

[19] M. I. Katsnelson, "The electronic properties of graphene", *Mater. Today* **10**, 20, 2007.

[20] M. I. Katsnelson, K. S. Novoselov, and A. K. Geim, "Chiral tunnelling and the Klein paradox in graphene", *Nat. Phys.* **2**, 620, 2006.

[21] A. V. Rozhkov, G. Giavaras, Y. P. Bliokh, V. Freilikher, and F. Nori, "Electronic properties of mesoscopic graphene structures: Charge confinement and control of spin and charge transport", *Phys. Rep.* **77**, 503, 2011.

[22] A. Vakil, and N. Engheta, "Transformation Optics Using Graphene", *Science* **332**, 1291, 2011.

[23] K. S. Novoselov, A. K. Geim, S. V. Morozov, D. Jiang, Y. Zhang, S. V. Dubonos, I. V. Grigorieva, and A. A. Firsov, "Electric Field Effect in Atomically Thin Carbon Films", *Science* **306**, 666, 2004.

[24] M. P. Levendorf, C.-J. Kim, L. Brown, P. Y. Huang, R. W. Havener, D. A. Muller, and J. Park, "Graphene and boron nitride lateral heterostructures for atomically thin circuitry", *Nature* **488**, 627, 2012.

[25] C. Dean, A. Young, L. Wang, I. Meric, G.-H. Lee, K. Watanabe, T. Taniguchi, K. Shepard, P. Kim, and J. Hone, "Graphene based heterostructures", *Solid State Commun.* **152**, 1275, 2012.

[26] Y. P. Bliokh, V. Freilikher, S.Savel'ev, and F. Nori, "Transport and localization in periodic and disordered graphene superlattices", *Phys. Rev. B* **79**, 075123, 2009.

[27] P. Burset, A. L. Yeyati, L. Brey, and H. A. Fertig, "Transport in superlattices on single-layer graphenes", *Phys. Rev. B* **83**, 195434, 2011.

[28] L.-G. Wang, and S.-Y. Zhu, "Electronic band gaps and transport properties in graphene superlattices with one-dimensional periodic potentials of square barriers", *Phys. Rev. B* **81**, 205444, 2010.

[29] C. H. Park, L. Yang, Y. W. Son, M. L. Cohen, and S. G. Louie, "New Generation of Massless Dirac Fermions in Graphene under External Periodic Potentials", *Phys. Rev. Lett.* **101**, 126804, 2008.

[30] C.-H. Park, L. Yang, Y.-W. Son, M. L. Cohen, and S. G. Louie, "Anisotropic behaviours of massless Dirac fermions in graphene under periodic potentials", *Nat. Phys.* **4**, 213, 2008.

[31] C.-H. Park, Y.-W. Son, L. Yang, M. L. Cohen, and S. G. Louie, "Electron Beam Supercollimation in Graphene Superlattices", *Nano Lett.* **9**, 2920, 2008.

[32] J. C. Meyer, C.O. Girit, M. F. Crommie, and A. Zettl, "Hydrocarbon lithography on graphene membranes", *Appl. Phys. Lett.* **92**, 123110, 2008.

[33] M. Yankowitz, J. Xue, D. Cormode, J. D. Sanchez-Yamagishi, K. Watanabe, T. Taniguchi, P. Jarillo-Herrero, P. Jacquod, and B. J. LeRoy, "Emergence of

superlattice Dirac points in graphene on hexagonal boron nitride", *Nature Phys*. **8**, 382, 2012.

[34] L. A. Ponomarenko, R. V. Gorbachev, G. L. Yu, D. C. Elias, R. Jalil, A. A. Patel, A. Mishchenko, A. S. Mayorov, C. R. Woods, J. R. Wallbank, M. Mucha-Kruczynski, B. A. Piot, M. Potemski, I. V. Grigorieva, K. S. Novoselov, F. Guinea, V. I. Fal'ko, and A. K. Geim, "Cloning of Dirac fermions in graphene superlattices", *Nature* **497**, 594, 2013.

[35] M. G. Silveirinha, and N. Engheta," Spatial Delocalization and Perfect Tunneling of Matter Waves: Electron Perfect Lens", *Phys. Rev. Lett.* **110**, 213902, 2013.

[36] A. Greenleaf, Y. Kurylev, M. Lassas, and G. Uhlmann, "Electromagnetic Wormholes and Virtual Magnetic Monopoles from Metamaterials", *Phys. Rev. Lett.* **99**, 183901, 2007.

[37] J. B. Pendry, D. Schurig, and D. R. Smith, "Controlling Electromagnetic Fields", *Science* **312**, 1780, 2006.

[38] U. Leonhardt, "Optical Conformal Mapping", Science **312**, 1777, 2006.

[39] V. M. Shalaev, "Transforming Light", *Science* **322**, 384, 2008.

[40] J. B. Pendry, "Negative Refraction Makes a Perfect Lens", *Phys. Rev. Lett.* **85**, 3966, 2000.

[41] Y. Liu, G. Bartal, and X. Zhang, "All-angle negative refraction and imaging in a bulk medium made of metallic nanowires in the visible region", *Opt. Express* **16**, 15439, 2008.

[42] J. Yao, Z. Liu, Y. Liu, Y. Wang, C. Sun, G. Bartal, A. M. Stacy, and X. Zhang, "Optical Negative Refraction in Bulk Metamaterials of Nanowires", *Science*, **321**, 930, 2008.

VI. CONCLUSIONS

VI.1. Main Results

In this thesis, it we presented a variety of new and exciting theoretical and numerical results obtained from different configurations of structured materials.

In Chapter II we developed an effective medium model for a uniaxial wire-medium formed by two nested sets of parallel wires. The effective dielectric constant of the metamaterial and the photonic modes supported in the bulk nested wire media received particular attention. Using this effective medium model, we proposed a formalism to solve scattering problems involving the metamaterial, and it was shown, both theoretically and numerically, that the transmission and reflection properties of the nested wire media may be drastically modified when there is some structural asymmetry in the system. In such circumstances, the electromagnetic response of the two sub-arrays may be rather different and the currents in the two sets of wires may flow in opposite directions. It was shown that this phenomenon may allow engineering the scattering properties of the effective medium, resulting in sharp Fano-type resonances [1, 2] in the transmission and reflection coefficients of the slab.

In Chapter III we investigated the emission of Cherenkov radiation by a pencil of electric charges moving inside a nanowire metamaterial using an effective medium theory. It was revealed that the main radiation channel is associated with the q-TEM mode, and since the dispersion of this mode does not depend on the velocity of the charges, it is always possible to couple the moving charges to a propagating mode, enabling the emission of Cherenkov radiation with no velocity threshold, contrary to

what is observed in natural materials [3]. Moreover, it was shown that the nanowire array allows guiding the emitted radiation in a very specific direction. We also demonstrated that the anomalously high density of photonic states in the wire media leads to an enhancement of the stopping power by more than two orders of magnitude as compared to other natural media.

In Chapter IV, we studied the formation and propagation of 3-D bright and dark spatial solitons with cylindrical symmetry in a nanowire metamaterial embedded in a nonlinear Kerr-type host medium. The performed analysis relied on effective medium techniques, and we showed that unlike in conventional nonlinear dielectric media, dark (bright) unstaggered solitons can be formed only when the host medium is a self-focusing (defocusing) Kerr dielectric. In this Chapter, we also developed a framework that allowed characterizing the propagation of the spatial solitons. We calculated the solitons profile and studied the influence of variations in the structural parameters of the metamaterial and of the oscillation frequency on the confinement of the solitary waves. The results revealed that for both types of solitons, perturbations that increase the hyperbolicity of the isofrequency contours of the metamaterial are detrimental to the confinement of the solitons. Moreover, we showed that the main decay channel of the solitons is associated with the absorption in the dielectric host rather than to the metallic loss. We also proved that for sufficiently large optical field intensities, the spatial solitons can, in theory, have a subwavelength modal size.

Finally, in Chapter V we theoretically showed that some phenomena previously studied in the context of electromagnetic metamaterials, such as the negative refraction of light [4, 5] and light wormholes [6-9], can have electronic counterparts in graphene based nanomaterials. Based on the effective medium model described in [10], we developed a framework that allows characterizing the scattering properties of a cascade

of graphene based nanomaterials and also determining the spatial distribution of the wavefunction. This approach is based on a transfer matrix formalism, and revealed that under the macroscopic approach the dynamics of electron waves in a graphene superlattices needs to be based on a nontrivial boundary condition at the interfaces between distinct materials. We showed that the proper tuning of the average potentials in adjacent graphene based nanomaterials permits the negative refraction of electron waves. Among the set of novel results described in this Chapter, it is important to mention that we demonstrated that superlattices with symmetric anisotropy ratios may enable the perfect transmission of electron waves with a specific energy, mimicking a wormhole that effectively bridges the input and output interfaces, as if the superlattice cascade was nonexistent. Furthermore, we also showed that the proper tuning of the microscopic potential in superlattices allows tailoring the group velocity of the electrons, and that superlattices characterized by an extreme anisotropy allow for nondifractive propagation of electron waves.

VI.2. Future Work

To conclude the thesis, next we discuss some possible extensions of the presented studies as well as other research directions.

One topic that is worth further development is the Cherenkov emission in nanowire media. It would be interesting to numerically validate the results obtained with the effective medium model. This may be done with the help of an electromagnetic simulator, for instance CST Particle Studio [11].

Similarly, it is also desirable to determine the spatial solitons in nanowires arrays using a full wave theory. Again this may done with the help of an electromagnetic simulator, such as CST Microwave Studio [12].

Still regarding the nonlinear effects in wire media, it may be interesting to study configurations wherein the nanowires are loaded with nonlinear elements, e.g. a variable capacitance diode, commonly known as varactor. Since the response of the diode is dependent on the voltage drop across its terminals, it is expected that the scattering properties of the metamaterial may become tunable with the amplitude of the excitation signal, alternating between states of total transmission and complete reflection, similar to a switch.

Although it was not discussed in this thesis, in Ref. [J7] we developed a Finite Difference in the Time Domain numerical algorithm to characterize the time dynamics of electrons in complex graphene superlattices, for both the effective medium [10] and microscopic models. Future work regarding this subject will focus on extending the algorithm to characterize the optical properties of graphene based nanomaterials, namely calculating the electrical conductivity of superlattices and the consistency of the effective medium model results in such problems.

References

[1] U. Fano, “Effects of configuration interaction on intensities and phase shifts”, *Phys. Rev.* **124**, 1866, 1961.

[2] A. E. Miroshnickenko, S. Flach, and Y. S. Kivshar, “Fano resonances in nanoscale structures”, *Rev. Mod. Phys.* **82**, 2257, 2010.

[3] P. A. Čerenkov, “Visible radiation produced by electrons moving in a medium with velocities exceeding that of light”, *Phys. Rev.* **52**, 378, 1934

[4] Y. Liu, G. Bartal, and X. Zhang, “All-angle negative refraction and imaging in a bulk medium made of metallic nanowires in the visible region”, *Opt. Express* **16**, 15439, 2008.

[5] J. Yao, Z. Liu, Y. Liu, Y. Wang, C. Sun, G. Bartal, A. M. Stacy, and X. Zhang, “Optical Negative Refraction in Bulk Metamaterials of Nanowires”, *Science*, **321**, 930, 2008.

[6] A. Greenleaf, Y. Kurylev, M. Lassas, and G. Uhlmann, "Electromagnetic Wormholes and Virtual Magnetic Monopoles from Metamaterials", *Phys. Rev. Lett.* **99**, 183901, 2007.

[7] J. B. Pendry, D. Schurig, and D. R. Smith, "Controlling Electromagnetic Fields", *Science* **312**, 1780, 2006.

[8] U. Leonhardt, "Optical Conformal Mapping", Science **312**, 1777, 2006.

[9] V. M. Shalaev, "Transforming Light", *Science* **322**, 384, 2008.

[10] M. G. Silveirinha, and N. Engheta, "Effective medium approach to electron waves: Graphene superlattices", *Phys. Rev. B* **85**, 195413, 2012.

[11] CST GmbH 2014 CST Particle Studio http://www.cst.com.

[12] CST GmbH 2014 CST Microwave Studio http://www.cst.com.